Towards single atom aided probing of an ultracold quantum gas

Dissertation

zur

Erlangung des Doktorgrades (Dr. rer. nat.)

der

Mathematisch-Naturwissenschaftlichen Fakultät

der

Rheinischen Friedrich-Wilhelms-Universität Bonn

vorgelegt von

Shincy John

aus

Kottayam (Indien)

Bonn 2010

Angefertigt mit Genehmigung der Mathematisch-Naturwissenschaftlichen Fakultät
der Rheinischen Friedrich-Wilhelms-Universität Bonn

1. Gutachter: Prof. Dr. Dieter Meschede
2. Gutachter: Prof. Dr. Martin Weitz

Tag der Promotion: 22.02.2011

Erscheinungsjahr: 2011

Abstract

In this thesis, the interactions in an unbalanced Rubidium (Rb)-Caesium (Cs) mixture are studied, where the Cs atoms have been used as probes to study the interspecies interactions. The Rb atoms are trapped and stored in a conservative potential, in an optical dipole trap and cooled to quantum degeneracy. The coherent manipulation of the spin states is realized using a microwave and radio frequency radiation to prepare the Rb atoms in the various Zeeman split hyperfine levels of the ground state. Cs atoms are trapped in a MOT. An overlap of these two entities is obtained via a magnetic transport to study the interspecies interactions. The dynamics of the Cs MOT is studied in the presence of a 600 nK thermal cloud of Rb, where a loss in the Cs atoms is observed. Rb remains unaffected. Here, a method has been demonstrated, where the interspecies inelastic two- and three-body collisions have been investigated by monitoring the one- and two-atom loss rates in Cs. Each term in the complicated inelastic rate equation has been determined individually without having to solve the rate equation which can not be solved analytically. This is therefore, a nondestructive and simple method to extract information about the interactions and can be performed for future experiments with Cs in a conservative species specific potential.

Contents

Introduction

Ultracold quantum gases and single neutral atoms represent the two different regimes of many-body and few-body quantum physics. The pooling of these two entities helps in the study of many interesting quantum phenomena, e.g. the decoherence studies of a quantum degenerate gas. Also, the special properties of each of them such as coherence in an ultracold quantum gas and spatial and particle resolution in single neutral atoms, can be used to manipulate one by the other and to address the challenges posed by each of them. This therefore, provides us with an amazing integrated system.

The advent of the techniques of laser cooling [1, 2, 3] and evaporative cooling [4, 5], along with the novel trapping techniques provided by traps like the Magneto-Optical Trap (MOT) [6, 7] and magnetic traps [8, 9, 10] have led to the cooling of dilute atomic gases to temperatures of a few hundred nanokelvin. This resulted in the realization of a Bose-Einstein Condensate (BEC) [11, 12, 13, 14], a coherent state of matter, representing a many-body quantum object. This breakthrough was followed by an explosion of experiments in the field of ultracold quantum gases. The use of optical dipole traps [15, 16] provided extended flexibility to the trapping of atoms and the manipulation of atomic interactions via. magnetic fields through Feshbach resonances [17, 18]. This turned out to be an important tool in the tuning of intra-and inter-species interactions resulting in the formation of molecules [19, 20], molecular BECs [21, 22] and double condensates [23]. This has also enabled the condensation of fermionic pairs in the Bardeen-Cooper-Schrieffer (BCS)-BEC crossover regime [24, 25, 26]. These weakly interacting systems exhibit long range coherence. However, particle and spatial resolution is challenging in these systems.

Ultracold quantum gases in optical lattices [27, 28, 29] at low temperatures undergo a transition from the superfluid to the Mott insulator state [30, 31] which represents a strongly correlated system. In such systems, coherent transport of neutral atoms over a definite number of lattice sites has been realized [32]. Such systems provide a platform for the realization of multi-particle entangled states through controlled collisions between atoms in the neighbouring lattice sites [33, 34]. However, single atom and single site detection is demanding in these systems. Recently, single atom and single site detection has been realized in such a system via in situ fluorescence imaging [35, 36].

In the few-body regime, we have single neutral atoms. They are suitable candidates for storing and transmitting quantum information. A deterministic source of single neutral atoms has been demonstrated in [37, 38]. A neutral atom quantum register with a string of neutral atoms with high spatial resolution has been realized in [39]. Such strings of atoms can also be sorted and arranged precisely [40, 41]. The spin state of an atom has been detected via a quantum non-demolition method through quantum jumps [42, 43]. Recently, the diffraction limit has been overcome in detecting neutral atoms in neighbouring lattice sites via fluorescence imaging [44]. Hence, single atom and single site detection has been widely demonstrated experimentally in neutral atoms. However, the realization of coherent interactions which is also one of the pre-requisites for quantum information processing is rigorous.

Combining these two systems (many-body and few-body) could provide a platform to address the challenges posed by each of them. Several proposals have been made for experiments concerning a single atom and a many-body system finding applications in quantum information processing. Single atom cooling by immersing it in a condensate to compensate for the heating and decoherence caused during the transport of a qubit has been proposed in [45, 46]. A quantum non-demolition method to detect the state of a qubit using a condensate as a single atom mirror has been studied in [47], whereas the interactions between two impurity atoms immersed in a condensate for the realization of a two qubit gate has been discussed in [48]. Proposals have also been made for the study of the properties of a condensate using an impurity atom. Here, the phase fluctuations [49] and decoherence [50] in a BEC have been theoretically studied non-destructively using a single atom coupled to the BEC.

In our experiment, we intend to experimentally realize a Caesium (Cs) single atom immersed in a Rubidium (Rb) BEC. These two species provide a conducive environment for the realization of such experiments due to the strong interactions between them. A lower limit of the interspecies triplet s-wave scattering length has been deduced to be $150\,a_0$ for Cs in the $f = 4, m_\mathrm{f} = 4$ and Rb in the $f = 2, m_\mathrm{f} = 2$ states, where a_0 is the Bohr radius and f and m_f are the quantum numbers representing the hyperfine and Zeeman split hyperfine states respectively [51, 52]. Besides, 23 interspecies magnetic Feshbach resonances have been found [53] which allows the tuning of the interactions between these species, an important tool for the manipulation of both the species for various applications. The first steps towards the creation of an integrated many-body and few-body system was performed with Rb and Cs atoms stored in a conventional and a single atom MOT, respectively. Here, Cs atoms were used as probes to study the interspecies interactions without disturbing the many body system (Rb) [54, 55].

In this thesis, a further step has been taken by trapping and storing Rb atoms in a conservative potential, in an optical dipole trap. The Rb atoms are cooled to quantum degeneracy. Cs atoms are trapped in a MOT. The techniques involved in overlapping the two entities and the coherent manipulation of the atomic states of Rb through a microwave and Radio Frequency (RF) radiation are developed here. The interaction between the Rb cloud and the single Cs atoms are studied by analysing the losses in the Cs atoms. Here, a non-destructive and simple method has been developed to quantify the interspecies interactions by studying the interspecies inelastic collisional loss rates. Although, the interactions are still light-induced, the techniques developed in this thesis, would be used along with a species specific conservative trap for Cs, to immerse or insert a Cs atom in its absolute ground state, in a Rb BEC, in a controlled fashion for all future experiments.

The thesis has been structured as follows. Chapter 1 deals with the theoretical description of the scattering processes and the BEC theory. In chapter 2, the theoretical framework of the coherent control of the spin degrees of freedom is discussed. Chapter 3 deals with the experimental setup and the route towards the preparation of an ultracold gas of Rb in a magnetic trap and a single atom Cs MOT. In chapter 4, the Rb condensate is prepared in an optical dipole trap and the Rb atoms are prepared in their various spin states using a microwave and RF radiation. Chapter 5 deals with the interactions between an ultracold Rb gas and a single or a few Cs atoms. Finally, chapter 6 ends with concluding remarks and a brief outlook over future experiments.

1 Ultracold Gases and their Interactions

Recent developments in laser cooling and evaporative cooling techniques have led to the production of cold and ultracold gases. The temperatures of such gases lie between a few hundred microkelvin to a few tens of nanokelvin with densities varying between $10^{10} - 10^{15}\,\mathrm{cm}^{-3}$, respectively. At these temperatures and densities, quantum effects start to become evident and the gases can no longer be described classically. The gases used for most experiments are alkali gases due to the ease in laser cooling because of the presence of a closed transition. Furthermore, these gases are considered dilute as the inter-particle distance ($\sim$100 nm) is much larger than their scattering length, which describes the interaction between the particles at such low temperatures (see section 1.1). Since the gases are dilute, for the description of the interactions it is sufficient to consider interactions which involve only two atoms. These interactions can therefore, be described by the two-body interaction potential which describes all the macroscopic properties of the system. However, at relatively large densities ($10^{14} - 10^{15}\,\mathrm{cm}^{-3}$), e.g. in the case of a Bose-Einstein Condensate (BEC), three-body interactions also play an important role.

In this chapter, the theoretical framework concerning the interactions of cold and ultracold gases is discussed by means of the scattering theory in sections 1.1 and 1.2. Section 1.3 deals with a BEC.

1.1 Scattering Theory

The interaction between two atoms can be described by the quantum mechanical scattering theory, where the collisions between the atoms are taken into account. The interactions are described by the trajectories of the relevant atoms involved in the collisions before and after the collisions. These collisions are distinguished depending upon the conservation of energy and the preservation of the internal states of the atoms during the collisions. Hence, we have elastic and inelastic scattering. This will be briefly discussed in the following sections.

1.1.1 Elastic Scattering

Elastic scattering occurs when the internal states of the atoms do not change during the scattering process and when the kinetic energy is conserved. The elastic scattering rate is an important quantity, since it sets a limit on the speed and efficiency of evaporative cooling (see section 3.5.1). It is responsible for the thermalization of an atomic sample through exchange of momentum. Therefore, it is also an important phenomenon required for the study of interesting effects in a doped many-body system. To describe the theory of elastic scattering the following approximations are made.

a) Particles have no internal structure, i.e. in this case, no spin. The case which includes spin will be discussed in section 1.2.

b) Particles are distinguishable, the generalization to the case of identical particles will be shown later.

c) Interactions between two particles are described by the interaction of their reduced mass with a potential which has the form of a central potential with a finite range r_0, i.e. it vanishes at ∞.

The description is based on the theory given in [56]. Consider two atoms colliding with each other, interacting through a potential given by $V(r)$ which satisfies the condition given in **c)**. The scattering properties can be determined by solving the time independent Schrödinger equation (TISE) given by

$$\left(\frac{p^2}{2\mu_\mathrm{r}} + V(r)\right)\psi_k(r) = E_k\psi_k(r) \ , \tag{1.1}$$

where μ_r is the reduced mass of the particles, E_k is the energy which is given by $E_k = \hbar^2k^2/2\mu_\mathrm{r}$ and p is the momentum. The asymptotic form of the solution of equation (1.1) is given at large distances (distances much larger than the range of the potential, $r \gg r_0$) by the superposition of the incident wave and the scattered wave. The incident wave is considered as a plane wave propagating along the z direction and the solution is therefore written in the spherical coordinates as

$$\psi_k(r) \sim e^{ikz} + f(k,\theta,\phi)\frac{e^{ikr}}{r} \ , \tag{1.2}$$

where $f(k,\theta,\phi)$ is the scattering amplitude which depends on the energy through the momentum vector k and the scattering direction through θ and ϕ. If the potential is considered as spherically symmetric, then the dependence on ϕ can be eliminated. A schematic of the scattering process is shown in figure 1.1. From the scattering amplitude, the differential scattering cross-section can be determined by the following equation,

$$\frac{d\sigma}{d\Omega_\mathrm{s}} = |f(k,\theta)|^2 \ , \tag{1.3}$$

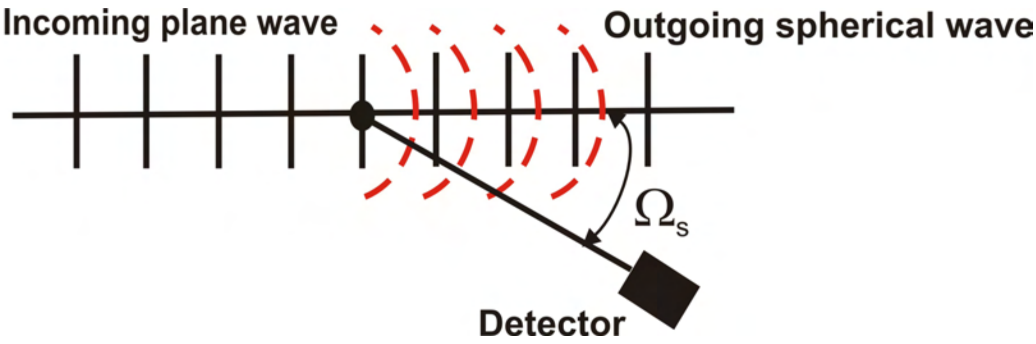

Figure 1.1: The quantum mechanical scattering is demonstrated. The black lines correspond to incoming plane waves which are scattered at a potential resulting in outgoing spherical waves (red dashed). The detector is placed at an angle Ω_s which represents the solid angle.

where Ω_s represents the solid angle through which the particle is scattered and σ is the scattering cross-section. The total cross-section is then obtained by integrating over the entire solid angle. The scattering amplitude can now be determined by solving the TISE in equation (1.1). For the spherically symmetric potential, the method of partial waves can be used, where a partial wave is a spherical wave represented by the angular momentum quantum number l. At low temperatures, this is also quite useful as the contribution to scattering comes from only the lower partial waves. This will be explained later. The solution can be written as a combination of a radial and a spherical wave function and is given by

$$\psi_k(r) = \sum_{l=0}^{\infty} Y_l^0(\theta) \frac{u_{k,l,0}(r)}{r} \,, \tag{1.4}$$

where $Y_l^0(\theta)$ are the spherical harmonic functions and $u_{k,l,0}$ represents the radial wave function. The 0 in both the wave functions corresponds to the value m which represents the azimuthal quantum number and is 0 as the potential is independent of the azimuthal angle ϕ. The scattering state for $r \gg r_0$ can therefore be written as

$$\psi_k(r) \sim \frac{1}{2\imath kr} \sum_{l=0}^{\infty} (2l+1) P_l(\cos\theta) \left((-1)^{l+1} e^{-\imath kr} + e^{2\imath\delta_l} e^{\imath kr}\right) \,, \tag{1.5}$$

where $P_l(\cos\theta)$ are the Legendre polynomials. The incident plane wave is written as a superposition of incoming and outgoing spherical waves with a relative phase depending upon l. Hence, the scattering state is equivalent to the incident wave with a phase shift given by δ_l due to the potential. Using equation (1.4) in the TISE of equation (1.1), a one dimensional (1D) Schrödinger equation can be written for every radial wave function $u_{k,l}(r)$. Here, it is assumed that $u_{k,l}(r)/r$ is regular at $r = 0$ i.e.

at the origin. The Schrödinger equation is then written as

$$u''_{k,l}(r) + \left(\frac{\hbar^2 k^2}{2\mu_{\mathrm{r}}} - \frac{\hbar^2 l(l+1)}{2\mu_{\mathrm{r}} r^2} - V(r) \right) u_{k,l}(r) = 0 \ , \tag{1.6}$$

where the effective potential is given by

$$V_{\mathrm{eff}} = \frac{\hbar^2 l(l+1)}{2\mu_{\mathrm{r}} r^2} + V(r) \ . \tag{1.7}$$

Here, the first term is the centrifugal barrier term and puts a limit on the number of partial waves contributing to collisions depending upon the energy of the colliding atoms. The asymptotic form of the radial wave function can be written similar to equation (1.5) and this gives the values of the scattering amplitude and the total scattering cross-section in terms of the phase shifts,

$$f(k,\theta) = \frac{1}{2\imath k} \sum_{l=0}^{\infty} (2l+1) \left(e^{2\imath\delta_l} - 1 \right) P_l(\cos\theta) \ , \tag{1.8}$$

$$\sigma(k) = \frac{4\pi}{k^2} \sum_{l=0}^{\infty} (2l+1) \sin^2 \delta_l(k) \ . \tag{1.9}$$

Low Energy Limit

In the low energy limit, the scattering is considered to be isotropic for a potential with a finite range. This can be explained by considering the fact that only the lowest partial wave viz. that corresponding to $l = 0$ contributes to scattering at low energies. This limit is introduced due to the centrifugal barrier term shown in equation (1.7). This is equivalent to a repulsive potential and only atoms having energy higher than this potential are able to cross this potential in order to experience the scattering potential $V(r)$. For alkali atoms, in the low energy limit, i.e. in the temperature range of a few tens to a hundred microkelvin, only the s wave scattering ($l = 0$) is relevant. This is because at these temperatures the atoms do not have sufficient energy to cross the energy barrier for $l \neq 0$. For the s-wave scattering, the effective potential is just the interatomic potential. This can also be written in terms of the phase shifts as

$$\delta_l(k) \propto k^{2l+1} \qquad \text{when } k \to 0 \ , \tag{1.10}$$

such that the cross-section becomes

$$\sigma_{l\neq 0}(k) \propto k^{4l} \ , \tag{1.11}$$

which goes to 0 as $k \to 0$. In the limit $k \to 0$, the scattering cross-section for the s-wave can be written as

$$\lim_{k\to 0} \sigma_{l=0}(k) = 4\pi a^2 \ , \tag{1.12}$$

where a represents the scattering length which is defined as

$$a = -\lim_{k\to 0} \frac{\tan\delta_0(k)}{k} \ . \tag{1.13}$$

Hence, we see that the scattering is isotropic for the s-wave as the cross-section is constant and does not depend on θ.

Identical Particles

The scattering cross-section was determined by making the assumption that the particles are distinguishable. This is however, not the case at extremely low temperatures where the particles become indistinguishable. For identical particles, the symmetrization of the wave function needs to be taken into account. This differential cross-section is therefore written as

$$\frac{d\sigma}{d\Omega_\mathrm{s}} = |f(k,\theta) + \epsilon f(k, \pi - \theta)|^2 \ , \tag{1.14}$$

where $\epsilon = +1(-1)$ corresponding to bosons (fermions)[1]. The contribution to the scattering cross-section is only from even (odd) partial waves for bosons (fermions) with a respective doubling of their contributions given by

$$\sigma(k) = \frac{8\pi}{k^2} \sum_{l,\mathrm{even}} (2l+1)\sin^2\delta_l(k) \qquad \text{for bosons} \ \ , \tag{1.15}$$

$$\sigma(k) = \frac{8\pi}{k^2} \sum_{l,\mathrm{odd}} (2l+1)\sin^2\delta_l(k) \qquad \text{for fermions} \ \ . \tag{1.16}$$

1.1.2 Scattering Length

The scattering length has already been introduced in the previous section. The importance of this quantity is that its sign and magnitude describes quite well, the interactions between the particles in the low energy limit irrespective of the complicated nature of the interaction potentials. A positive scattering length indicates a repulsive interaction whereas a negative scattering length indicates an attractive interaction and the magnitude gives the strength of the interaction. Physically, it is the phase shift introduced between the initial and the asymptotic final wave functions in the presence and absence of a potential in the low energy limit,

$$-\lim_{ka\to 0} \frac{\delta_0}{ka} = a \ . \tag{1.17}$$

---

[1] Bosons are particles with integer spin whereas fermions are particles with half integer spin.

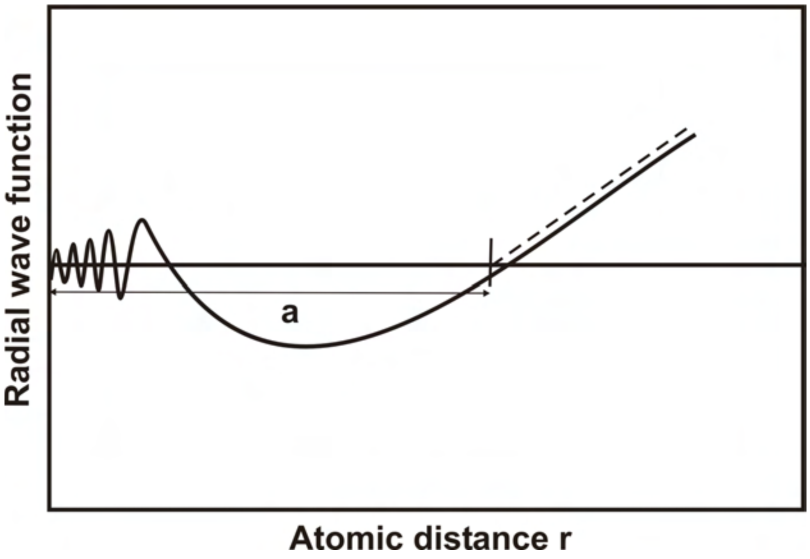

Figure 1.2: A schematic of the physical interpretation of the scattering length is illustrated. The radial wave function in the presence of a scattering potential is shown. The tangent at the asymptotic part of the wave function at large r, gives the scattering length at its zero crossing on the r axis. This is the phase shift introduced in the wave function in the presence of the potential. A positive scattering length indicates the presence of a repulsive potential.

The magnitude and sign of the scattering length is also an indication of the presence of bound states in a potential. The scattering length is negative and diverges before the formation of a bound state. After the formation of the bound state, it becomes positive and large. Figure 1.2 shows a schematic of the scattering length indicating a repulsive interaction for a bound state.

For alkali-metal atoms, the s-wave scattering lengths are of the order of $100\,a_0$ where a_0 is the Bohr radius. The large values are due to the strong Van der Waals interaction (see section 1.2) and due to the large masses of their nuclei (87 and 133 atomic mass units (a.m.u) for Rb and Cs respectively).

1.2 Inelastic Scattering

Inelastic scattering occurs when a change in the internal structure of the colliding particles takes place and when the kinetic energy is not conserved during a collision. In the previous section, the internal structure was neglected in the discussion of the elastic scattering as elastic scattering does not change the internal states during the collision. However, the internal states of the colliding atoms are important and are to be taken into account in the case of inelastic scattering. Inelastic scattering can in principle be studied in the same manner as elastic scattering with an alteration in the boundary conditions due to the change in the internal structure of the outgoing scattered wave after the collision.

The internal structure of the atoms is described in terms of the electronic and nuclear spins and their interactions in the presence of an external field. The scattering therefore, becomes a multichannel problem where a channel is described in terms of the various electronic and nuclear quantum numbers. The entrance and exit channels have different sets of quantum numbers if the internal structure changes during the collision.

The energy released during an inelastic scattering process can lead to loss of atoms from the confining trap e.g. MOT, magnetic trap or an optical dipole trap (see section 3.7) or a heating of the atoms depending upon the ratio between the released energy and the trap depth. Inelastic scattering is usually expressed in terms of the rate equation. The rate equation demonstrates the rate of change of the number of atoms in terms of the various rate constants and the density of the sample. In the case of dilute gases, inelastic scattering is divided into three types of scattering events depending upon the number of atoms lost per colliding event. They are one-body losses (loss of one atom), two-body losses (loss of two atoms) or three-body losses (loss of three atoms). The corresponding rate equation is written as follows

$$\frac{dN}{dt} = R_{\mathrm{L}} - K_1 \int n(r,t)\, d^3r - K_2 \int n^2(r,t)\, d^3r - K_3 \int n^3(r,t)\, d^3r \ , \tag{1.18}$$

where R_{L} is the loading rate, N is the number of atoms, n is the density of the sample and K_1, K_2, K_3 are the one body, two body and three body loss rate coefficients. The rate equation therefore describes the inelastic collisions quantitatively. The one-body loss occurs due to collisions with the background gas. This rate therefore depends on the quality of the vacuum used for the experiments. This greatly limits the lifetime of the atoms, especially that of a condensate, if the vacuum is not good enough. The two- and three-body loss mechanisms are discussed in detail in the following sections.

The inelastic collisions can be distinguished further depending upon the energies of the colliding atoms into cold and ultracold collisions. The nature of inelastic collisions in these two temperature regimes is very different due to the involvement of different molecular potentials where the atoms interact with each other. Here, the cold and ultracold collisions are first described for the two-body collisions. The three-body collisions are described in section 1.2.2 in the context of ultracold collisions since this is the main loss mechanism in a condensate.

1.2.1 Cold Collisions

The cold collision regime lies in the temperature range from 1 mK to 1 μK. Temperatures in a MOT lie in this range and therefore, the collisions involved in this kind of a trap are termed cold collisions. These traps use near resonant light for trapping and cooling and therefore, the dominant collisions are light-induced. Such collisions involve the presence of excited state as well as ground state molecular potentials. Figure 1.3 shows a schematic of a cold collision process [57]. The excited as well as the ground states are described by their orbital angular momentum corresponding to the quantum number l. From here on, the molecular quantum numbers corresponding to the molecular potentials involving both the atoms will be described by capital letters and the quantum numbers describing the individual atoms by small case letters.

The long range ground state potential shown as $s + s$ in figure 1.3 is dominated by the attractive Van der Waals potential. This is caused by the electrostatic dispersion forces between the atoms and has the form C_6/r^6, where r represents the distance and is the internuclear separation here. C_6 determines the strength of the Van der Waals interaction. It has values 4600 and 7380 in terms of atomic units for Rb and Cs respectively (the alkali atoms used in this thesis work) [58]. Hence, the atoms in the ground state approach each other along a potential which varies as r^{-6}. On the other hand, the $s+p$ molecular potential corresponds to one atom in the excited state and the other in the ground state. When one atom is in the excited state, the electric dipole interaction gives a first order contribution to the energy. These atoms therefore, approach each other on a potential which varies as r^{-3} which could be attractive or repulsive. We consider here, the case of the attractive potential. Since, this is much stronger than the Van der Waals potential, the excited state can have many bound states. The atoms in the ground state can absorb a red detuned photon at a distance R_o, which is in the long range part of the potential as shown in figure 1.3 and get excited to one of the bound states of the upper level forming a quasimolecule. The collisional interaction time of the quasimolecule is of the order of the decay time of the excited state or even larger than that at these temperatures. The absorption depends upon the collisional energy and the detuning of the laser light. The semiclassical approach can be used to describe these processes as it works for many different energies and detunings. The colliding atoms in the $s+p$ state can lead to atom losses from the trap via two exoergic processes viz. radiative escape or fine structure changing collisions both of which are two-body loss collisions. Both these processes depend upon the detuning and intensity of the absorbed light and the trap depth.

Radiative Escape

The atom in the ground state gets excited to the upper state by absorbing red detuned light. The colliding atoms approaching along the $1/r^3$ potential can emit a photon at a much shorter internuclear distance compared to R_o as shown in figure 1.3. The emitted photon therefore, has a lower energy than the absorbed photon and the remaining energy is distributed among the two atoms. This energy which is

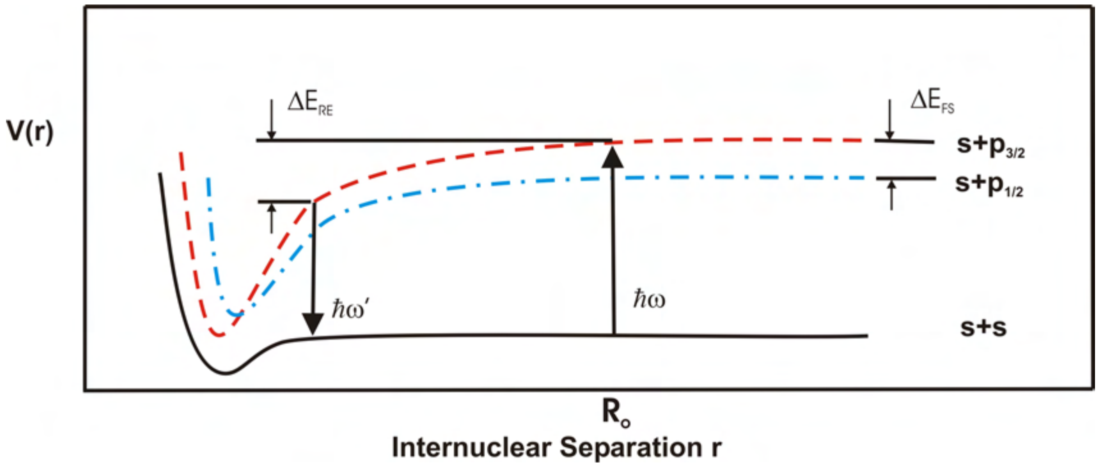

Figure 1.3: A schematic of the light induced cold collision process is shown. The ground state potential is labelled $s + s$ and shown in a black straight curve and the two excited state potentials varying from each other due to their different fine structures are shown in a red dashed $(s+p_{3/2})$ and a blue dash-dot curve $(s+p_{1/2})$. The atoms are excited to the $s + p_{3/2}$ state by absorbing a photon with frequency ω_{t} at a distance R_o. The colliding atoms move along the potential and at smaller internuclear separations compared to R_o, either decay to the ground state emitting a photon of frequency ω_{t}' and releasing an energy equal to ΔE_{RE} (radiative escape) or are transferred to the $s+p_{1/2}$ potential releasing an energy equal to ΔE_{FS} (Fine structure changing collisions)

of the order of a few Kelvin is usually sufficient for the loss of both the atoms from the trap, for a typical trap depth of a mK. The theoretical frameworks have been discussed by Gallagher and Pritchard in [59] and by Julienne and Vigue in [60]. The radiative escape process can be written as

$$A_1 + A_1 + \hbar\omega_{\mathrm{t}} \rightarrow A_2^* \rightarrow A_1 + A_1 + \hbar\omega_{\mathrm{t}}' \; , \qquad (1.19)$$

where A_1 represents the two interacting atoms, A_2^* represents the quasimolecule, ω_{t} is the frequency of the absorbed light and ω_{t}' is the frequency of the emitted light. The energy transferred to each atom during the process in the homonuclear case is given by

$$E_{\mathrm{RE}} = \frac{\hbar\left(\omega_{\mathrm{t}} - \omega_{\mathrm{t}}'\right)}{2} \; . \qquad (1.20)$$

Fine Structure Changing Collisions

The other type of inelastic collision present is due to the fine structure of the atoms. The fine structure of the atoms arises due to the coupling of the spin and angular momentum of the atoms. The excited state is therefore, split into two, viz. the

$p_{1/2}$ and the $p_{3/2}$ states, where the subscripts 1/2 and 3/2 represent the quantum number $\vec{j} = \vec{l} + \vec{s}$. Here, $\vec{l}$ is the angular momentum quantum number and $\vec{s}$ is the spin quantum number. Suppose, the atom is excited to $p_{3/2}$ by the absorption of a photon. The atoms in the ground and the excited states then collide with each other in the $s + p$ molecular potential. At a shorter internuclear distance compared to R_o, where the fine structure change plays a role, the atom can change its state from the $p_{3/2}$ to $p_{1/2}$ state releasing an energy equal to the fine structure splitting which is divided between both the atoms. This also leads to the escape of both the atoms from the trap. The fine structure changing collision can be written as

$$A_1 + A_1 + \hbar\omega_{\mathrm{t}} \to A_1^*(p_{3/2}) + A_1 \to A_1^*(p_{1/2}) + A_1 + \Delta E_{\mathrm{FS}} \ , \tag{1.21}$$

where ΔE_{FS} is the fine structure splitting energy and the energy transferred to each atom is given by $\Delta E_{\mathrm{FS}}/2$.

A third type of exoergic process which occurs in this temperature regime and in traps like the MOT are the ground state hyperfine changing collisions. The hyperfine interaction is explained in section 1.2.2. Here, the atoms interact via the Van der Waals interaction along the $s + s$ molecular potential where light plays no role. The energy released is equal to the hyperfine splitting ΔE_{HFS} and the energy transferred to each atom is $\Delta E_{\mathrm{HFS}}/2$. The ground state collisions are discussed in more detail below.

1.2.2 Ultracold Collisions

Ultracold collisions occur in the temperature range below 1 μK. Here, the energies of the colliding atoms lie below the recoil limit since light is not involved and hence the collisions are also termed dark collisions. These are also called ground state collisions, since there is no light to excite atoms to the upper excited states. The ground state molecular potentials are given by the singlet and the triplet potentials depending upon the total coupled spin of the colliding atoms which are alkali-metal atoms. For two atoms with spins in opposite directions, the total spin is $S = 0$ and represents the singlet state, whereas for two atoms with parallel spins the total spin is $S = 1$ and represents the triplet state. The interactions between the atoms are given by various different forces depending upon the internuclear distance. Figure 1.4 shows the singlet and triplet potentials for a Rb molecule.

The total Hamiltonian is given by the unperturbed Hamiltonian of the individual atoms and the interaction Hamiltonian. The internal structure of the atoms in the ground state is given by the hyperfine states and their splitting into the different Zeeman states in the presence of a magnetic field. The hyperfine interaction arises due to the coupling between the electronic spin and the nuclear spin of the atom and is given by $\vec{f} = \vec{j} + \vec{i}$, where $\vec{i}$ represents the nuclear spin and $\vec{j} = \vec{l} + \vec{s}$. The ground states of the Rb as well as the Cs atom consists of two hyperfine levels. Each of these

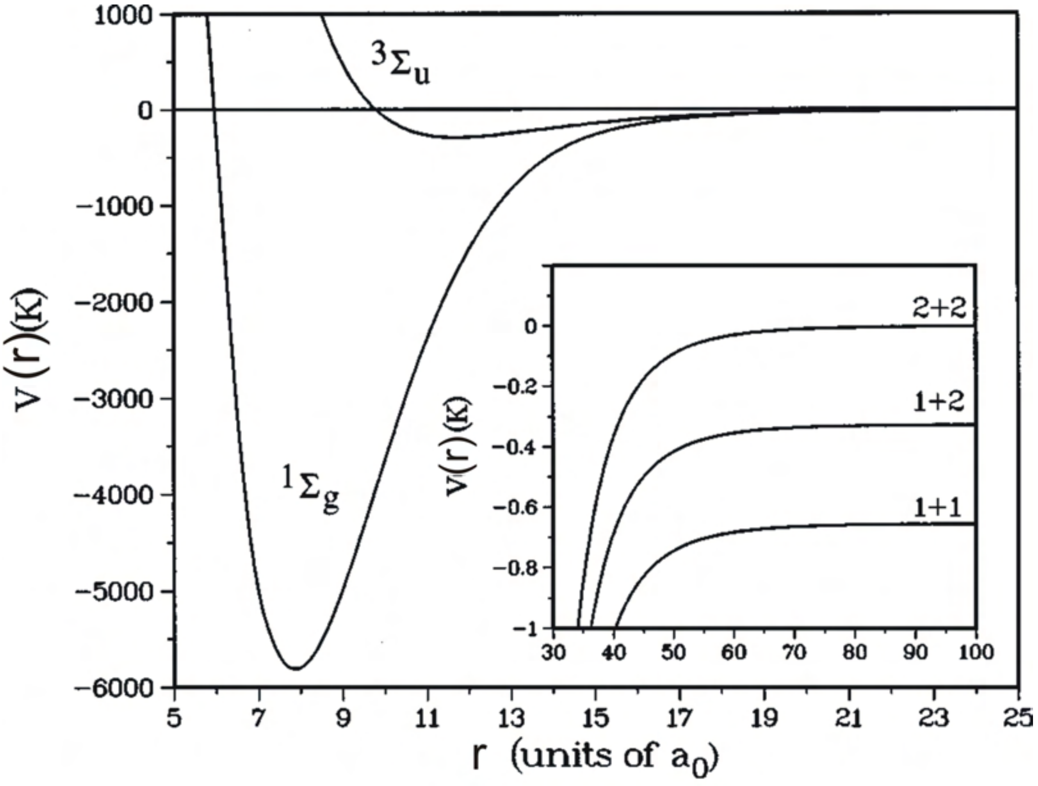

Figure 1.4: The singlet and the triplet molecular potentials of Rb_2 are plotted against the internuclear separation. The singlet potential labelled as $^1\Sigma_g$ is much steeper than the triplet potential $^3\Sigma_u$. The large positive values at short distances are due to the repulsive Coulomb interaction. At large distances equivalent to the Van der Waals length, the potentials are negative and therefore, attractive. Beyond this, the interaction between the atoms become negligible and the potential is given by the unperturbed Hamiltonian (see text). The inset shows the hyperfine splitting of the asymptotic part of the triplet potential. Figure taken from [57].

hyperfine levels is degenerate and the degeneracy is lifted when they are placed in a magnetic field splitting them into $2f+1$ states due to the Zeeman effect. Hence, the unperturbed Hamiltonian is given by

$$H_0 = H_{\mathrm{kin}} + H_{\mathrm{hfs}} + H_{\mathrm{Z}} \ , \tag{1.22}$$

where H_{kin} represents the kinetic energy of the atom, H_{hfs} is the term due to the hyperfine interaction and H_{Z} due to the Zeeman effect [2]. These terms act only on the individual atoms at large internuclear distances, larger than the scattering lengths, where the interactions between the atoms are negligible and f_1 and f_2 and

---

[2] Throughout this thesis, $\vec{\imath}$ represents the nuclear spin quantum number of an atom and not the imaginary unit. The imaginary unit is represented by the "imath" symbol in latex.

m_{f1} and m_{f2} are good quantum numbers at low magnetic fields close to zero. The inset in figure 1.4 shows the various hyperfine levels of the asymptotic part of the potential

At smaller internuclear distances compared to the scattering length, the interaction between the atoms become important. Within this region, at relatively large distances (equal to the Van-der Waals length which is about a few tens of Bohr radii for the alkali atoms considered in this thesis), the interaction is dominated by the attractive Van der Waals interaction which has already been explained before. As the distance becomes smaller, the dipole-dipole interaction and the exchange interaction become relevant which will be explained below and which are mainly responsible for the inelastic two-body losses from the trap. At very small distances, the electron clouds repel each other due to the Coulomb interaction and the potential is dominated by the large repulsive interaction as shown in figure 1.4. Hence, the interaction Hamiltonian can be written as

$$H_{\text{int}} = H_{\text{VDW}} + H_{\text{dd}} + H_{\text{ex}} + H_{\text{C}} \ , \tag{1.23}$$

where H_{VDW} represents the Van der Waals interaction, H_{dd}, the dipole-dipole interaction, H_{ex}, the exchange interaction and H_{C}, the Coulomb interaction.

Spin Exchange Interaction

Spin exchange [61] occurs when the charge electron clouds overlap and where the hyperfine interaction and the exchange interaction are comparable. At very short internuclear distances, the electron and nuclear spins decouple and $\vec{S} = \vec{s_1} + \vec{s_2}$ and $\vec{I} = \vec{i_1} + \vec{i_2}$ become relevant quantum numbers resulting in the singlet and the triplet states. When the hyperfine interaction comes into play, the $m_F = m_{f1} + m_{f2}$ is a good quantum number and needs to be conserved. Here, m_F is the projection of the total spin ($\vec{F} = \vec{f_1} + \vec{f_2}$) on the quantization axis. In the spin exchange process, two colliding atoms with initial spins m_1 and m_2 have final spins m_3 and m_4 after the collision such that $m_1 + m_2 = m_3 + m_4$. The interaction involved in this process is very strong and leads to a significant two-body loss rate (the rate depends on the particular species). The exchange potential is given by

$$V_{\text{ex}} = C_{\text{ex}} e^{-r/r_{\text{ex}}} \ , \tag{1.24}$$

where C_{ex} represents the interaction strength and depends upon the splitting between the singlet and the triplet states. Here, r_{ex} represents the range of the interaction, it falls off exponentially with distance as the overlap between the atom clouds decreases. Since, for this process m_F needs to be conserved, this process does not take place for the stretched states where $f, m_f = \pm f$. Hence, these are usually the preferred states for producing condensates due to absence of two body losses due to spin exchange. Moreover, the exchange is proportionally high when the singlet and triplet splittings are large or in other words, the scattering lengths of these two states differ by a large amount. In the case of ^{87}Rb atoms, this splitting is very small and hence, the loss of atoms due to a spin exchange two-body process is proportionally low in ^{87}Rb [62].

Dipolar Relaxation

Dipolar relaxation [63, 64] is a relatively weak interaction when compared to the spin exchange process (about two orders of magnitude smaller) but is the reason for two body losses in the stretched states because of different selection rules wherein $m_F = m_{f1} + m_{f2}$ need not be conserved and the value of Δm_F can change by a maximum value of ± 2. Here, the selection rules are given by $\Delta m_l + \Delta m_f = 0$ and $\Delta l = 0, \pm 2$. The dipolar relaxation occurs due to two processes, the magnetic dipole dipole interactions between the electron spins of the interacting atoms and the second order spin-orbit interaction. The first term is dominant among lighter alkali atoms whereas the second one is dominant among the heavier alkali atoms viz Rb and Cs. Both the processes can be written in a similar form with a variation in the interaction strength. The total Hamiltonian due to the dipole-dipole interaction can be written as [65]

$$H_{\mathrm{dd}} = D_{\mathrm{dd}}(r) \left[s_1 \cdot (3\hat{r}\hat{r} - 1) \cdot s_2 \right] \ , \tag{1.25}$$

where $\hat{r}$ represents the direction of the internuclear axis and $D_{\mathrm{dd}}(r)$ is given by

$$D_{\mathrm{dd}}(r) = -\alpha^2 \left(\frac{1}{r^3} - C_{\mathrm{SO}} e^{-\gamma(r - r_s)} \right) \ , \tag{1.26}$$

where α is the fine structure constant. The first term of equation (1.26) is due to the spin-spin dipolar interaction and the second term (exponential term) is due to the second order spin-orbit interaction where C_{SO} represents the strength of the interaction and γ is the decay constant of the potential with respect to the internuclear separation. The signs of the two terms are opposite. In the case of Rb, these two effects cancel each other to such an extent that the effective two body dipolar relaxation rate is very low. On the other hand, in Cs, the contribution of the second order spin-orbit interaction term is very large when compared to the spin-spin interaction and therefore dominates the two-body loss process and the dipolar relaxation rate is very high. An enumeration of the known two-body loss rates for Rb and Cs is given in section 1.2.3.

Apart from the two-body losses, inelastic collision losses can occur in the ground state as already mentioned before due to the loss of three atoms. This mechanism is discussed below.

Three-Body Losses

A three-body loss occurs at relatively large densities ($10^{14} - 10^{15}\,\mathrm{cm}^{-3}$) and is usually the main loss mechanism in a condensate. This limits the size of the condensate or in other words the number of atoms in a condensate. This occurs when three atoms collide in such a way that two of them form a dimer and the binding energy E_{bind} released due to the formation of the dimer is distributed between the dimer and the third atom where each receive $E_{\mathrm{bind}}/3$ and $2E_{\mathrm{bind}}/3$ respectively. The binding energy is relatively large (of the order of a few eV) compared to the trapping potential and therefore, both the entities are lost from the trap. Hence, it is termed as a three-body loss or three-body recombination. At large positive values of the scattering lengths of the order of $100\,a_0$ for alkali atoms, the three body loss rate is given by [66, 67]

$$L_3 = \frac{3C_{\mathrm{a}}\hbar a^4}{M} \,, \tag{1.27}$$

where the number 3 in the equation represents the number of atoms lost from the trap, M is the mass and C_{a} is a factor which has a value depending upon whether the atoms are in a condensate or a thermal cloud. Furthermore, as already mentioned before, the three body loss rate depends upon the third power of the density of the sample.

1.2.3 Loss Rates for Rubidium and Caesium

The alkali atoms dealt with in this thesis are Rb and Cs. Cs is trapped in a MOT whereas Rb in a conservative potential, in a magnetic trap and a dipole trap (see chapter 3 and 4). Hence, both cold and ultracold collisions take place. The known cold and ultracold collision loss rates for homonuclear Rb and Cs atoms respectively and heteronuclear Rb-Cs atoms are given in table 1.1. The collisions in a MOT, both conventional and high gradient are dominated by light-induced collisions. Hence, the loss rates depend upon the intensity and detuning of the trapping light. Ground state hyperfine changing collisions also contribute to the loss rates. In a conservative trap, at ultracold temperatures, collisions are ground state collisions, the rates of which are much smaller than the rate of light-induced collisions as is evident from the values given in table 1.1.

1.3 BEC

Bose Einstein condensate (BEC) is a state of matter where a macroscopic occupation of the lowest energy ground state of the trap takes place. The theoretical prediction of the BEC was made based on the Bose statistics [80] by Einstein in [81]. The experimental realization of a BEC in dilute gases has been possible with the advent

Process	Type/Trap	State	Rb	Cs	Rb-Cs
Light-Induced Collisions	Conventional MOT (two-body loss)		10^{-11} – $10^{-12}\,\mathrm{cm}^3/\mathrm{s}$ [68, 69, 70]	10^{-10} – $10^{-12}\,\mathrm{cm}^3/\mathrm{s}$ [71, 72]	$(1.0 \pm 0.6) \times 10^{-10}\,\mathrm{cm}^3/\mathrm{s}$ [73]
	High gradient Cs MOT (two-body loss)			10^{-10} – $10^{-11}\,\mathrm{cm}^3/\mathrm{s}$ [74, 75]	$(1.7 \pm 0.6) \times 10^{-10}\,\mathrm{cm}^3/\mathrm{s}$ [54]
Ground State Collisions	Conservative trap (two-body loss)	Rb $\|2,2\rangle$ Cs $\|4,4\rangle$	$\sim 10^{-15}\,\mathrm{cm}^3/\mathrm{s}$ [63, 64]	$\sim 4 \times 10^{-12}\,\mathrm{cm}^3/\mathrm{s}$ [76], $\sim 4 \times 10^{-13}\,\mathrm{cm}^3/\mathrm{s}$ [77]	
	Conservative trap (three-body loss)	Rb $\|2,2\rangle$ Cs $\|4,4\rangle$	$(1.8 \pm 0.5) \times 10^{-29}\,\mathrm{cm}^6/\mathrm{s}$ [66]	$\sim 10^{-25}\,\mathrm{cm}^6/\mathrm{s}$ [78]	
		Rb $\|1,-1\rangle$	$(4.3 \pm 1.8) \times 10^{-29}\,\mathrm{cm}^6/\mathrm{s}$ [79]		

Table 1.1: Loss rate coefficients: The known homonuclear loss rate coefficients for Rb and Cs and the heteronuclear loss rate coefficients for Rb-Cs are displayed. The loss rate coefficients are distinguished based on whether the collisions are light-induced or ground state collisions, the type of trap involved, the number of atoms lost during the collision and the state in which the atom is present in a conservative potential (see text for details).

of the techniques of laser cooling (see chapter 3) and evaporative cooling (see section 3.5.1) and has been demonstrated by several groups [13, 14, 82, 83].

The wave nature of a particle is described in terms of the thermal de Broglie wavelength which is given by

$$\lambda_{\mathrm{dB}} = \left(\frac{2\pi\hbar^2}{M k_{\mathrm{B}} T} \right)^{1/2} , \tag{1.28}$$

where M is the mass of the particle and T is the temperature. This gives the position uncertainty for a particular momentum distribution. For gases, at high temperatures of the order of a few Kelvin, the thermal de Broglie wavelength is very small compared to the inter-particle spacing which is of the order of $n^{-1/3}$ and therefore, the particles obey the classical Maxwell Boltzmann distribution. At sufficiently low temperatures of the order of a few microkelvin, the de Broglie wavelength becomes comparable to the inter-particle spacing and the quantum nature of the particles becomes prominent. An overlap of the individual particle wave functions takes place and the particles are then considered indistinguishable. At a temperature lower than the so called critical temperature, which will be discussed in the next section, a phase transition takes place leading to the macroscopic population of the ground state. This is called a BEC which is an ordered state and exhibits a long range phase coherence. Only bosons can occupy the same state. In the case of fermions it is not possible due to the Pauli exclusion principle. However, fermion pairs (bosons) can form a condensate.

In the following sections, I will discuss the theoretical framework for the description of a BEC. The experimental realizations are discussed in section 3.5 and section 4.2 in a magnetic trap and an optical dipole trap respectively.

1.3.1 Non-Interacting Bose Gas in a Harmonic Potential

The case of a non-interacting Bose gas is an ideal case and is not true for real systems. However, the theory concerning this is discussed here, because many quantities which describe a condensate in dilute gases are close to those for the non-interacting gas. Therefore, in this section, the critical temperature, condensate fraction as well as the density distribution of this non-interacting gas are discussed.

For non-interacting bosons in thermal equilibrium, the mean occupation number of the single particle state ν is given by the Bose distribution which is [84]

$$f\left(E_\nu\right) = \frac{1}{e^{(E_\nu-\mu)/k_\mathrm{B}T} - 1} \,, \tag{1.29}$$

where E_ν is the energy of the single particle state ν and μ is the chemical potential. The chemical potential increases for decreasing temperature and has a maximum value given by E_min which is the zero point energy or the energy of the lowest single particle state. To calculate the atom number and the temperature, the density of states is used. Here, the individual energy level details are smoothed out which leaves out the contribution from the lowest energy state. However, the contribution from the excited states can be studied using this. The density of states for a harmonic oscillator is given by

$$g\left(E\right) = C_d E^{d-1} \,, \tag{1.30}$$

where d is the dimension of the harmonic oscillator. The constant C_d is given by

$$C_d = \frac{1}{(d-1)! \prod_{i=1}^{d} \hbar\omega_i} , \tag{1.31}$$

where ω_i are the trap frequencies of the harmonic trap. Neglecting the zero point energy for large atom numbers (few tens to a few hundred thousand atoms) and integrating the product of the mean occupation number and the density of states over the energy, the number of atoms in the excited state can be calculated. Here, it is assumed that at the critical temperature T_c, all the atoms are still in the excited states. Using equations (1.29), (1.30) and (1.31), the number of atoms in the excited state can be calculated to be

$$N = N_\mathrm{ex} = C_d \Gamma\left(d\right) \zeta\left(d\right) \left(k_\mathrm{B} T_\mathrm{c}\right)^d , \tag{1.32}$$

where $\Gamma\left(d\right)$ and $\zeta\left(d\right)$ are the gamma and Riemann zeta functions respectively. Taking $d = 3$ for a three dimensional (3D) harmonic oscillator potential, the critical temperature is given using the above equation by

$$k_\mathrm{B} T_\mathrm{c} \approx 0.94 \hbar\bar{\omega} N^{1/3} , \tag{1.33}$$

where $\bar{\omega}$ is the geometric mean of the trap frequencies given by $\bar{\omega} = \left(\omega_1\omega_2\omega_3\right)^{1/3}$. The fraction of atoms in the condensate for a temperature T can be calculated using equations (1.29), (1.30) and (1.32) and is given by

$$N_\mathrm{c} = N \left[1 - \left(\frac{T}{T_\mathrm{c}}\right)^3\right] . \tag{1.34}$$

Below the critical temperature T_c, the number of atoms in the excited states is limited and a macroscopic portion of the atoms occupies the ground state indicating the formation of a condensate. An important quantity which describes the state of a gas is the phase space density. It is defined as the particle density within a volume given by the cube of the de Broglie wavelength and is given by

$$\varpi = n \left(\frac{2\pi\hbar^2}{M k_\mathrm{B} T}\right)^{3/2} . \tag{1.35}$$

The phase transition from a thermal gas to a condensate occurs for $\varpi \approx 2.612$. This means that the overlap of the de Broglie wavelength of the individual atoms at large densities marks the beginning of the condensation. Thus, BEC is realized for low temperatures and high particle densities.

For the investigation of cold thermal atoms and condensates and to distinguish them from one another, the density profile is a useful quantity. In an ideal Bose gas, all the atoms occupy the single particle ground state and the many-body ground state

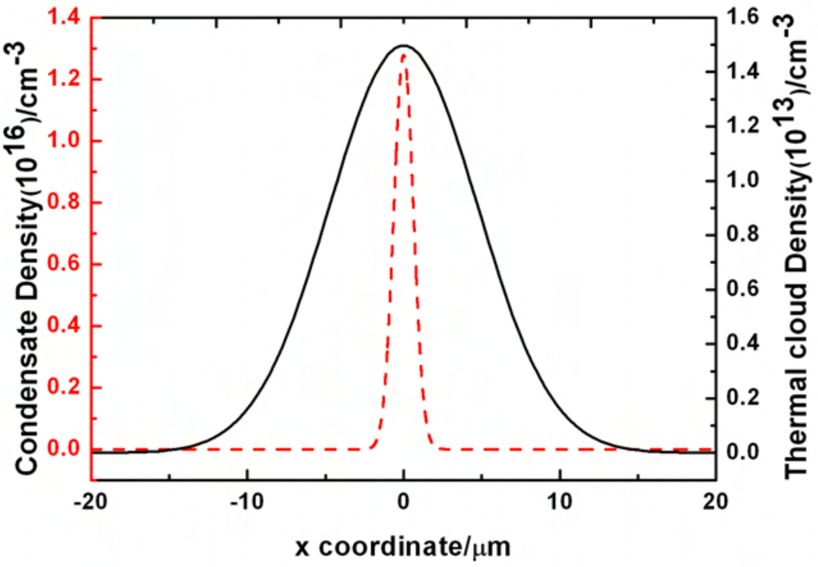

Figure 1.5: The graph shows a cut through the density profile of an ideal Bose condensate (red dashed curve) and a thermal cloud (black curve). As can be seen clearly from the graph, the width of the condensate is much smaller than that of the thermal cloud. Both the curves represent a Gaussian distribution. The curves have been calculated for the trap parameters of our dipole trap (see section 3.7) for a temperature of 200 nK and 10^5 atoms. The peak density of the condensate is three orders of magnitude larger than that of the thermal cloud (as is indicated by the two different scales).

function is the product of N identical single particle wave functions. The density profile for a condensate is given by

$$n(r) = N\,|\xi_0(r)|^2 \;, \tag{1.36}$$

where $\xi_0(r)$ is the ground state wave function. In a 3D harmonic potential, the size of the ground state wave function is given by the oscillator length, which describes the extent or the width of the condensate in the trap. The density profile is therefore given by

$$n(r)_\mathrm{c} = \frac{N}{\pi^{3/2}\prod_{i=1}^{3} b_i} e^{\Sigma_{i=1}^{3} -r^2/b_i^2} \;, \tag{1.37}$$

where $b_i = \sqrt{\hbar/m\omega_i}$ is the oscillator length. On the other hand, the density profile for a thermal cloud is described using the classical Boltzmann statistics and is given by

$$n(r)_\mathrm{th} = \frac{N}{\pi^{3/2}\prod_{i=1}^{3} w_{\mathrm{th}i}} e^{\Sigma_{i=1}^{3} -r^2/w_{\mathrm{th}i}^2} \;, \tag{1.38}$$

where $w_{\mathrm{th}i} = \sqrt{2k_{\mathrm{B}}T/\hbar\omega_i^2}$ is the width of the thermal cloud. The ratio of the width of the thermal cloud to that of the condensate is larger than 1 showing that the thermal cloud is much broader than the condensate. Figure 1.5 shows a cut through the density profiles of a thermal cloud as well as a condensate in the dipole trap (see section 3.7).

1.3.2 BEC in the Presence of Interactions

As already mentioned, real systems are interacting systems. These interactions alter the cloud size as well as the energy per particle. However, the Bose gases are dilute gases which means that the interatomic interaction characterized by the scattering length is of a scale which is much smaller than the inter-particle separation. The system is then considered to be weakly interacting. Such low densities characteristic of a dilute gas are important for the formation of a condensate to increase the lifetime of the metastable gas state by preventing three body collisions, aggregations etc.. However, the densities should be large enough to allow binary elastic collisions required for the process of evaporative cooling. Lower densities also reduce the temperature at which quantum phenomena is observed.

The interactions between the particles can be treated in a mean field approximation, where the interaction of a many-body system is reduced to an interaction between a single body and an external potential. Here, the effective interaction between two particles for weak interactions at low energies is given by

$$U_0 = \frac{4\pi\hbar^2 a}{M} \ , \tag{1.39}$$

where a is the scattering length. The properties of a weakly interacting Bose gas can be described using the time independent Gross-Pitaevskii equation and is given by

$$\frac{-\hbar^2}{2M}\nabla^2\psi(r) + V(r)\psi(r) + U_0 \left|\psi(r)\right|^2 \psi(r) = \mu\psi(r) \ , \tag{1.40}$$

where $\psi(r)$ represents the wave function of the condensate and μ is the chemical potential which is the eigen value of the state. For non-interacting systems, μ is also the energy per particle. For interacting systems, however, this is not the case and the chemical potential is given by

$$\mu = U_0 n \ . \tag{1.41}$$

Considering a 3D harmonic potential, as in the case of the non-interacting Bose gas, the potential and kinetic energies of a condensate with a spatial extent r are given by $V = m\omega^2 r^2/2$ and $Q = \hbar^2/2Mr^2$ respectively for an isotropic trap where ω represents the trap frequency. For large values of R, the kinetic energy term is therefore, very small. For repulsive interactions, the potential minimum is further

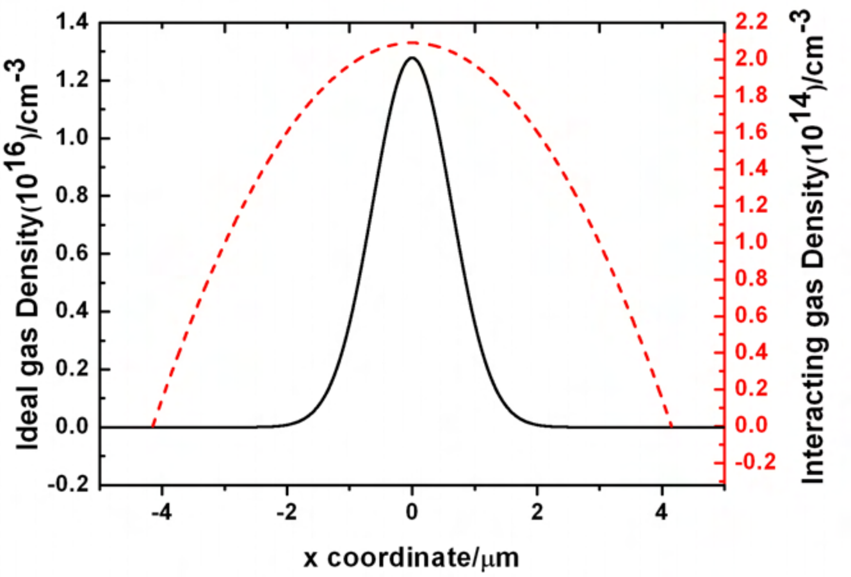

Figure 1.6: The graph shows a cut through the density profile of an ideal Bose condensate (black curve) and a weakly interacting Bose condensate (red dashed curve). The density profile of the ideal condensate is a Gaussian whereas that of the interacting condensate is a parabola according to the Thomas-Fermi approximation. As can be seen from the figure, the condensate is broader in the presence of interactions. The profiles have been calculated for the trap frequencies of our dipole trap (see section 3.7) for a temperature of 200 nK and 10^5 atoms. Also clear from the figure is that the peak density in the interacting case is two orders of magnitude smaller than in the ideal case due to repulsive interactions (note the difference in the two scales).

shifted to larger values of r and hence for large atom numbers in the condensate, the kinetic energy term can be neglected. Hence, the Gross-Pitaevskii equation can be solved in the Thomas-Fermi approximation without the kinetic energy term. This gives exact solutions of the ground state wave function for large values of N. The solution is given by

$$n(r) = |\psi(r)|^2 = [\mu - V(r)] / U_0 \, . \tag{1.42}$$

Since, the Right Hand Side (RHS) of the equation should be positive, the maximum value of $V(r)$ is given by μ. Hence, $V(r) = \mu$ represents the boundary of the cloud, since the wave function is zero outside this region. Using the expression for the potential for an anisotropic harmonic oscillator, the spatial extent of the cloud in the Thomas-Fermi approximation is given by

$$w_{\mathrm{TF}i}^2 = \frac{2\mu}{M\omega_i^2} \, . \tag{1.43}$$

The corresponding density distribution of the condensate is given by

$$n_{\mathrm{TF}} = \frac{\mu}{U_0}\left(1 - \Sigma_{i=1}^{3}\frac{r_i^2}{w_{\mathrm{TF}i}^2}\right) \ . \tag{1.44}$$

This is a parabola in contrast to the Gaussian distribution obtained for an ideal Bose gas. The chemical potential can be written in terms of the total atom number and the trap frequencies and is given by

$$\mu = \frac{15^{2/5}}{2}\left(\frac{Na}{\bar{b}}\right)^{2/5}\hbar\bar{\omega} \ , \tag{1.45}$$

where $\bar{\omega}$ is the geometric mean of the trap frequencies and $\bar{b} = \sqrt{\hbar/m\bar{\omega}}$. Using this in the expression for the width of the cloud shows that the width in the presence of interactions is larger than that in the absence of interactions by a factor that is $\propto (Na/\bar{b})^{1/5}$. The Thomas-Fermi radii for the BEC in our dipole trap is given by $R_1 = 4\,\mu$m, $R_2 = 12\,\mu$m and $R_3 = 6\,\mu$m. The density distributions of the BEC is shown for both the ideal case as well as the Thomas-Fermi case in figure 1.6. Since, the condensates in our case have atom numbers of the order of 10^5 atoms, the condensate fraction is well described by the parabola.

In this chapter, the theoretical framework of cold and ultracold collisions and the theory describing a condensate have been discussed. This has been used to study and interpret the collisions between a single Cs atom and an ultracold Rb gas. The experimental details and results are given in chapter 5. In the future, this will be used to investigate the coherent ground state interactions between a single Cs atom and a Rb BEC.

2 Coherent Control of Spin Degrees of Freedom

The experiments discussed in this thesis involve the preparation of Rb atoms in various Zeeman split hyperfine states in the optical dipole trap and therefore requires the manipulation of these states by a coherent radiation field. Particularly, the magnetically insensitive $m_f = 0$ state is important in our case because the Rb atoms are not pushed out from this state due to the high magnetic field gradient of 300 G/cm of the Cs MOT during the interaction between the two entities. The coherent manipulation of the states is achieved through a microwave and RF radiation field. The experimental details will be discussed in chapter 4. In this chapter, I will discuss the theoretical framework used to describe this coherent manipulation.

The atomic system involved can be considered as a two level system depending upon four parameters viz. the coupling strength of the two levels under consideration, the splitting between the neighbouring Zeeman split hyperfine levels and the frequency and spectral width of the radiation field. If the coherent radiation field has a frequency which is almost at resonance with the transition frequency between the two levels and if the field is monochromatic in nature such that the spectral width of the radiation is smaller than the splitting of the Zeeman levels, then the two level approximation is valid. A quantitative discussion is done in chapter 4. This leads to a coupling of only two levels with this field with negligible effect on the other levels. This interaction of the radiation field with the two level atom is analogous to that of a spin 1/2 in a magnetic field, first demonstrated by Bloch in [85]. The spin 1/2 particle has exactly two levels. However, the assumption made in the case of an atom is good enough for the analogy. The equations for the spin vector developed by Bloch for magnetic resonance can therefore be generalized to the case of a two level system interacting with an external radiation field. These equations are called Bloch equations and the optical counterpart are called the optical Bloch equations where the concept of a pseudospin vector has been introduced. The components of this vector describe the population of the different states and the dipole moment. The rotation of this vector on a sphere, also known as the Bloch sphere describes all possible states of the spin 1/2 particle. The Bloch sphere is therefore, a good illustration of the interaction of the atom with the radiation field. Depending upon the duration of the external radiation, the oscillations of the populations between the two states which are the so called Rabi oscillations demonstrated in [86], can be visualized on the Bloch sphere.

The two level atom and its interaction with an external radiation field have been studied in various textbooks [87, 88, 89]. I will only briefly discuss the interactions and the temporal evolution of this system using the Bloch vector model. In this context, the optical Bloch equations will be briefly explained in section 3.1 followed by the Rabi flopping in section 3.2.

2.1 Optical Bloch Equations

The interaction of a radiation field with the atom can be studied by the semiclassical theory [87]. The Hamiltonian of such a system can be written as the sum of the unperturbed Hamiltonian of the atom and the scalar product of the dipole moment operator and the electric field operator of the radiation as

$$\hat{H} = \hat{H}_\mathrm{A} - \hat{\mu_\mathrm{d}} \cdot \hat{W} \ , \tag{2.1}$$

where $\hat{H}$ is the Hamiltonian of the interacting atom, $\hat{H}_\mathrm{A}$ is the unperturbed Hamiltonian, $\hat{\mu_\mathrm{d}}$ is the dipole moment operator and $\hat{W}$ is the electric field operator. The $\hat{H}_\mathrm{A}$ and $\hat{\mu_\mathrm{d}}$ operators can be written in matrix form such that

$$\hat{H}_\mathrm{A} = \begin{pmatrix} E_+ & 0 \\ 0 & E_- \end{pmatrix} \ , \tag{2.2}$$

$$\hat{\mu_\mathrm{d}} = \begin{pmatrix} 0 & \mu_{\mathrm{d}r} + \imath\mu_{\mathrm{d}\imath} \\ \mu_{\mathrm{d}r} - \imath\mu_{\mathrm{d}\imath} & 0 \end{pmatrix} \ , \tag{2.3}$$

where the $+$ and $-$ refer to the two levels with eigenstates $|+\rangle$ and $|-\rangle$ corresponding to $\hat{H}_\mathrm{A}$ and E_+ and E_- being the corresponding energies. The dipole matrix elements are complex in nature in general. Introducing the Pauli matrices $\hat{\sigma_\mathrm{p}}$, the Hamiltonian and dipole moment operator can be written as

$$\hat{\mu_\mathrm{d}} = \mu_{\mathrm{d}r}\hat{\sigma_{\mathrm{p}1}} - \mu_{\mathrm{d}\imath}\hat{\sigma_{\mathrm{p}2}} \ , \tag{2.4}$$

$$\hat{H}_\mathrm{A} = \frac{1}{2}\left(E_+ + E_-\right)\hat{I_\mathrm{U}} + \frac{1}{2}\left(E_+ - E_-\right)\hat{\sigma_{\mathrm{p}3}} \ , \tag{2.5}$$

where $\hat{I_\mathrm{U}}$ is the 2×2 unity matrix operator. The time dependence of this atomic system can be determined using the Heisenberg equation of motion for the operator $\hat{\sigma_\mathrm{p}}$ which is given by

$$\imath\hbar\dot{\hat{\sigma_\mathrm{p}}} = [\hat{\sigma_\mathrm{p}}, \hat{H}] \ , \tag{2.6}$$

where $\hat{H}$ is the total Hamiltonian of the system which is given by substituting equations (2.4) and (2.5) in equation (2.1). Using the expression for the total Hamiltonian and the dipole moment operator, the pauli matrix operators follow the equations

$$\dot{\widehat{\sigma_{\mathrm{p1}}}}(t) = -\omega_{\mathrm{t}}\widehat{\sigma_{\mathrm{p2}}}(t) + \frac{2}{\hbar}\left[\mu_{\mathrm{d}\imath} \cdot \hat{W}(t)\right]\widehat{\sigma_{\mathrm{p3}}}(t)\ , \tag{2.7}$$

$$\dot{\widehat{\sigma_{\mathrm{p2}}}}(t) = \omega_{\mathrm{t}}\widehat{\sigma_{\mathrm{p1}}}(t) + \frac{2}{\hbar}\left[\mu_{\mathrm{d}r} \cdot \hat{W}(t)\right]\widehat{\sigma_{\mathrm{p3}}}(t)\ , \tag{2.8}$$

$$\dot{\widehat{\sigma_{\mathrm{p3}}}}(t) = -\frac{2}{\hbar}\left[\mu_{\mathrm{d}r} \cdot \hat{W}(t)\right]\widehat{\sigma_{\mathrm{p2}}}(t) - \frac{2}{\hbar}\left[\mu_{\mathrm{d}\imath} \cdot \hat{W}(t)\right]\widehat{\sigma_{\mathrm{p1}}}(t)\ . \tag{2.9}$$

Here

$$\omega_{\mathrm{t}} = \frac{E_{+} - E_{-}}{\hbar}\ , \tag{2.10}$$

represents the atomic transition frequency. The operator nature of the atom and the field make the equations quite complex without any general solutions. However, this set of equations would yield solutions if the operator nature of the variables does not exist. The semiclassical treatment can be applied in this case of a two level atom if we ignore the quantum correlations between the atom and the field, which is actually unimportant in this case. The operator products can then be factored such that

$$\langle \hat{W}(t)\widehat{\sigma_{\mathrm{p3}}}(t)\rangle = \langle \hat{W}(t)\rangle\langle\widehat{\sigma_{\mathrm{p3}}}(t)\rangle\ . \tag{2.11}$$

Replacing the operators by their expectation values in equations (2.7) to (2.9) yields three equations for the expectation values of the Pauli matrices, which represent the interactions of the two level atom with the radiation field. For convenience, from now on the notation $q(t) \equiv \langle\hat{\sigma_{\mathrm{p}}}(t)\rangle$ is used for the pseudospin vector.

Having written the equations in terms of the pseudospin describing the two level atom in the radiation field, we can now interpret the physical significance of each component of this pseudospin vector. Substituting the relation for the atomic transition frequency (2.10) in the total energy of the system and considering $\frac{1}{2}\left(E_{+} + E_{-}\right)$ as the zero of energy, the internal energy of the atom can be written as

$$E_{\mathrm{I}} = \frac{1}{2}\hbar\omega_{\mathrm{t}}q_3(t)\ . \tag{2.12}$$

Equation (2.4) also shows that $q_1(\mathrm{t})$ and $q_2(\mathrm{t})$ are related to the atom's dipole moment. Therefore, we can say that, physically, the components of the pseudospin represent the population difference (given by q_3) as well as the dipole moment (q_1 and q_2). If we consider only the $\Delta m = 0$ transition, then the dipole matrix element can be expressed without its complex part. This simplifies the pseudospin vector equations by setting $\mu_{\mathrm{d}\imath} = 0$.

Applying the Rotating Wave Approximation (RWA), where the fast rotating terms are neglected and transforming the equations to a coordinate system rotating with the angular velocity ω_f of the applied field, the following rotation matrix is introduced

$$\begin{pmatrix} u \\ v \\ w \end{pmatrix} = \begin{pmatrix} \cos\omega_\mathrm{f}t & \sin\omega_\mathrm{f}t & 0 \\ -\sin\omega_\mathrm{f}t & \cos\omega_\mathrm{f}t & 0 \\ 0 & 0 & 1 \end{pmatrix} \begin{pmatrix} q_1 \\ q_2 \\ q_3 \end{pmatrix} , \tag{2.13}$$

where u, v and w are the components of the stationary pseudospin vector ρ in the new frame of reference[1]. The equations of motion obeyed by the pseudospin vector can be written as

$$\dot{u} = \Delta v \ , \tag{2.14}$$

$$\dot{v} = -\Delta u + \Omega_\mathrm{R} w \ , \tag{2.15}$$

$$\dot{w} = -\Omega_\mathrm{R} v \ , \tag{2.16}$$

where Δ is the detuning of the radiation field frequency with respect to the atomic transition frequency and Ω_R is the Rabi frequency at resonance. The Rabi frequency is also a measure of the coupling strength of the atom radiation interaction. The above equations can be written as a single equation

$$\frac{d}{dt}\rho = \Omega \times \rho \ , \tag{2.17}$$

where Ω is the torque vector in this frame. The physical significance of u, v and w are the same as that of q_1, q_2 and q_3. Here, w represents the population difference, whereas u and v are the in phase and quadrature terms of the atomic dipole moment, respectively. Hence, the above equations describe quite well a two level system in a coherent radiation field. The pseudospin vector described in equation (2.17) traces an orbit on a unit sphere (Bloch sphere) for the case where no damping is present. The rotation of this vector with respect to the duration of the radiation pulse on a Bloch sphere is shown in the next section.

2.2 Rabi Oscillations

In this section, the solutions of the Bloch equations introduced in the previous section will be presented for an atom in a coherent radiation field, which is in our specific case the microwave radiation or the RF radiation. The general solution of this problem which describes the oscillations in the populations between the two states for a detuning $\Delta = \omega_\mathrm{f} - \omega_\mathrm{t}$, is given by [87]

$$w(t,\Delta) = -1 + \frac{2{\Omega_\mathrm{R}}^2}{{\Omega_\mathrm{R}}^2 + \Delta^2} \sin^2 \sqrt{{\Omega_\mathrm{R}}^2 + \Delta^2}\frac{t}{2} \ , \tag{2.18}$$

---

[1] In this chapter, u, v and w are the components of the stationary pseudospin vector ρ. In the rest of the thesis, v is the velocity of the atoms and w represents the widths of the atomic clouds. u has been introduced as the radial wave function in chapter 1

where it is assumed that the atom is initially in its ground state. The generalized Rabi frequency is given by

$$\Omega(\Delta) = \sqrt{\Delta^2 + {\Omega_\mathrm{R}}^2} \,. \tag{2.19}$$

This is the frequency with which the atoms flip from the ground to the excited state and vice versa resulting in oscillations known as Rabi oscillations.

Considering the case where $\Delta = 0$, i.e. when the external field is in resonance with the atomic transition frequency, the solutions of the Bloch equations can be written as

$$u(t,0) = u_0 \,, \tag{2.20}$$

$$v(t,0) = w_0 \sin\theta_\mathrm{B}(t) + v_0 \cos\theta_\mathrm{B}(t) \,, \tag{2.21}$$

$$w(t,0) = -v_0 \sin\theta_\mathrm{B}(t) + w_0 \cos\theta_\mathrm{B}(t) \,, \tag{2.22}$$

where a quantity θ_B has been introduced which represents the rotation angle of the Bloch vector and is given by

$$\theta_\mathrm{B}(t) = \int_0^t \Omega_\mathrm{R}(t')\,dt' \,. \tag{2.23}$$

The rotation of this vector through a particular angle is equivalent to the area of the pulse of the radiation field. Let us consider two cases.

$\pi/2$ Pulse

This corresponds to rotation of the Bloch vector by an angle $\theta_\mathrm{B} = \pi/2$ and a pulse duration equal to $\pi/2$ which gives the corresponding components

$$v(t,0) = w_0 \,, \tag{2.24}$$

$$w(t,0) = -v_0 \,. \tag{2.25}$$

This means that there exists a superposition of the states if the system is initially in either the ground state or the excited state due to a flipping of the components v and w after a time corresponding to a $\pi/2$ pulse has elapsed. The Bloch vector is then in the horizontal plane of the Bloch sphere as shown in figure 2.1.

π Pulse

This corresponds to $\theta_\mathrm{B} = \pi$, which gives the following components

$$v(t,0) = -v_0 \,, \tag{2.26}$$

$$w(t,0) = -w_0 \,. \tag{2.27}$$

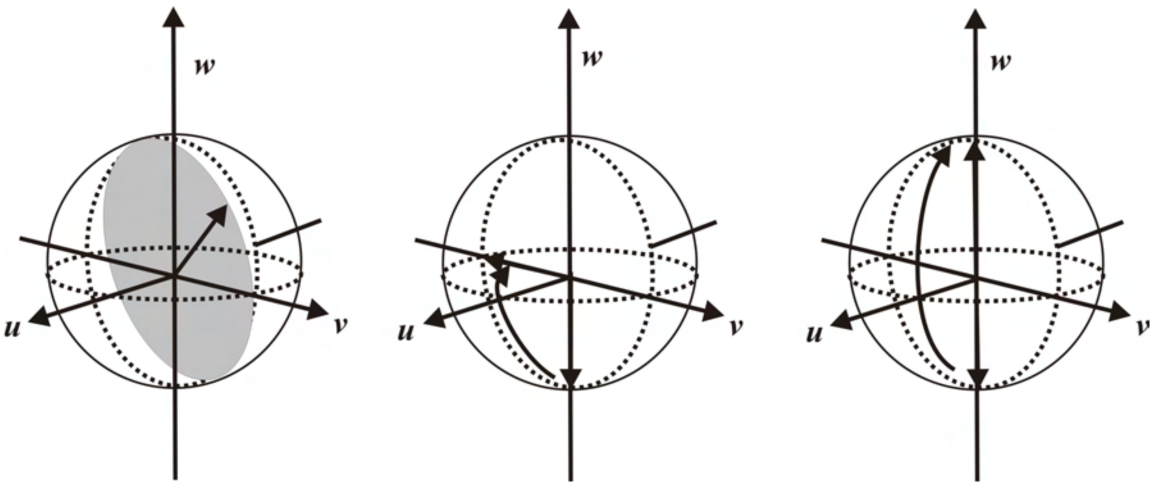

Figure 2.1: The rotation of the Bloch vector ρ on the Bloch sphere is shown. Here, u, v and w correspond to the components of the Bloch vector. The leftmost figure shows the rotation of the Bloch vector about u for a given angle θ_{B} at resonance. The middle figure shows the flipping of the Bloch vector onto the horizontal plane for a $\pi/2$ pulse and the rightmost shows the complete flipping from -w to +w for a π pulse.

This means that the system flips between the ground and the excited state such that if it is initially in the ground state then a complete population transfer occurs to the excited state after a time corresponding to a π pulse.

However, a complete population transfer occurs only for a resonant pulse. In the general case, the detuning Δ changes the amplitude as well as the frequency of these oscillations as already evident from equation (2.18).

Decay Constants

The Bloch equations given in (2.14)-(2.16) are not enough to describe real atomic systems because of the presence of finite decay constants. Two different decay constants have been associated with the population term w and the dipole moment terms u and v known as the longitudinal and transverse decay constants, respectively. This is because there are interactions which can affect the dipole oscillations but leave the energy unchanged. The corresponding longitudinal and transverse decay times are given by T_1 and T_2, respectively. The longitudinal decay time corresponds to the spontaneous emission rate of the atomic level. The transverse decay time has two components, one which arises due to processes which affect all the atoms homogeneously, for example, during collisions and the other which is due to the different velocities of the individual spins in an ensemble, leading to dephasing which is an inhomogeneous effect. The total transverse decay time can then be written as

$$\frac{1}{T_2} \equiv \frac{1}{{T_2}'} + \frac{1}{{T_2}^\star} \;, \tag{2.28}$$

where ${T_2}'$ is the homogeneous decay time and ${T_2}^\star$ is the inhomogeneous decay time. Adding the decay constants to the Bloch equations therefore, results in the following corrected equations [87]

$$\dot{u} = \Delta v - \frac{u}{{T_2}'} \tag{2.29}$$

$$\dot{v} = -\Delta u + \Omega_\mathrm{R} w - \frac{v}{{T_2}'} \;, \tag{2.30}$$

$$\dot{w} = -\Omega_\mathrm{R} v - \frac{w - w_\mathrm{eq}}{T_1} \;, \tag{2.31}$$

where w_eq is the value at equilibrium when the field amplitude is zero.

3 Preparation of an Ultracold Rb Gas and a Single Atom Cs MOT

This thesis focusses on the interaction between an ultracold Rb gas and a single atom Cs MOT. These two entities represent a many body system and a few body system respectively. For example, an ultracold gas of Rb, has temperatures of the order of a few hundred nanokelvin with about a few hundred thousand atoms, whereas a single atom Cs MOT has a temperature of about a hundred microkelvin with one or a few atoms. The processes involved in the preparation of the two differ. This chapter deals with the various steps involved in the preparation of a Rb BEC in a magnetic trap and a single atom Cs MOT, which includes a brief description of the experimental setup. Apart from the preparation of these species, the two entities are also analyzed differently. Therefore, the imaging and detection techniques are also briefly discussed.

3.1 Vacuum Setup

The main part of the apparatus consists of a double MOT system shown in figure 3.1, which includes a vapour cell MOT and an Ultra High Vacuum (UHV) MOT. A description of the MOT is given in section 3.3. This kind of a setup is a trade off between collection of a large number of atoms and achievement of a good vacuum to minimize background gas collisions for a larger lifetime of the atoms. In our experiment, therefore, about 10^9 atoms are first collected in the vapour cell MOT from a Rb reservoir and then transferred using a near resonant light beam via radiation pressure to the UHV MOT. The glass cell is placed in this region and it is here that all the experiments including the condensation of Rb and Rb-Cs interactions take place. The preparation of a BEC via evaporative cooling (see section 3.5.1) has a duration of a few tens of seconds in our case, and therefore, a good vacuum ($\sim 10^{-10} - 10^{-11}$ mbar) is required in this UHV region to maintain a lifetime larger than this. In our experiment, the thermal clouds have a lifetime of about 120 s. Furthermore, the BEC needs to be stored in this region for experiments involving Rb and Cs.

The vacuum in our setup is achieved through a combination of an ion getter pump (Model Number:Varian, VacIon Plus 300; Pump speed: 230 l/s) and a Titanium

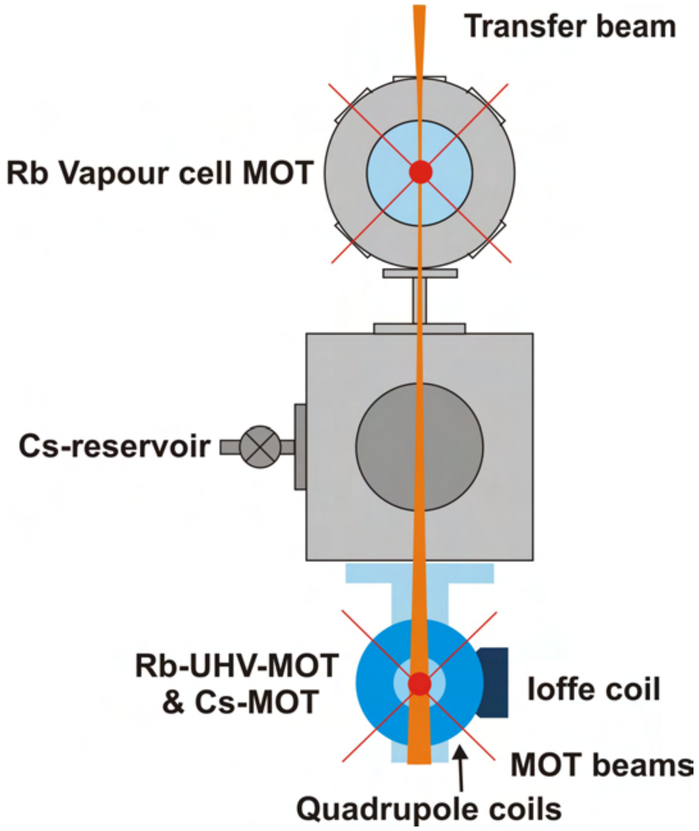

Figure 3.1: A schematic of the double MOT setup is shown. The two MOTs are vertically separated by a distance of 60 cm. The Rb atoms are transferred to the UHV region by the transfer beam (orange). The square in the middle represents the vacuum setup which is connected to the upper MOT by a differential pumping tube. The coil system is shown (quadrupole coil (blue toroid) and Ioffe coil) along with two of the MOT beams (red). Also shown, is the Cs reservoir which is flanged to the UHV region.

Sublimation Pump (TSP). The TSP acts as an additional pump, they have a higher pumping speed for active gases. This was implemented into the set up after the former turbo-molecular pump responsible for maintaining the vacuum suddenly broke down. A valve separated the main chamber (UHV region) from the turbo pump, which was closed to avoid atmospheric pressure at the main chamber during the breakdown. This area was therefore, maintained at a pressure of 10^{-5} mbar and the new vacuum setup was flanged behind this valve. Unlike the turbo pump, the ion pump has no moving parts and therefore creates no vibrations at the experiment. Ion pumps use high voltages of $\sim$ 3-7 kV to induce cathode emissions. High magnetic field strengths of the order of a few Tesla, required for the pumping action create stray magnetic fields in the vicinity of the ion pump. In our case, the ion getter pump is flanged 100 cm away from the chamber which produces negligible stray magnetic fields at the chamber. The pumping speed at the chamber is ∼ 187 l/s. The new vacuum setup was first pumped out using a turbo-molecular pump station and the ion pump and subsequently baked out leading to a pressure of 10^{-10} mbar at the main chamber after the valve was opened. A pressure of 10^{-11} mbar was achieved by cooling the TSP with liquid nitrogen leading to freezing out of residual gases and subsequent bake outs with the valve closed.

The vapour cell MOT (upper MOT) and the UHV MOT (lower MOT) are connected by a differential pumping tube, which is 8 mm in length and has an inner diameter of 3 mm. Due to the small dimensions of this tube, the upper MOT chamber is pumped much less efficiently than the UHV region and therefore has a comparatively higher pressure of 10^{-9} mbar. This however, serves our purpose of loading a large number of atoms from the Rb reservoir as mentioned before. Due to the small number of Cs atoms required for our experiments, the Cs atoms are loaded directly into the UHV chamber from the Cs reservoir.

3.2 Laser Setup

Lasers constitute an important part of our experimental setup. Near resonant light is used for cooling the atoms through radiation pressure [1, 90] as well as for confining them. A laser beam is also used for optically pumping the atoms to a particular Zeeman split hyperfine level for magnetic trapping. They also find use in absorption imaging as well as fluorescence detection making it possible to analyze both the species. Laser is also used for optically trapping the atoms as in the case of a dipole trap. In the following sections, the Rb and Cs laser setups are briefly discussed. The dipole trap will be discussed in section 3.7.

For Rb as well as Cs, the D_2 lines having wavelengths 780 nm and 852 nm for Rb and Cs respectively, have closed transitions which are required for cooling. The natural line width of the D_2 line is $2\pi \times 6.06\,\mathrm{MHz}$ ($2\pi \times 5.22\,\mathrm{MHz}$) for Rb (Cs). The lasers operating at the wavelengths corresponding to both the species are External Cavity Diode Lasers (ECDL) in the Littrow configuration [91]. These lasers have a linewidth of $< 1\,\mathrm{MHz}$. However, the need for near resonant light to drive a closed transition, requires active stabilization of the laser frequency to compensate for drifts larger than the natural linewidths of the atomic transitions, in the central frequency of the laser. This is achieved through polarization spectroscopy [92] or a Dichroic Atomic Vapour Laser Lock (DAVLL) [93, 94] by sending a feedback to the laser. Saturation spectroscopies [95] are built for all the lasers as a reference for the different resonant and crossover transitions. The light from the lasers passes through various optical elements, pinholes and Accousto-Optic Modulators (AOMs), this is discussed briefly in the next part. Any drift in any of these elements would lead to a misalignment of the laser beams at the experiment. In order to avoid this, the light is coupled into single mode polarization maintaining optical fibers and coupled out at the main experiment. Therefore, any drifts would only decrease the coupling efficiency of the fiber and not change the position of beams. As an improvement to the existing setup, some of the fibers were replaced with new ones which were configured by us in the lab with FC/APC fiber connectors. The new fibers and the FC/APC fiber connectors (Schaefter and Kirchoff) are more stable and more efficient ($65 - 80\%$ coupling efficiency) than the old fibers ($40 - 50\%$ coupling efficiency) and the fiber connectors, where about 1 cm of the fiber tip hung freely in the air. All the lasers pass through mechanical shutters before they are coupled into the fibers. These shutters are computer controlled and allow the switching ON or switching OFF of the different lasers independently during the experimental run. The Cs as well as the Rb laser systems are placed in a box to protect them from temperature fluctuations and dust.

3.2.1 Rb Setup

The Rb setup consists of four lasers which are discussed below.

a) Cooling Beam : This laser is used for driving the closed transition between the hyperfine states, $f = 2$ of the ground state and $f' = 3$ of the excited state, required for cooling. The term scheme for Rb is given in [96]. Here, the light from the ECDL is amplified using a Tapered Amplifier (TA) system from Toptica with a TA chip (M2K) giving an output of 1 W for a seed laser power of ~ 25 mW. This beam is then divided into two using a Polarising Beam Splitter (PBS) cube to provide cooling light for the two MOTs. Two different fibers are used for the two MOT beams. The power at the output of the fiber coupler for each beam is ~ 70 mW. The cooling light is 15 MHz red detuned from resonance to enable cooling. The cooling light for the lower MOT is also used during various stages of the experiment viz. compression, optical molasses and optical pumping (these processes are described in section 3.4), all of which require a different detuning with respect to resonance. The required detunings are obtained by placing an AOM in double pass configuration [97] in each cooler arm. A different frequency shift is produced each time with the AOM by modulating its acoustic frequency, which is computer controlled. The central frequency of the AOM was chosen to be 225 MHz (bandwidth ±50 MHz) producing a total frequency shift of 450 MHz in this configuration. In order to drive the closed transition, the laser is frequency stabilized to the $f = 2 \rightarrow f' = 1$ transition (~ 424 MHz away from resonance) through polarization spectroscopy. The response time of the AOMs is of the order of a few hundred nanoseconds and therefore, the detuning required for each process is achieved very quickly. This is a big improvement over the earlier setup where the different detunings were obtained by scanning the laser grating. For optical pumping however, an additional AOM is also used to drive the $f = 2 \rightarrow f' = 2$ transition. A part of the cooler light is diverted before it enters the AOM and is overlapped with the transfer beam and the imaging beam in order to provide two beat signals for frequency reference.

b) Repumper Beam : The atoms in the closed transition fall into the $f = 1$ state, which is a dark state in this case, after a few thousand cycles due to off resonant excitations to the $f' = 2$ state. These atoms are pumped back into the cooling transition by the repumper light which is resonant from $f = 1 \rightarrow f' = 2$ state. The repumper laser is also used for pumping the atoms back to the cycling transition during optical pumping. The loading of the UHV MOT as well as the optical pumping is very sensitive to the frequency as well as the mode of the repumper laser. The laser should therefore run stable at single mode and should have negligible frequency drifts. The frequency stabilization is achieved in this case also through polarization spectroscopy, where the laser is locked to the crossover $f = 1 \rightarrow (f' = 2, f' = 1)$ transition. This is done because the dispersive signal in the spectroscopy is larger for this crossover than the resonance transition providing a greater stability to the lock signal. The 78 MHz detuning from resonance is achieved by placing an AOM in the polarization spectroscopy setup. As in the case of the cooler light, the repumper light beam is also split into two by a PBS cube to provide light for the vapour cell as well as the UHV MOT. As in the case of the cooler, two different fibers are used for the two MOTs. The upper repumper has a power of $\sim 2\,\mathrm{mW}$ whereas the lower repumper has a power of $\sim 6\,\mathrm{mW}$ at the fiber output.

c) Imaging Beam : The Rb atoms are observed and analyzed in our setup through absorption imaging (see section 3.6.1). For this purpose, a laser light resonant to the cooling transition is used. Due to the short exposure time of $200\,\mu\mathrm{s}$ required for taking the image, an AOM is used to switch ON the beam while imaging. The AOM is used in single pass configuration and produces a frequency shift of 133 MHz from resonance. The laser is therefore, frequency stabilized to the crossover $f = 2 \rightarrow (f' = 2, f' = 3)$ transition (133 MHz away from resonance) through polarization spectroscopy. After passing through the AOM, the beam is divided into three, using PBS cubes. Two of these parts are used for imaging the Rb atoms in the y and z directions (see figure 3.1). The third part is used for overlapping with the cooler light to produce a beat signal for frequency reference. All the three parts are coupled into three different optical fibers. The imaging beam has a power of $\sim 200\,\mu\mathrm{W}$ in each arm at the fiber output.

d) Transfer Beam : The Rb atoms are transferred from the vapour cell MOT to the UHV MOT by the transfer beam which is $\sim 25\,\mathrm{MHz}$ detuned from the cooling transition. This laser is however, frequency stabilized using a DAVLL which does not have sub doppler resolution as in the case of polarization spectroscopy. As the loading of the UHV MOT is not very sensitive to the detuning of the transfer beam, sub doppler spectroscopy is not inevitable in this case. The transfer beam has a power of $\sim 700\,\mu\mathrm{W}$. A part of the transfer beam is diverted, before it is coupled into the fiber, to overlap with the cooler laser to create a beat signal for frequency reference.

3.2.2 Cs Setup

The Cs laser setup is similar to the Rb laser setup with a few exceptions. This setup consists of just two lasers. The transfer beam is not required here as the Cs atoms are loaded directly into the UHV MOT. Since the Cs atoms are detected by the fluorescence detection technique, an imaging beam for absorption imaging is also not required. All the lasers are frequency stabilized through polarization spectroscopy. The entire setup is built on another optical table.

a) Cooling Beam : The cooling beam here serves the same purpose as in the case of Rb. This is driven on the closed transition $f = 4$ of the ground state and $f' = 5$ of the excited state. The Cs term scheme is shown in [98]. The cooling beam is derived from a TA system from Sacher Lasertechnik which gives an output power of 500 mW. The earlier interspecies experiments conducted viz. sympathetic cooling of Cs by Rb [52], required a higher Cs cooling power ($\sim 50\,\mathrm{mW}$) because of $\sim 10^7$ Cs atoms involved in the process. The experiments with few or single atoms do not require such high powers. The setup remains the same, however, the desired power is obtained by varying the intensity of the laser light with a retardation plate and a PBS cube and by operating the TA system at a lower current. The power at the fiber output is $\sim 1\,\mathrm{mW}$. An AOM in double pass configuration is placed in the cooler beam. This AOM is computer controlled and is used to obtain different detunings (frequency modulation) and power outputs (amplitude modulation) during the experimental run to control the Cs atom number as well as the fluorescence signal obtained per atom. The AOM introduces a total frequency shift of 450 MHz. In order to drive the cooling transition, the laser frequency is therefore stabilized to the $f = 4 \rightarrow f' = 3$ transition.

b) Repumper Beam : The repumper beam is resonant to the transition $f = 3 \rightarrow f' = 4$. This pumps atoms which fall into the dark state $f = 3$ back into the cooling cycle. The repumper beam is overlapped with the cooler beam with a PBS cube and transmitted via the same fiber to the experiment. The power at the fiber output is $\sim 600\,\mu\mathrm{W}$.

3.3 Magneto-Optical Trap

To achieve quantum degeneracy, the Rb atoms need to be cooled to temperatures of a few 100 nK with a density of $\sim 10^{14}\mathrm{cm}^{-3}$ and an enhancement of the phase space density to a minimum value of ~ 2.612. The Cs atoms in our experiment also need to be trapped at a temperature of $\sim 100\,\mu\mathrm{K}$. Various methods are employed for cooling and trapping atoms. Laser cooling is used as a pre-cooling technique for cooling atoms to a few hundred microkelvin.

The energy levels of the alkali atoms undergo hyperfine splitting [99] due to the interaction of the nuclear spin $\vec{i}$ with the total angular momentum $\vec{j}$ of the electron, such that atomic transitions occur between these levels according to the selection rules $\Delta f = 0, \pm 1$. In a simple 1D case, when the atom in motion encounters light, propagating in the opposite direction (towards the atom), which is red detuned with respect to the atomic transition, the atom absorbs a photon due to the doppler shift of the light frequency towards the atomic resonance. The atom then gets a kick in the direction of the propagation of light leading to its slowing down. Cooling occurs through a radiation pressure force or a dissipative force. This force arises due to the exchange of momentum between the atoms and the light field and is in the low intensity limit given by [100]

$$F_{\mathrm{dis}} = \frac{\hbar k s_0 \Gamma/2}{1 + s_0 + (2(\Delta + \omega_{\mathrm{D}})/\gamma)^2} \,, \tag{3.1}$$

where s_0 is the saturation parameter, Δ is the detuning from the atomic transition, Γ is the natural line width of the atomic transition and ω_{D} is the doppler shift [1]. Scattering of a single photon leads to a very small change in the atomic velocity, given by $\hbar k/M$, which is the recoil velocity and is about a few mm/s. In order to cool atoms from a room temperature of 300 K to about a few hundred microkelvin, around 10^5 cycles of absorption and emission are required on a closed transition. An extension of this simple 1D picture in 3D is the optical molasses [101, 102, 103]. This is formed by two counter propagating beams in all the three directions with the same intensity, frequency and polarization. Atoms moving slowly along the light beams experience a net damping force, given by the sum of the dissipative force in both the directions, which is proportional to their velocity v for small velocities [100]

$$\vec{F_{\mathrm{T}}} = -\beta \vec{v} \,, \tag{3.2}$$

where β is the damping coefficient. However, this cooling does not go till absolute zero as an heating effect in involved due to spontaneous emission in random directions and puts a limit to this cooling given by the Doppler Limit $T_{\mathrm{D}} = \hbar\Gamma/2k_{\mathrm{B}}$, which has value of 145 μK (125 μK) for Rb(Cs), respectively. However, these optical molasses lead only to a cooling of the atoms, trapping requires further modifications or additions.

Trapping is achieved by using circular polarized beams for the light field and by applying an inhomogeneous magnetic field, B. The minimum of the magnetic field coincides with the crossing point of the laser beams. This kind of a trap is called a Magneto-Optical Trap (MOT)[104]. A simple picture in 1D is depicted in figure 3.2. This takes advantage of the Zeeman splitting of the degenerate atomic states. In the simple case of a transition between $j_{\mathrm{g}} = 0 \rightarrow j_{\mathrm{e}} = 1$, the upper hyperfine level is split into three states $m_{\mathrm{e}} = 0, \pm 1$. The $m_{\mathrm{e}} = 1$ state is raised up for $B > 0$, whereas the $m_{\mathrm{e}} = -1$ state is pulled down. Now, for atoms moving to the right, if a σ^- light,

---

[1] Note that, F has been used in chapter 1 for the hyperfine state of a molecular potential. From here on, in the rest of this thesis, F refers to force.

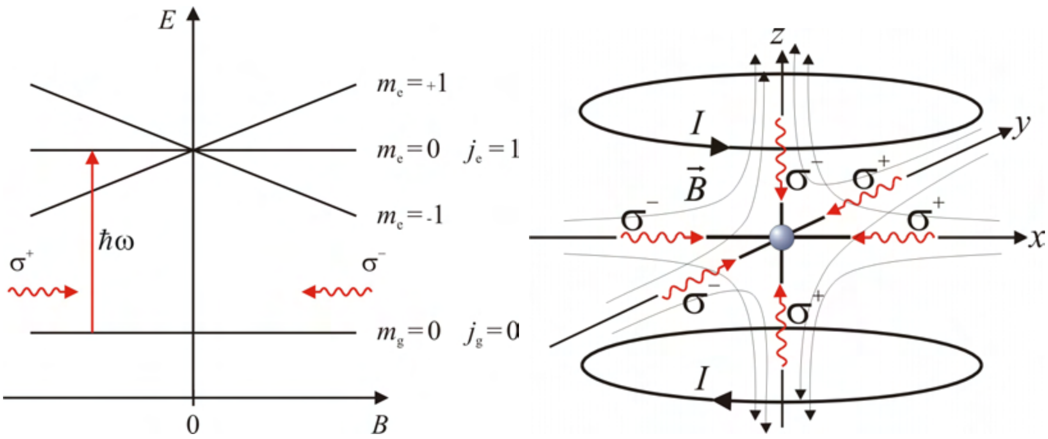

Figure 3.2: The figure on the left shows a 1D picture of the MOT. The upper hyperfine level has three Zeeman states. The two circular polarized light beams σ^+ and σ^- trap the atoms at $B = 0$ (see text). An extension in 3D is shown on the right with circular polarized beams in all the six directions.

red detuned with respect to the atomic transition, propagates towards $B = 0$, the atoms scatter photons of this light and are driven to the centre of the trap ($B = 0$). Similarly, the σ^+ light is scattered more for atoms moving to the left from the trap centre, thereby confining the atoms to the zero magnetic field region. The dissipative force for small field gradients is now given by

$$\vec{F_{\mathrm{T}}} = -\beta\vec{v} - \kappa\vec{r}\,, \tag{3.3}$$

where κ depends on the magnetic field gradient. The temperature in the MOT is comparable to that in optical molasses. However, in optical molasses as well as in the MOT, the various polarizations of the light field lead to sub-doppler cooling [105, 106, 107] resulting in a temperature lower than the Doppler limit. This simple picture for the MOT can be extended to 3D as shown in figure 3.2 as well as for complex hyperfine structures.

In our experiment, we have two MOTs for Rb and one for Cs. The Rb MOTs are typical conventional 3D MOTs. The vapour cell MOT is formed by retro-reflected circular polarized light beams with approximately 25 mW power in each axis with the beams having a diameter of ~ 1.5 cm and a detuning of 15 MHz from the cooling transition. The magnetic field gradient is provided by quadrupole coils in anti-Helmholtz configuration and has a gradient of 12 G/cm along the symmetry axis. This traps about 10^9 atoms. The atoms from this MOT are transferred to the UHV MOT with the help of a transfer beam as mentioned before. The UHV MOT has the same beam parameters as the vapour cell MOT. However, the beams are not retro-reflected, instead, six counter propagating beams with almost the same intensity intersect at the glass cell at the quadrupole minimum to trap and cool the atoms.

The field gradient is produced in this case too, through quadrupole coils in anti-Helmholtz configuration and has a value of $10\,\mathrm{G/cm}$. This MOT traps about a few times 10^8 atoms at about $100\,\mu\mathrm{K}$. The repumper beam is overlapped with the z arm of the cooler beam in both the MOTs.

In contrast to the Rb MOT which has a large number of atoms, the Cs MOT in our case, is a single atom MOT. To load single or a few atoms, the Cs atoms are loaded directly into the UHV region having a very low Cs partial pressure. Apart from this, a very high field gradient of $300\,\mathrm{G/cm}$ is used in order to reduce the loading rate of the MOT as the loading rate is given by [108]

$$R_{\mathrm{L}} \propto \left(\frac{dB}{dz}\right)^{-14/3} . \tag{3.4}$$

Furthermore, MOT beams are narrow with a diameter of $\sim 2\,\mathrm{mm}$ and a total power of $\sim 1\,\mathrm{mW}$. The size of the MOT due to the high gradient is therefore $\sim 30\,\mu\mathrm{m}$ (largest size corresponding to a particular set of ground and excited state Zeeman levels [100]) in contrast to that of the Rb MOT where it is $\sim 8\,\mathrm{mm}$. Details of the single atom MOT are given in [54, 109]. The repumper beam and the cooler beam are coupled out at the experiment from the same fiber. The Cs MOT beams are overlapped with the Rb MOT beams in all the six directions. Since, the power balance of both the MOTs need to be adjusted independently in order to have an optimal optical molasses, species specific polarization optical elements are placed in the MOT beams, which change the polarization of one of the species without affecting the other and vice versa.

3.4 Coil System

The coil system is shown in figure 3.3. The main part of the coil system consists of the Quadrupole Ioffe Configuration (QUIC) trap [110] which is formed by the two quadrupole coils (MOT coils) and the Ioffe coil. Apart from this, a coil is placed along the gravitation axis from below, called the levitation coil in this thesis. Two coils in Helmholtz configuration are also placed along the axis of the MOT coils, just behind the MOT coils, which produce a homogeneous field. However, in this section, I will only discuss the QUIC trap. The other coils are not relevant for the preparation of a BEC in the magnetic trap. They will be discussed in the following chapter in the context of magnetic transport and state preparation of the atoms in the dipole trap.

The Rb atoms are cooled to quantum degeneracy in our experiment in the magnetic trap. An atom with a magnetic moment $\vec{\mu_{\mathrm{m}}}$ can be confined in an inhomogeneous magnetic field due to the interaction of this moment with the magnetic field. This

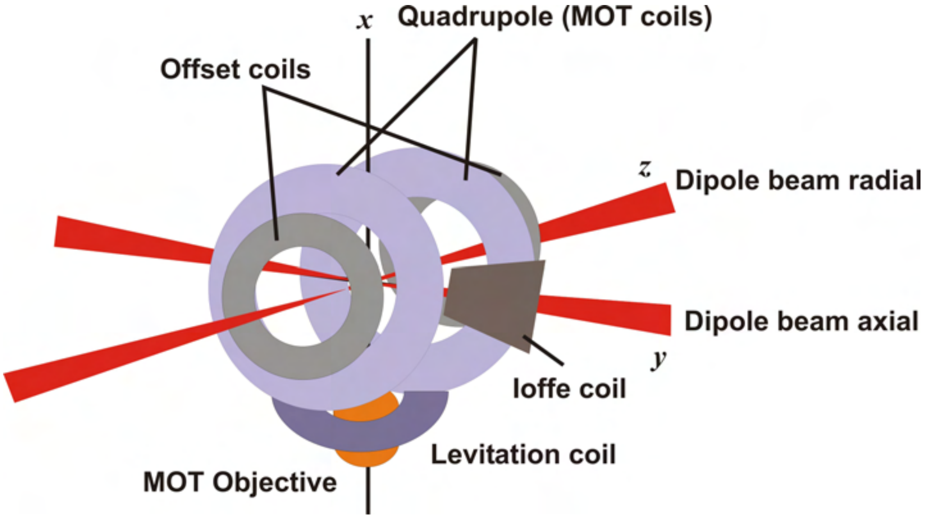

Figure 3.3: The QUIC configuration is shown with the two quadrupole coils along the z axis and the Ioffe coil along the y axis. The two coils parallel to the quadrupole coils (offset coils) are in Helmholtz configuration. The levitation coil is symmetric about the x-axis and surrounds the MOT objective. The dipole trap beams (red) are also shown. Note that the y axis is also referred to as the axial direction (symmetry axis of the Ioffe coil) and the z axis as the radial direction (symmetry axis of the quadrupole coil).

produces a force which is given by

$$\vec{F_{\mathrm{M}}} = \vec{\nabla}\left(\vec{\mu_{\mathrm{m}}} \cdot \vec{B}\right) = g_{\mathrm{f}}\mu_{\mathrm{B}}m_{\mathrm{f}}B \; , \tag{3.5}$$

where g_{f} is the Landé factor and m_{f} represents the Zeeman level of the hyperfine state f. Atoms are trapped only in the quantum states where the energy increases with increasing field. These are the weak field seeking states. This kind of a confinement can be provided by a quadrupole field, which has field zero at the trap centre with the field increasing in all the directions. This field is given by

$$B = A\sqrt{x^2 + y^2 + 4z^2} \; , \tag{3.6}$$

where A is the field gradient. Thus, the field is not uniform and has a stronger gradient along the symmetry axis of the quadrupole coils i.e. the radial direction. The velocities of the atoms should be low enough such that they follow the magnetic field adiabatically. The adiabaticity condition is given by

$$\omega_{\mathrm{Z}} \gg \frac{dB/dt}{B} \; , \tag{3.7}$$

where ω_{Z} is the Larmor frequency. However, this condition is not met close to the centre of the trap, where the magnetic field is very low i.e. close to zero. The atoms change their quantum state and are transferred to a non-trappable state. Hence, the atoms close to the trap centre are lost due to Majorana spin flips [111] and therefore this kind of a trap cannot be used to cool atoms to quantum degeneracy. However, an additional dipole field along the axial direction (symmetry axis of the coil producing the dipole field) can solve this problem. The sum of the quadrupole and the dipole field creates a harmonic trap having a finite value of the magnetic field at the trap centre, also called the offset field. The harmonic potential is given by

$$V\left(x,y,z\right)=\frac{1}{2}M\left({\omega_{\mathrm{rad}}}^{2}\left(x^{2}+z^{2}\right)+{\omega_{\mathrm{ax}}}^{2}y^{2}\right)+\mu_{\mathrm{m}}B_{0}\ , \tag{3.8}$$

where B_0 is the offset field, ω_{rad} and ω_{ax} are the radial and axial trap frequencies respectively and are given by

$$\omega_{\mathrm{rad}}=\frac{3}{2}A\sqrt{\frac{\mu_{\mathrm{m}}}{MB_{0}}}\ , \tag{3.9}$$

$$\omega_{\mathrm{ax}}=\frac{2}{6^{1/8}}\sqrt{\frac{\mu_{\mathrm{m}}A^{5/4}}{Mp_{\mathrm{m}}^{1/4}}}\ , \tag{3.10}$$

where A is the field gradient and p_{m} is the magnetic dipole moment of the dipole field.

In our experiment, the quadrupole field is generated by the MOT coils and the dipole field by the Ioffe coil. They are connected in series in order to minimize the noise generated by the power supply. The field minimum of the quadrupole and the QUIC traps are separated by a distance of 7 mm. A detailed description of the quadrupole and Ioffe coils is given in [52].

The atoms in the MOT go through a few stages before they are loaded into the magnetic trap in order to achieve high densities at low temperatures (increased phase space densities). For an optimal loading, mode matching needs to be achieved between the MOT and the magnetic trap such that they have comparable sizes and are well overlapped. The overlap is first achieved by adjusting the power balance of the MOT beams to move the MOT in space towards the centre of the magnetic trap before starting the experimental sequence. During the sequence, the atoms in the MOT are compressed by raising the magnetic field from 10 G/cm to 12 G/cm with a detuning of 22 MHz over a time period of 20 ms. The increase in the field gradient increases the density of the MOT and also reduces its size, thereby, giving a better overlap with the magnetic trap. The detuning is increased from that of the MOT stage to avoid radiation trap loss [112] because of a higher density. After this, the magnetic fields are switched OFF and the atoms are cooled by optical molasses. For this, the cooler light is further detuned to 27 MHz to have optimal sub-doppler cooling. The molasses has a duration of 8 ms. The atoms are cooled in the optical molasses to $\sim 50\,\mu$K. These atoms need to be pumped into the correct Zeeman level for magnetic trapping. This is achieved through optical pumping. In our case, the atoms are pumped to the $f = 2$, $m_f = 2$ i.e. the $|2,2\rangle$ state, which is the most tightly confining state. For this, circular polarized σ^+ light derived from the cooler light with a power of $150\,\mu$W is used to drive the $f = 2 \rightarrow f' = 2$ transition. This circular polarized light, in combination with the repumper light, with a power of $50\,\mu$W, pumps all the atoms which are distributed in all the ground state Zeeman levels, during the MOT phase to the $|2,2\rangle$ state by exciting the $\Delta m_\mathrm{f} = +1$ transitions. A homogeneous magnetic field produces the required quantization field which is 1 G in our case. The pumping is carried out for a duration of 2.25 ms. The atoms in the $|2,2\rangle$ state are no longer excited by the light as no $\Delta m_\mathrm{f} = +1$ transition is possible in this state.

Once the atoms are optically pumped to the $|2,2\rangle$ state, they are transferred to the quadrupole trap by switching on the magnetic field instantly with a field gradient of 72 G/cm. Here, they are adiabatically compressed in order to increase the phase space density by raising the field gradient to 200 G/cm in 1 s at a current of 16.9 A. This is followed by the transfer into the combined trap by raising the current through the Ioffe coil to 16.9 A, the so called QUIC trap. In our experiment, about 5×10^8 atoms are loaded into the QUIC trap at a temperature of $200\,\mu$K. The lifetime of these atoms is 120 s.

Once the atoms are in the QUIC trap, they undergo further cooling evaporatively to form a BEC. This is discussed in the next section.

3.5 Towards Quantum Degeneracy

The trapped atoms in the magnetic trap have densities of the order of $10^{11}\,\mathrm{cm}^{-3}$ and temperatures thousand times higher than that for a condensate or in other words, a phase space density 10^{-6} times lower. Further lowering of temperature by laser cooling is not possible at high densities due to radiation trapping and excited state collisions. In order to cool further, the evaporation cooling technique is employed. This is executed with the help of a microwave setup in our case. The same setup, in addition to a RF setup is, however, also used for the state preparation of the atoms in the dipole trap. In the following sections, the microwave set-up is discussed in detail. The evaporative cooling resulting in a Rb BEC is also discussed. The state preparation of the atoms is discussed in the next chapter.

3.5.1 Evaporative Cooling

Evaporative cooling is based on the principle of removal of atoms from a confined sample which have an energy higher than the average energy of the sample and the subsequent re-thermalization of the remaining sample to a lower temperature through elastic collisions [4, 113, 114]. The trap depth is reduced continuously to

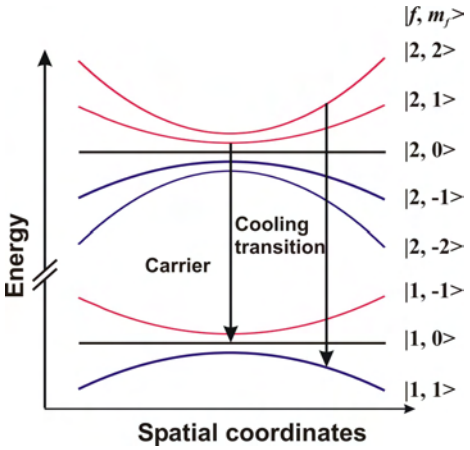

Figure 3.4: The Zeeman split hyperfine levels of the ground state of Rb are shown. Two microwave frequencies are shown inducing two transitions. The atoms in the $|2,2\rangle$ state are transferred to the anti-trapping $|1,1\rangle$ state by the first side band of the microwave (cooling transition). The microwave carrier frequency empties the $|2,1\rangle$ state continuously (see text).

achieve a continuous decrease in temperature, this is called forced evaporation. If the ramping is very fast (faster compared to the thermalization time scale), then the thermalization may not take place fully leading to less efficient evaporation. On the other hand, if it is very slow (compared to the lifetime of the atoms in the trap), atoms might be lost due to inelastic collisions as the atoms have a finite lifetime in the trap. Hence, a compromise should be found out between speed and efficiency. Since, the atoms need to re-thermalize fast enough (faster than their lifetime in the trap), a high density is a pre-requisite for a high rate of elastic collisions . In our case, we have densities of the order of $10^{12}\,\mathrm{cm}^{-3}$ with an evaporation time of about 20 s compared to a lifetime of 120 s for the atoms (see details below). The efficiency and speed of evaporation is therefore improved by strong confinement. A tighter confinement in a harmonic trap is given by higher trap frequencies. The trap frequencies in the QUIC trap, in our case, have been calculated using equations (3.9) and (3.10) and are given by $\omega_{\mathrm{rad}} = 2\pi \times 180\,\mathrm{Hz}$ and $\omega_{\mathrm{ax}} = 2\pi \times 18\,\mathrm{Hz}$. In this thesis, atoms have been evaporatively cooled both in the magnetic as well as the optical dipole trap. Here, evaporative cooling in the QUIC trap is discussed. The evaporative cooling in the dipole trap is discussed in section 4.2.

The Zeeman split hyperfine levels of ^{87}Rb are shown in figure 3.4. The atoms are confined in the $|2,2\rangle$ state. To cool the atoms by evaporation, the trap depth has to be lowered, or in other words, the high energy atoms need to be expelled from the trap, so that the remaining atoms can re-thermalize to a lower temperature. This is achieved by using a microwave frequency which is resonant to the $|2,2\rangle \rightarrow |1,1\rangle$ atomic transition. The $|1,1\rangle$ state is a high field seeking state and therefore,

]

the atoms are no longer confined in the magnetic trap. The trap depth has to be lowered continuously by ramping the microwave frequency until degeneracy is observed. However, in our case, a Stern Gerlach experiment showed the presence of atoms in the $|2,1\rangle$ state also. Inelastic collisions between the two clouds prevented further cooling at about $1\,\mu$K and therefore, the condensation of Rb atoms. This problem was solved by using another microwave frequency resonant to the $|2,1\rangle \rightarrow |1,0\rangle$ atomic transition at the trap centre. This state was therefore, continuously emptied, thereby preventing collisions with the atoms in the $|2,2\rangle$ state resulting in the condensation of Rb. The microwave setup responsible for generating the above frequencies is discussed below.

3.5.2 Microwave Setup

The schematic of the microwave setup is shown in figure 3.5. The ground state hyperfine splitting of ^{87}Rb is 6.8 GHz. This frequency is generated with a PLDRO (MITEQ) which multiplies the signal from the Rhode and Schwarz (R&S) signal generator by 683. From now on, this will be referred to as R&S1. The R&S1 generator is operated in the list mode which allows it to produce a list of frequencies each for a finite time. In our case, this is operated on two frequencies, one of which is used for evaporation and the other for the pulse generation for state preparation (see chapter 4). The frequency used for evaporation is 10.00807 MHz which gives a frequency of 6.83551 GHz at the output of the PLDRO. This particular frequency is chosen, as it is resonant to the $|2,1\rangle \rightarrow |1,0\rangle$ atomic transition at the trap centre in our case and is therefore used to empty the $|2,1\rangle$ state. This is then mixed with a radio frequency, generated by another signal generator (TABOR) as shown in the figure which produces frequencies between 1-50 MHz, with a mixer. The mixer output therefore, consists of a carrier frequency and side bands. The first side band is used for cooling.

The old setup consisting of a Marconi signal generator for producing the 10.00807 MHz frequency and an Agilent for the RF frequencies was replaced by the present setup for frequency generation. In the old setup, the microwave side band used for cooling had a broad spectral width of 30 kHz with a resolution worse than 10 kHz. In contrast to this, the new setup generates a side band which has a background spectral width of 20 kHz and a peak with a width of 2.5 Hz. The background is suppressed by 40 dB with respect to the peak. As the condensate has a depth of a few kHz to a few hundred Hz, the old set-up could not generate stable BECs due to the broad spectral width of the side band and the poor resolution of the generator. In the new setup, the frequency can be changed with a resolution of 1 kHz to obtain stable BECs. The side band used for cooling with the new setup is shown in figure 3.6.

A RF switch with an attenuation of 60 dB is used to switch between the TABOR and a second R&S generator. From now on, this will be referred to as R&S2. This

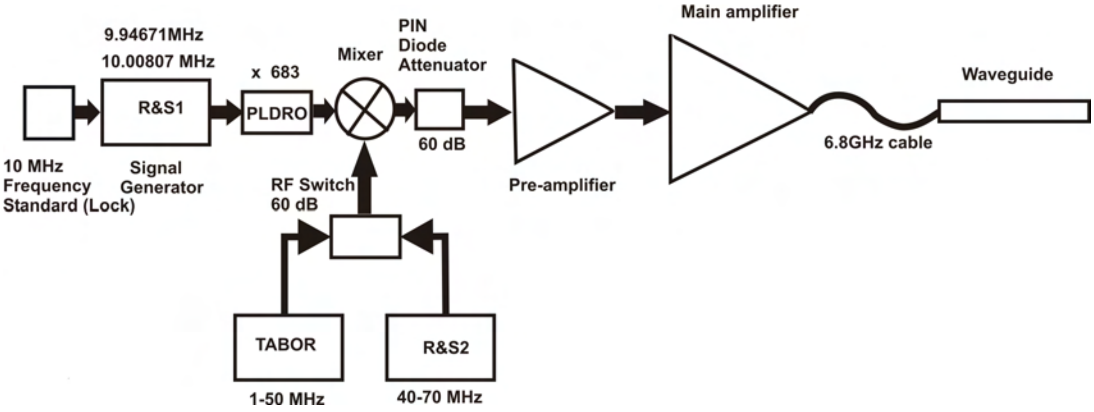

Figure 3.5: The components of the microwave setup are shown. The PLDRO multiplies the frequency from the R&S1 generator by 683. This is then mixed with the frequency from either the TABOR or the R&S2 generator. The RF switch allows the switching between the TABOR and the R&S2 generators. The signal then passes through a PIN diode attenuator and two amplifiers to be finally transmitted by a waveguide.

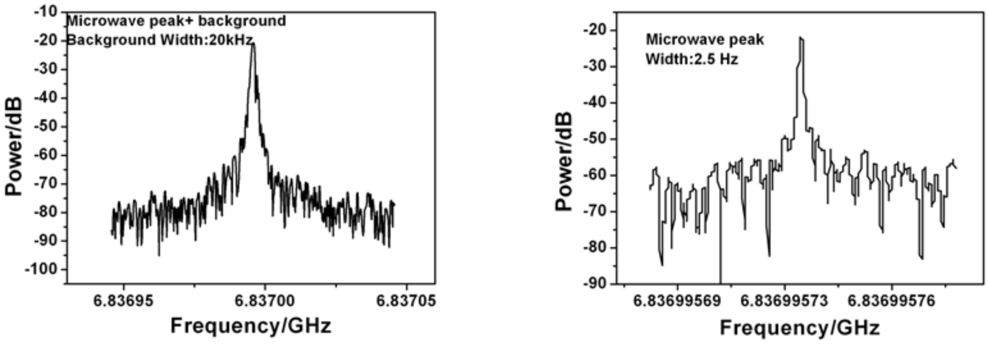

Figure 3.6: The two graphs show the microwave side band used for cooling measured using a spectrum analyser. The left picture shows the peak along with the background which is suppressed by 40 dB with respect to the peak. The background has a width of 20 kHz. The width of the peak is not resolved properly in this picture. The graph on the right shows the well resolved peak which has a width of 2.5 Hz.

generator produces frequencies between 40-70 MHz and is used for pulse generation along with the R&S1 generator for state preparation. The output of the mixer passes through a PIN diode attenuator (max. attenuation 60 dB), which allows the adjustment of power of the microwave signal during the experimental run depending upon the analog input voltage provided (0-10 V). This is then passed through a pre-amplifier and the main amplifier and transmitted through a microwave antenna (waveguide) to the atoms. The amplifier is connected to the waveguide by a low

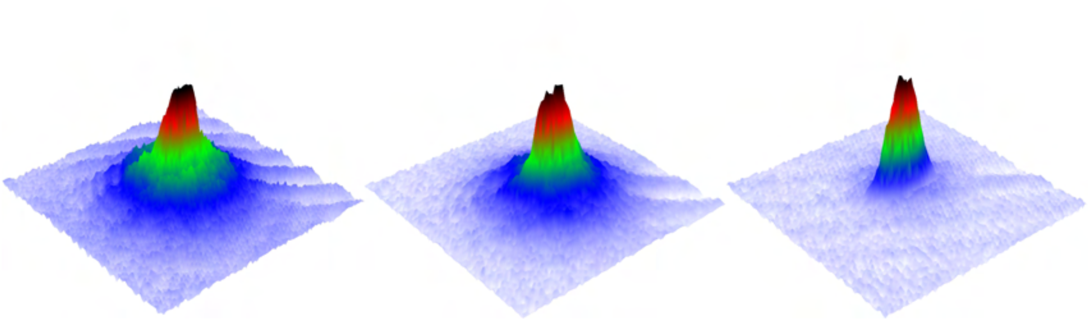

Figure 3.7: A 3D picture of the evolution of a BEC from a thermal cloud is shown. The leftmost picture depicts a partial condensate with a large fraction of thermal atoms, the next one to the right has a higher fraction of the condensate, the rightmost picture depicts a pure condensate.

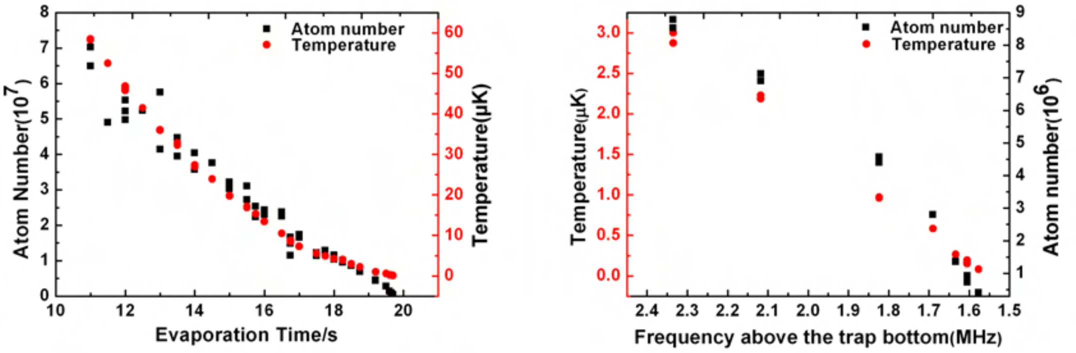

Figure 3.8: The graph on the left shows the atom number and temperature progression with respect to the evaporation time during the last 10 s of the evaporation. Both the temperature and atom number decrease as evaporation progresses. The graph on the right shows the temperature and atom number progression with respect to the frequency above the bottom of the trap during the last second of evaporation. The temperature decreases from 3 μK to 300 nK and the atom number decreases by more than an order of magnitude from $10^7 - 5 \times 10^5$ atoms during this period.

loss 6.8 GHz cable having a length of 0.5 m. The maximum power at the output of the amplifier is 8 W. The entire setup is locked to the 10 MHz frequency standard. All the coaxial components are placed on a bread board which is water cooled, the main amplifier has an additional ventilator for cooling. This setup is trigerred from a pulse generator (Quantum Composer, 9520 Series), which in turn is trigerred from the experiment.

Rb BEC

With the above setup and procedure, a Rb BEC is achieved with about 4×10^5 atoms in the condensate. A picture of the Rb BEC is shown in the figure 3.7. Stable BECs could be produced due to the improvement in the resolution of the microwave frequency and also due to the thermalization of the magnetic coils. The floor of the magnetic trap drifts due to thermal effects (temperature changes). These small drifts (few hundred nanokelvin to few microkelvin) are not important for a thermal cloud but is significant in the case of a BEC. Thermalization is attained in about 30 minutes by an automatic repetition of the experimental run which lasts about a minute each. The temperature and atom number progression towards a BEC for the evaporation ramp used in our experiment is shown in figure 3.8. The evaporation takes about 20 s.

3.6 Imaging and Detection Techniques for Rb and Cs

The cold and dense Rb atoms in our experiment are imaged through the typical absorption imaging technique [114] which gives the atom number, temperature and the density of the cloud. Due to the very small number of Cs atoms involved in our experiment, they cannot be imaged via absorption imaging technique and therefore, the fluorescence detection technique is employed in this case. Both are discussed below.

3.6.1 Absorption Imaging

When atoms are irradiated with near resonant light, they absorb the light photons casting a shadow which is then imaged onto a Charge Coupled Device (CCD) camera. This is the so called absorption imaging technique. The image reflects the density distribution of the atoms at the time of imaging. The temperature and atom number for the atomic clouds is determined by the Time of Flight (TOF) method. For this, the magnetic fields are switched OFF and the cloud falls and expands under gravity. The free expansion of the cloud is imaged which gives the velocity of the cloud and in turn determines the temperature. Typically, three images are taken, one with atoms, one without atoms which images only the imaging beam and the third one without either of them which projects the background noise. The probe light is attenuated when it passes through the atoms, the attenuation is given by the Lambert Beer law which is

$$PA\left(x,y\right) = P\left(x,y\right) e^{-D_{\mathrm{A}}(x,y)} \,, \tag{3.11}$$

where $PA\left(x,y\right)$ is the imaging beam profile with atoms, $P\left(x,y\right)$ is the imaging beam profile without atoms and $D_{\mathrm{A}}\left(x,y\right)$ gives the attenuation. The images with

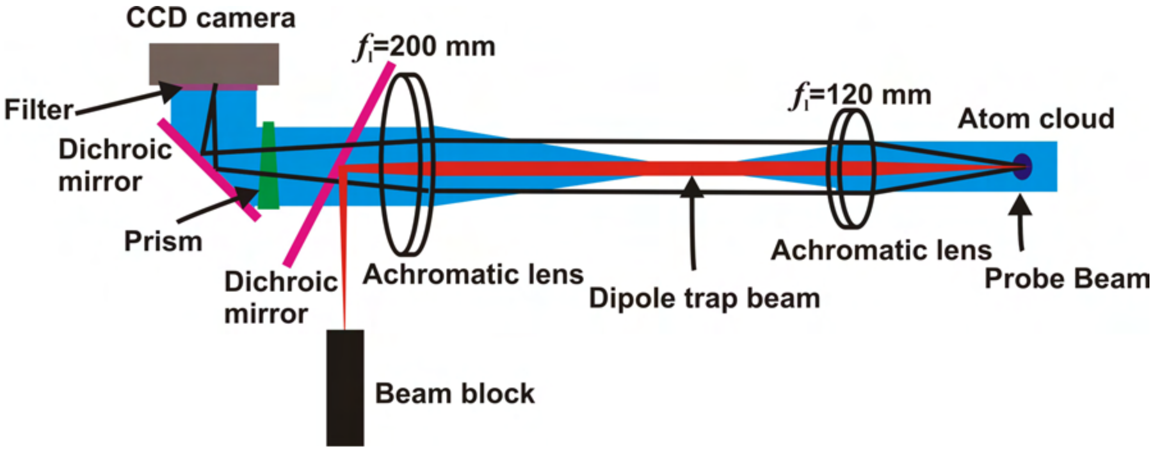

Figure 3.9: The absorption imaging setup: The atom cloud (violet) is irradiated by the probe beam (blue) and then imaged onto the CCD camera. The achromatic lenses give a magnification of 1.67 and the two dichroic mirrors separate the probe beam from the dipole trap beam (red) and the Cs beam respectively. The prism (green) shifts the probe beam in order to observe the atoms in the QUIC trap. The filter (purple) filters out any remaining dipole trap power transmitted by the dichroic mirror.

$(I_{PA}(x,y))$ and without $(I_P(x,y))$ atoms can be written as

$$I_{PA}(x,y) = PA(x,y) + N_{\mathrm{A}}(x,y) \ , \tag{3.12}$$

$$I_P(x,y) = P(x,y) + N_{\mathrm{A}}(x,y) \ , \tag{3.13}$$

where $N_{\mathrm{A}}(x,y)$ is the contribution from the background noise. The ratio of the above two equations gives the attenuation $D_{\mathrm{A}}(x,y)$, which is proportional to the column density of the atomic cloud. This, further gives all the required parameters necessary for analyzing the atomic cloud.

The absorption imaging system used in our experiment is shown in figure 3.9. The imaging beam which is coupled out from an optical fiber and having a beam diameter of 2 mm is magnified to a 1.5 cm collimated beam using two lenses (not shown in the figure) and passed through the glass cell where the atoms are present. This beam after illuminating the atoms is incident on an achromatic lens having a focal length $f_l = 120\,\mathrm{mm}$, which focusses the light, which is then collimated using a $f_l = 200\,\mathrm{mm}$ achromatic lens, thereby giving a magnification of 1.67. This means, that the fluorescence from the atoms (object) is collected and collimated by the first lens and then focussed by the second lens onto the camera to form the image.

To obtain a sharply focussed image, the atoms should sit in the focus of the first lens and the camera in the focus of the second lens. If the atoms sit out of focus, then the image obtained will have regions of negative optical density. A detuning of the imaging beam to the red or blue will produce either a doughnut shape or a ring shape cloud depending upon the position of the object in the focal plane. This is discussed in detail in [115]. This method was employed in our case, with a BEC, to obtain a sharply focussed image on the camera by first moving the camera with respect to the second lens and then finely adjusted by moving the second lens with the help of a linear translation stage.

A two inch dichroic mirror is placed behind the second lens which reflects the 1064 nm dipole laser beam which is also present along this axis onto a beam block and transmits the 780 nm and the 852 nm imaging beams. This is done to avoid the dipole laser beam entering the camera. A prism is placed behind this mirror which is used to switch the imaging between the atoms in the quadrupole trap and the QUIC trap which are separated by 7 mm. The prism which has an angle of 4° is therefore placed at a distance of 10 cm from the camera to achieve a beam displacement of 7 mm. It is mounted on a flip mount such that it is placed in the beam path only when the displacement is required to image the atoms in the QUIC trap. This is followed by a dichroic mirror which is used to separate the Rb and Cs wavelengths. The Rb imaging beam is reflected onto the CCD camera whereas the Cs beam is transmitted. An interference filter is placed in front of the CCD camera which allows the Rb light to pass through and blocks any residual dipole light. In this thesis, since Cs is detected through the fluorescence detection technique, an imaging beam is not required but for further experiments for Cs in a conservative species selective trap which has been built already, the imaging of Cs will also be done with a Electron Multiplying Charge Coupled Device (EMCCD) camera (Company:Andor) placed in the transmission axis of the dichroic mirror. The camera used for imaging Rb (Company:Apogee), has a pixel size of $9\,\mu$m with 768×512 pixels. The image is taken with an exposure time of $200\,\mu$s. Apart from this imaging beam in the radial direction (symmetry axis of the quadrupole coils), an imaging beam in the axial direction (symmetry axis of the Ioffe coil) is also used to illuminate the atoms. This is imaged onto a camera (Company:Imaging Source) having a pixel size of $5.6\,\mu$m with 640×480 pixels. Therefore, the simultaneous imaging of the atoms in all the three directions is possible using both the cameras.

3.6.2 Fluorescence Detection

The Cs atoms in our case are not imaged but are detected by counting the number of scattered photons. This method is used here as absorption imaging does not have the resolution to image small number of atoms. Only a small fraction of the light scattered by the atoms is collected by the imaging system. The fluorescence collected depends on the numerical aperture of the objective that collects light and is given by [116, 117]

$$\frac{\Omega_{\mathrm{s}}}{4\pi} = \frac{1}{2}\left(1 - \sqrt{1 - (NA)^2}\right) , \tag{3.14}$$

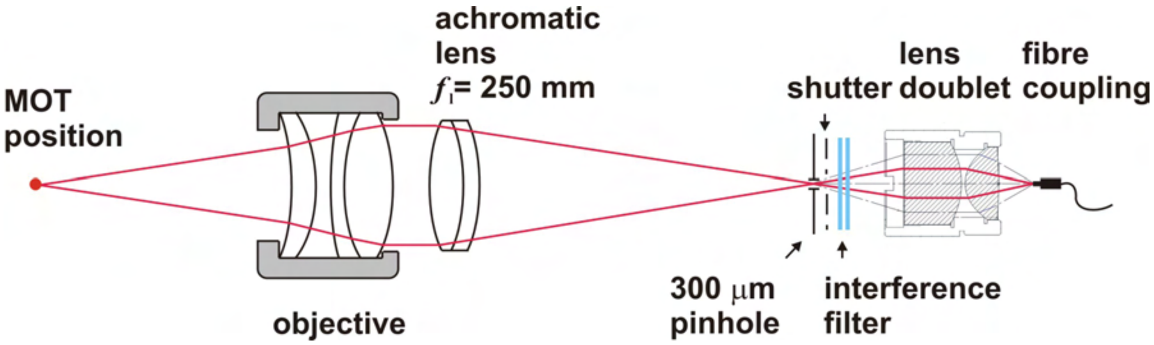

Figure 3.10: The fluorescence detection setup: The objective collects and collimates the MOT fluorescence. This is then focussed onto the pinhole having a size of 300 μm by the achromatic lens ($f_l = 250$ mm) and passes through a shutter and two interference filters (blue). The fluorescence is then collected and focussed onto the fiber coupler by the lens doublet.

where Ω_s is the solid angle covered by the objective and NA is the numerical aperture of the objective. Since, in our case, we detect single Cs atoms where the light scattered per atom is of the order of a few picowatt, the NA of the objective becomes even more critical. At such small powers, stray light suppression also becomes very important.

Figure 3.10 shows a schematic of the fluorescence detection setup used in our experiment. The objective is placed below the glass cell in our case since there is no other light other than the Rb transfer beam along this axis. Also, the reflections from the inner side of the glass cell are far away enough from the MOT, in this direction, such that they can be prevented from entering the detector through spatial filtering. The objective has a numerical aperture of 0.29 such that 2.1% of the total fluorescence is collected. As shown in the figure, the light from the MOT is collected by the objective and then collimated. This collimated light is focussed by an achromatic lens having $f_l = 250$ mm onto a 300 μm pinhole, which serves as a spatial filter to prevent stray light entering the detector. This is then collected by a lens doublet and focussed onto a fiber which couples this light to the Single Photon Counting Module (SPCM). The SPCM counts the number of photons and therefore, detects the number of Cs atoms present. Two band pass interference filters are placed in front of the fiber coupler which provides spectral filtering, with a transmission of 93% at 852 nm. Thus, light at 780 nm (transfer beam), is suppressed by 10^{14} and light at 1064 nm is suppressed by 10^{6}, although this light is not present along the axis of the objective and therefore should not pose a problem. A shutter is also placed behind the pinhole, this serves as a mechanical obstruction to the fluorescence light and is controlled by the experimental sequence. All the optical elements are placed in a closed cage system to avoid stray light. A detailed analysis of the objective used along with details of alignment and incorporation into the experiment is given in

[109].

3.7 Optical Dipole Trap

Till now I have discussed the trapping and cooling of atoms in a magnetic trap. They are conservative traps with large trap depths of the order of 100 mK and are ideal for condensation experiments. However, if the magnetic field needs to be used for manipulating the interaction between the species, for example in the case of Feshbach resonances, then the field strength has to be available as a free parameter. This is difficult when such strong fields are used for trapping. Moreover, magnetic trapping does not allow confinement of atoms in all its magnetic sub-states, confinement is only allowed in the weak field seeking states. This limits the number of states available for experiments. Especially in our particular case (for all future experiments concerning Rb and Cs in a conservative potential), the states of interest, the absolute ground state of Rb and Cs, viz. the $|1,1\rangle$ and the $|3,3\rangle$ states respectively, are anti-trapping states. Optical traps [118, 119, 15, 16] offer a good substitute to the magnetic traps, where all the sub-states can be occupied and the magnetic field can also be used as a free parameter to tune the interactions. They are also called dipole traps because the force involved in trapping is the dipole force. These traps are however, shallow traps when compared to the magnetic traps, but have been realized due to the laser cooling mechanisms which pre-cool the atoms such that they can be efficiently loaded into the dipole trap.

Dipole force arises due to the dispersive interaction of the electric dipole moments of the atoms with the light field. Atoms however, do not have permanent electric dipole moments, the oscillating electric field of the laser light induces an electric dipole moment which interacts with the light field. The energy levels of the atoms are shifted, which is the so called AC Stark shift or the light shift due to this interaction. If the electric field of the laser is spatially inhomogeneous, then this light shift varies in space and gives rise to a potential, the gradient of which produces the dipole force. The interaction of the laser light with atoms also leads to scattering of photons of the trapping light and therefore, sets a limit to the trap performance. For far detuned light, however, the optical excitation is very low and therefore, the radiation force associated with the scattering of photons is negligible when compared to the dipole force. Considering a two level atom, the atom-light interaction is given by [120]

$$p_{\mathrm{I}} = \alpha_{\mathrm{P}} W \ , \tag{3.15}$$

where p_{I} is the induced dipole moment, W is the electric field of the laser light and α_{P} is the complex polarizability with real and imaginary terms. The interaction potential is then, given by

$$U = -\frac{1}{2}\langle p_{\mathrm{I}} W\rangle = -\frac{1}{2\epsilon_0 c}\mathrm{Re}\left(\alpha_{\mathrm{P}}\right) I_0 \ , \tag{3.16}$$

where the factor 1/2 is due to the induced dipole moment and I_0 is the intensity of the laser field [2]. Due to the conservative nature of the dipole force, it is then given by the gradient of this potential

$$F_{\mathrm{D}} = -\nabla U(r) = \frac{1}{2\epsilon_0 c}\mathrm{Re}\left(\alpha_{\mathrm{P}}\right)\nabla I_0(r) \ . \tag{3.17}$$

As mentioned before, the atoms scatter photons of the trapping light which can be expressed in terms of the absorption of this light by atoms, the scattering rate is given by

$$\Gamma_{\mathrm{sc}} = \frac{P_{\mathrm{abs}}}{\hbar\omega_{\mathrm{t}}} = \frac{\langle \dot{p}_{\mathrm{I}} W\rangle}{\hbar\omega_{\mathrm{t}}} = \frac{1}{\hbar\epsilon_0 c}\mathrm{Im}\left(\alpha_{\mathrm{P}}\right) I_0(r) \ . \tag{3.18}$$

The interaction potential and the scattering rate are the two main quantities which define the dipole trap parameters. The expressions for these two quantities can be written by calculating the atomic polarizability. The polarizability of the atoms can be calculated according to the semiclassical approach and is given by

$$\alpha_{\mathrm{P}} = 6\pi\epsilon_0 c^3 \frac{\Gamma/{\omega_{\mathrm{t}}}^2}{{\omega_{\mathrm{t}}}^2 - {\omega_{\mathrm{f}}}^2 - i\left({\omega_{\mathrm{f}}}^3/{\omega_{\mathrm{t}}}^2\right)\Gamma} \ , \tag{3.19}$$

where ω_{t} is the resonance frequency of the atomic transition, ω_{f} is the driving frequency (frequency of the dipole trap radiation) and Γ is the decay rate of the excited state which is given in the semiclassical approach by

$$\Gamma = \frac{{\omega_{\mathrm{t}}}^3}{3\pi\epsilon_0\hbar c^3} \mid \langle e \mid \mu_{\mathrm{d}} \mid g\rangle \mid^2 . \tag{3.20}$$

Using the above two expressions, the interaction potential and the scattering rate can be written in Rotating Wave Approximation (RWA) case as,

$$U = \frac{3\pi c^2}{2{\omega_{\mathrm{t}}}^3}\frac{\Gamma}{\Delta} I_0(r) \ , \tag{3.21}$$

$$\Gamma_{\mathrm{sc}} = \frac{3\pi c^2}{2\hbar{\omega_{\mathrm{t}}}^3}\left(\frac{\Gamma}{\Delta}\right)^2 I_0(r) \ , \tag{3.22}$$

where $\Delta = \omega_{\mathrm{f}} - \omega_{\mathrm{t}}$ represents the detuning with respect to the atomic transition frequency. This value of the dipole potential corresponds to the light shift of the atoms in the ground and excited states. They are shifted by the same amount in opposite directions. For red detuned light, $\Delta < 0$, which means that $U < 0$ or in other words, the potential is an attractive potential. The atoms are attracted to the intensity maximum. For blue detuned light, $\Delta > 0$, the potential minimum corresponds to intensity minimum. Since, $U \propto I_0/\Delta$ and $\Gamma_{\mathrm{sc}} \propto I_0/\Delta^2$, the optimum

---

[2] Here, I_0 has been used for intensity instead of the conventional symbol I to differentiate it from the nuclear spin quantum number $\vec{I}$ introduced in chapter 1

conditions for trapping are achieved for large intensities and large detunings resulting in a higher U and a lower Γ_{sc}.

However, alkali atoms are multilevel atoms and therefore, the state dependent polarizability has to be taken into account. The light shift and therefore, the dipole potential depends on the particular state of the atom. It is influenced by the electronic and nuclear angular momenta and the polarization of the light field. For circular polarization, the shift depends on the m_f states whereas for linear polarization, the shift is independent of the m_f states and is the same as for the two-level atom. This is however possible only for large detunings, detunings larger than the excited state hyperfine splitting. Therefore, linear polarized light is usually employed in optical traps for alkali elements.

The three most commonly used kinds of dipole traps for the red detuned laser light are viz. focussed beam trap, standing wave trap and the crossed beam dipole trap. The focussed beam trap consists of a single Gaussian beam. The spatial intensity distribution along the propagation axis of such a beam with a power P is given by

$$I_{\mathrm{FB}}\left(r,z\right) = \frac{2P}{\pi w_{\mathrm{b}}^{2}\left(z\right)} e^{\left(\frac{-2r^{2}}{w_{\mathrm{b}}^{2}(z)}\right)} , \tag{3.23}$$

where $w_{\mathrm{b}}\left(z\right)$ is the $1/e^{2}$ radius of the beam at a distance z and is given by

$$w_{\mathrm{b}}\left(z\right) = w_{0}\sqrt{1+\frac{z}{z_{R}}^{2}} , \tag{3.24}$$

where w_0 is the Gaussian beam waist and z_R is the Rayleigh length. The dipole potential can be written using this intensity distribution, since $U \propto I$. In such a trap, the potential is steeper in the radial direction (perpendicular to the direction of propagation of the beam) than in the axial direction (along the direction of propagation of the beam) and the trapping volume is also different because it depends on the beam waist in the radial direction and on the rayleigh length in the axial direction. The radial (ω_{rad}) and axial (ω_{ax}) trap frequencies are given by

$$\omega_{\mathrm{rad}} = \left(\frac{4U}{M{w_{0}}^{2}}\right)^{1/2} , \tag{3.25}$$

$$\omega_{\mathrm{ax}} = \left(\frac{2U}{M{z_{\mathrm{R}}}^{2}}\right)^{1/2} . \tag{3.26}$$

To avoid this anisotropic nature of the trap, another beam orthogonal to the original beam is used, the intersection of the two results in a trap called the crossed beam dipole trap. This provides a larger trapping volume and a tighter confinement in three dimensions. The trap used in our experiment is a crossed beam dipole trap.

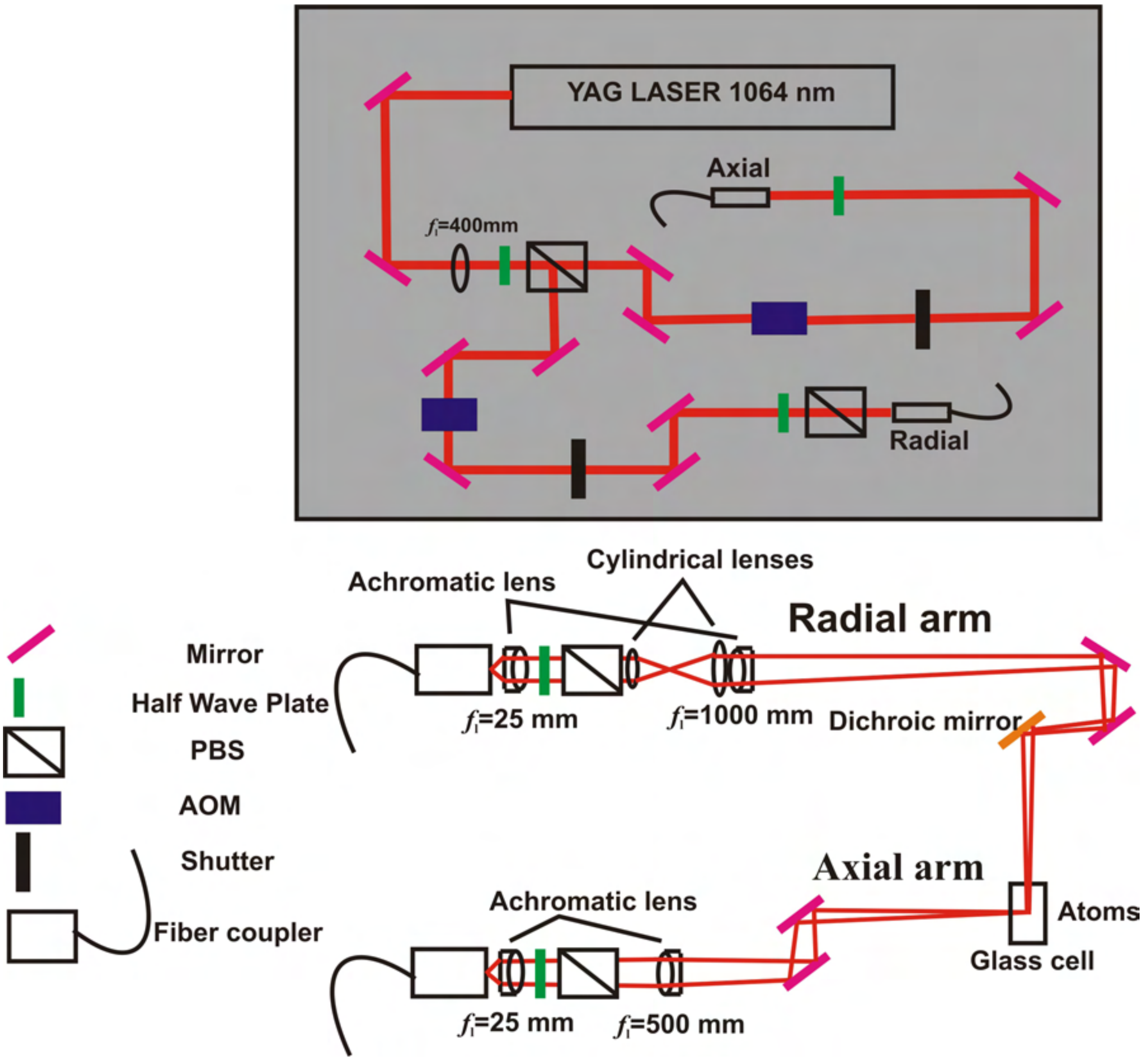

Figure 3.11: Dipole Trap setup: The figure in the box represents the setup of the dipole trap before it is coupled into the fibers. The beam from the YAG laser is split into two for the two axes (radial and axial respectively). Both the beams pass through an AOM each, before being coupled into the fiber. The lower picture depicts the focussing of the radial and axial beams onto the position of the atoms (glass cell) using the achromatic lenses. The radial arm has additional cylindrical lenses which creates an elliptical trap. The light from the radial arm is reflected by a dichroic mirror (orange) onto the glass cell.

Experimental Realization

The dipole trap in our experiment is realized by an arc pumped YAG laser (Quantronix Model 116EF-OCW-10) at 1064 nm with a maximum output power of 10 W. The setup is shown in figure 3.11. The laser light is divided into two beams, one for each arm of the dipole trap, viz. the radial and axial directions by a half wave plate and a PBS cube. The power of the dipole trap needs to be varied during the ramping up of the dipole trap as well as for the evaporation ramp and also for the switching OFF of the dipole trap. In order to do this, an AOM is placed in the beam which can change the power output by amplitude modulation. The required waveform is transmitted to the AOM from the computer via waveform generators. An AOM in single pass configuration at a central frequency of 80 MHz is therefore, placed in each arm, one of which amplifies the +1 order order whereas the other amplifies the -1 order. This is done to avoid interference effects at the position of the atoms (crossing point of the two beams). The AOMs have an efficiency of $\sim 90\%$. A shutter is also placed in each arm to get rid of any residual light from the AOM once it is switched OFF. These shutters do not need to be fast as the switching of the dipole trap is achieved through the AOM, they however, should be able to tolerate the high power of the YAG laser beam. The light is then coupled into optical fibers to be coupled out at the experiment. In the axial arm, a $\lambda/2$ plate is placed in front of the fiber. The fibers used here are polarization maintaining fibers and it is important to orient the polarization either along the fast axis or the slow axis of the fiber to avoid polarization fluctuations at the output of the fiber. Polarization fluctuations can result in intensity fluctuations of the trap beam and therefore, result in heating or trap loss. Therefore, the $\lambda/2$ plate is used to rotate the polarization such that it is oriented along the slow or fast axis of the fiber. In the radial arm however, a PBS cube (extinction ratio 1000:1) is also placed along with the $\lambda/2$ plate for a purer polarization. Intensity fluctuations can also be caused due to changes in the fiber coupling. To avoid these fluctuations, a feedback is sent to the AOM through a power stabilization circuit, thereby maintaining the dipole trap beams at a constant power for a particular value of the AOM voltage. This is discussed in detail in [54].

The light coupled out at the experiment is first collimated by an achromatic lens ($f_1 = 25\,\mathrm{mm}$) to a $1/e^2$ radius of 1.9 mm. A $\lambda/2$ plate and a PBS (Melles Griot; extinction ratio, 1000:1) cube are used for further polarizing the laser beams. In the axial arm, an achromatic lens of focal length 500 mm is used to focus the beam to a waist of 86 μm at the quadrupole minimum. In the radial arm, the achromatic lens used has a focal length of 1000 mm and therefore, focusses the beam to a waist of 172 μm. This is done to have a larger trap volume due to the spatial extent of the atomic cloud along the Ioffe axis. However, in the gravitational axis, the extension of the cloud is already restricted by the axial beam and therefore, a higher trap volume is not required. To compensate for the larger volume in this direction created by the achromatic lens, two cylindrical lenses, with focal lengths 30 mm and 60 mm respectively are used. These lenses are placed before the achromatic lens and expand the beam diameter along the gravitational axis by a factor of 2 (ratio between the two focal lengths). Since a higher beam diameter leads to a tighter focus, the achromatic lens focusses this asymmetric beam such that the beam waist along the gravitation axis is 86 μm. A dichroic mirror (T:780 nm and 852 nm; R:1064 nm) reflects the radial

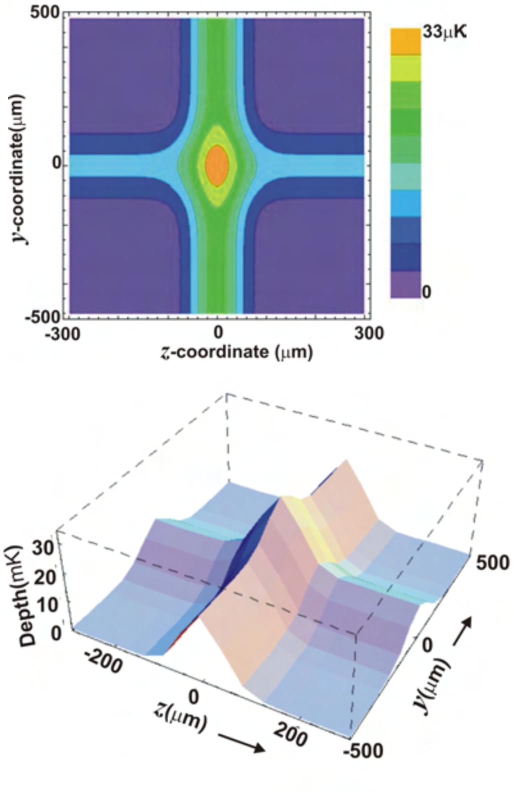

Figure 3.12: The upper figure shows a contour plot of the crossed dipole trap. The lighter regions correspond to a higher density. The horizontal axis represents the imaging axis and the vertical axis corresponds to the Ioffe coil axis. The trap is elliptical is shape. The lower figure is a 3D plot of the trap depth. The axis shown are the imaging (z) and the Ioffe (y) axis. The trap has a maximum depth of $k_B \cdot 33\,\mu$K. As is clear from the figure, the trap depth decreases at a distance equal to the beam waist from the centre of either beams.

trap beam onto the glass cell, this is used because of the presence of the MOT beams and the imaging beams along the same axis.

Trap Parameters

The trap depth, trap frequencies and the scattering rate are the parameters which characterize the trap. The trap depth decides the temperature of the cloud that can be stored in the trap. The trap frequencies are a measure of the confinement of the trap, which in turn is a measure of the cloud density as well as the temperature. The scattering rate determines the heating of the cloud and an eventual trap loss due to scattering of photons of the confining light field by the atoms. For the crossed dipole trap, the trap depth was calculated using equation (3.21) which gives

$$U = k_{\mathrm{B}} \cdot 33\,\mu\mathrm{K}\ , \tag{3.27}$$

However, along the axial direction for both the beams, the trap depth decreases at half the beam waist leading to loss of atoms. Hence, the effective trap depth is given by

$$U_{\mathrm{eff}} = U/2 = k_{\mathrm{B}} \cdot 16.5\,\mu\mathrm{K}\ , \tag{3.28}$$

The scattering rate is calculated using equation (3.22) and is given by

$$\Gamma_{\mathrm{sc}} = 0.26\,\mathrm{Hz}\,. \tag{3.29}$$

The trap frequencies were calculated using equations (3.25) and (3.26) and are given by

$$\omega_x = 2\pi \times 209\,\mathrm{Hz}\ , \tag{3.30}$$

$$\omega_y = 2\pi \times 74\,\mathrm{Hz}\ , \tag{3.31}$$

$$\omega_z = 2\pi \times 148\,\mathrm{Hz}\ , \tag{3.32}$$

where ω_x, ω_y and ω_z are the trap frequencies in the gravitation axis, the Ioffe axis and the imaging axis respectively. All the parameters have been calculated for a power of 2 W in each arm of the dipole trap and for the beam waists already mentioned before. A contour plot of the crossed dipole trap and a three dimensional plot of the trap is shown figure 3.12.

The loading of the dipole trap in our case, is from the magnetic trap and not from the MOT as is done typically. The loading together with the transport of the cold cloud will be discussed in the next chapter.

4 State Preparation of the Rb BEC in the Dipole Trap

In the previous chapter, I discussed the preparation of a Rb BEC in a magnetic trap with about a few hundred thousand atoms in the condensate. However, as already mentioned in section 3.7, there are certain advantages of using a dipole trap over a magnetic trap which includes the possibility of trapping atoms in the anti-trapping and untrapped states and the use of the magnetic field as a free parameter for tuning the interactions between the atoms, like for example in the case of magnetic Feshbach resonances [17, 18, 53, 121, 122]. In our specific case, we need to prepare the Rb atoms in the $m_f = 0$ state because it not sensitive to magnetic fields and therefore, not affected by the high gradient (300 G/cm) of the Cs MOT during the interaction. In this thesis, the interactions between an ultracold Rb gas and a Cs MOT are investigated. This is the first step towards future experiments involving a Rb BEC and a single Cs atom in species specific conservative optical traps where both the species would be stored in their absolute ground states. Therefore, as a pre-requisite the Rb BEC is prepared in an optical dipole trap in the desired state.

In this chapter, I will discuss the route towards the preparation of the Rb BEC in the $|1,1\rangle$ (the absolute ground state) and the $|1,0\rangle$ state and the overlapping of the Rb cloud with the Cs MOT. In section 4.1, the magnetic transport of a cold Rb cloud towards the position of the Cs MOT is discussed. Section 4.2 deals with evaporative cooling in the $|2,2\rangle$ state in a crossed dipole trap leading to the condensation of Rb. In section 4.3, I discuss the transfer of the BEC from the $|2,2\rangle$ to the $|1,1\rangle$ state using a microwave radiation and a consequent calibration of the coils used through microwave spectroscopy. Finally, the last section deals with the preparation of the BEC in the state we are interested in, i.e. the $m_f = 0$ state. Two different methods are discussed here for this purpose.

4.1 Magnetic Transport of a Cold Cloud in Conjunction with the Dipole Trap

It has already been shown that the Rb atoms are trapped and evaporatively cooled in a QUIC trap to quantum degeneracy. In order to perform experiments related to the interactions of a Rb BEC with a Cs MOT we need to obtain these two entities at the same position. The Cs MOT is here displaced from the Rb BEC by 7 mm which is the distance between the trap minima of the QUIC and the quadrupole trap. In our case, we use the method of magnetic transport along with the optical dipole trap to transport a cold thermal Rb cloud to the position of the Cs MOT.

There are various possibilities of bringing the two species together. Let us consider the possibility of transporting the Rb condensate from the QUIC to the MOT position. This has been demonstrated in [123]. Here, the condensate was transported over a distance of 40 cm through an optical tweezer which is actually a focussed dipole trap beam. The transport was achieved by translating the focussing lens, which was placed on a linear translation stage. However, such stages can cause vibrations leading to atom losses due to heating. In this case, two stages of isolation were implemented using rubber dampers and lead weights to avoid this problem. This is therefore a cumbersome and an expensive process since a very good translation stage needs to be used for this purpose. Moreover, shot to shot fluctuations were prominent due to the position instability of the tweezer when the stage was moved back and forth. Another possibility is the transport using a 1D optical lattice [124]. This does not create mechanical vibrations as the lattice is moved by introducing a relative detuning between the two beams forming the standing wave. Positioning is also quite precise. However, vibrations are present in the form of phase fluctuations. Also, the need for an optical lattice reduces the feasibility of this method in our setup where we work with a crossed dipole trap for our Rb atoms. Moreover, these lattices are tightly confining potentials reducing the number of atoms in the condensate. Another problem that hinders the transport of the condensate is its limited lifetime, shown for a Rb BEC in the $|2,2\rangle$ state in figure 4.1. The preparation of the condensate in the dipole trap is shown in section 4.2. The lifetime measurement is done by storing the BEC in the dipole trap after evaporation for about 2.5 s. The exponential fit yields a $1/e$ lifetime of 400 ms. Losses are attributed to inelastic collisions due to dipolar relaxation [63, 64]. This limited lifetime of the condensate puts a limit on the time duration of the transport. Preparation of the condensate in any other state requires changes in the optical pumping setup.

The other possibility is to transport the Cs MOT to the position of the QUIC trap. The movement of the quadrupole trap in space by a distance of 7 mm requires large offset fields of about 350 G which the offset coils currently in use cannot produce. More robust coils will be required for the purpose. A shift in the position of the quadrupole potential minima has been shown in [125], where nine overlapping quadrupole coils have been used to produce a shift of 33 cm. Moreover, the fluorescence detection system used to detect the Cs atoms has a field of view of 60 μm and therefore the Cs MOT cannot be detected anymore if its position is changed beyond this limit. The magnetic transport employed in our experiment is discussed below.

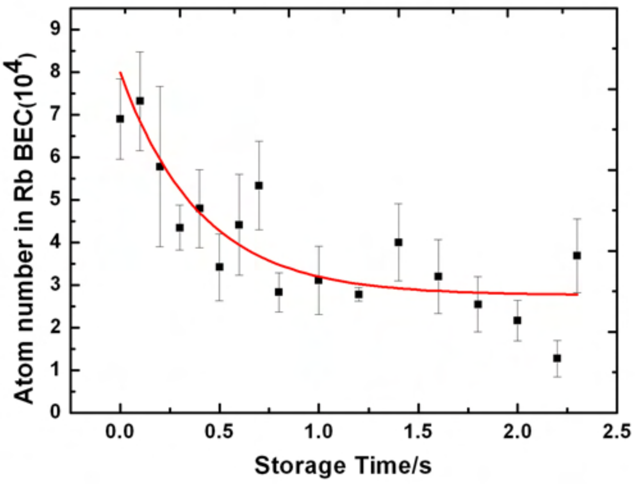

Figure 4.1: Lifetime measurement of the condensate in the $|2,2\rangle$ state in the dipole trap. The number of atoms in the Rb condensate is plotted against the storage time in the dipole trap. The loss of atoms is evident from the graph. Only about 20% of the atoms remain in the condensate after a storage time of 2 s. The red curve is an exponential fit to the data. This gives a $1/e$ lifetime of about 400 ms. The error bars represent the statistical error of the data points.

4.1.1 Magnetic Transport without the Dipole Trap

The method of magnetic transport has been demonstrated in [126]. Here, a degenerate heteronuclear mixture of Rb and Potassium (K) has been transported over a distance of 6 mm. The QUIC trap used here is similar to ours. Transport is realized by using an additional pair of coils in anti-Helmhotz configuration parallel to the quadrupole coils of the QUIC trap. This shifts the centre of the QUIC trap. The displacement and field offset depend upon the currents flowing through the coils. The required shift can therefore be obtained by choosing the currents flowing through the coils.

The magnetic transport that we implement in our experiment, however, does not involve an additional pair of quadrupole coils. It is achieved by changing the current flowing through the existing quadrupole coils (MOT coils) which leads to a displacement of the centre of the QUIC trap. The experimental details are given below.

Experimental Sequence

In our experiment, we do not transport the condensate created in the QUIC trap, this is because of the limited lifetime of the BEC as already mentioned before. Instead,

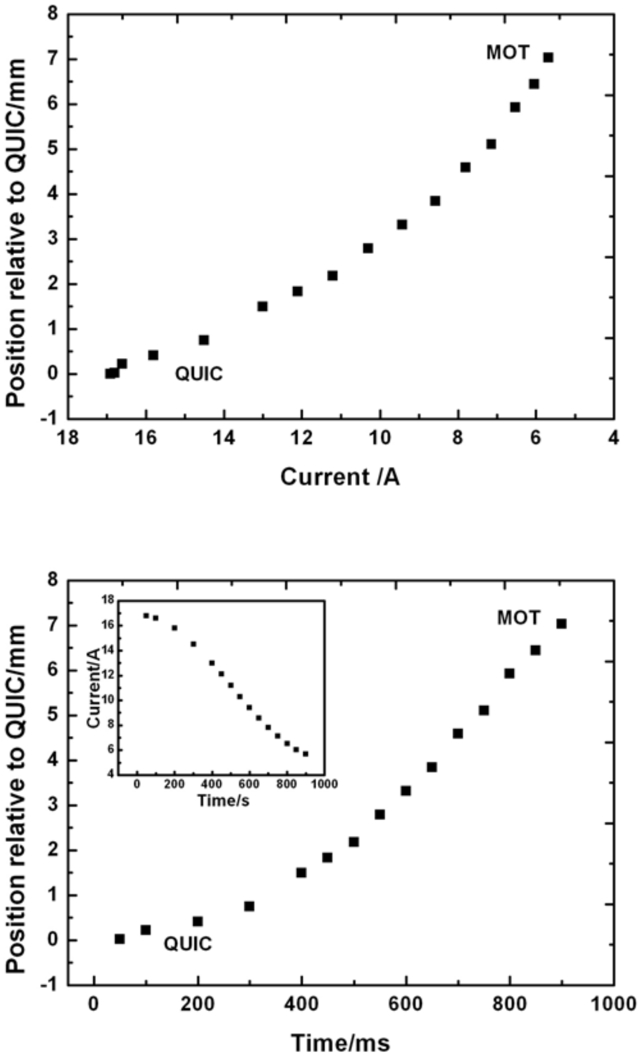

Figure 4.2: In the upper graph, the variation in the cloud position relative to the original position of the QUIC trap is plotted against the current flowing through the quadrupole coil during the transport. As seen from the graph, the trap minimum is displaced by 7 mm as the current is nearly 5 A. The displacement is towards the MOT position. The QUIC and the MOT positions are labelled. The lower graph shows the displacement with respect to the transport time. The total time required for this displacement is less than 1 s. The inset shows the current ramp used for the transport.

we transport a thermal cloud which has a temperature of about 1 μK and a lifetime of about 120 s. The evaporation in the QUIC trap is therefore carried out for about 19 s to generate the cold thermal cloud after which the transport begins. The current through the quadrupole coil is chosen depending upon the displacement required. In order to know this displacement, the atoms are imaged in the quadrupole trap as well as the QUIC trap and the position of the cloud is noted. The position in all the three axes is obtained by using both the cameras as mentioned in section 3.6. The current through the quadrupole coil is reduced in steps and the position of the cloud is ascertained for each current for which the camera had to be moved four times during the entire displacement. The current was reduced from 16.9 A to 5 A to obtain the necessary displacement of 7 mm. The current through the Ioffe coil remained unchanged at 16.9 A. This displacement is however an approximate one, the exact positioning with respect to the MOT is explained in the next chapter. The ramp used was a cosine ramp, such that the transport is slow in the beginning and in the end. This ramp was chosen to minimize excitations in the atom cloud which were measured experimentally. The transport was accomplished in less than a second. The change in the position of the trap minimum relative to the original position of the QUIC trap with respect to the current flowing through the quadrupole coil and the time required for the transport is shown in figure 4.2. This was the first attempt to displace the trap minimum. Atom losses and heating of the cloud were not observed. There were however, some problems associated with this transport method. The transport was not completely adiabatic and therefore, an oscillation of the cloud was obtained at the final position. The trap frequencies were drastically reduced due to the change in the trap parameters from 180 Hz at the position of the QUIC to less than 10 Hz at the quadrupole trap position. A gravitational sag of ~ 2 mm was also observed due to a lower field gradient.

An increase in the transport time to obtain an adiabatic transport would increase the length of the experimental sequence. This is evident from the low trap frequency values at the end of the transport which give an oscillation period of about 200 ms. The duration of an adiabatic transport would then be of the order of a few to a few tens of seconds and is therefore not an ideal solution to get rid of the oscillations. This problem was then solved by using a two step ramp, where the current was first reduced to a value close to 5 A in 900 ms. The oscillations of the cloud were recorded at this position. The phase and period of the oscillations were therefore ascertained. The cloud was then stored at this position for 85 ms after which the current was reduced to 5 A in about 60 ms which is about half the oscillation period. The idea behind this approach is to break the oscillation at an intermediate current value and then transporting the cloud to its desired position. This reduced the oscillation amplitude to about 10% of its initial value. The gravitational sag was compensated by using a levitation coil. This coil is shown in figure 3.3. This has an outer diameter of 130 mm, an inner diameter of 50 mm and has 120 turns with an inductance of 1.5 mH. This coil is placed below the glass cell as shown in figure 3.3 surrounding the MOT objective and is water cooled. This creates a gradient of about 10 G/cm in the vertical direction and compensates for the gravitational sag. The ramp used and the current flowing through the coil are discussed in the next section in concurrence with

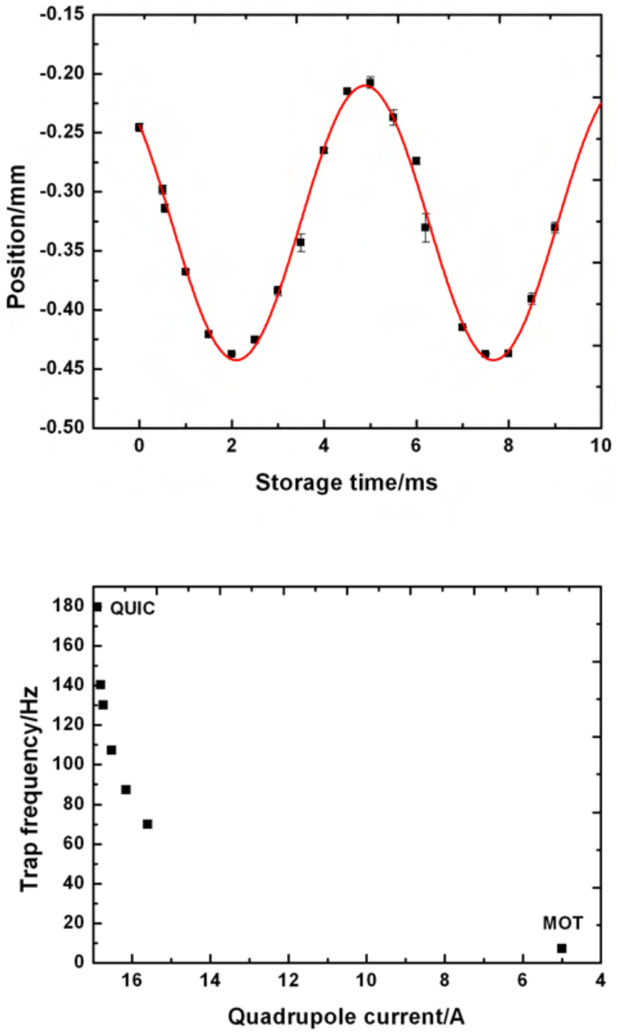

Figure 4.3: The upper graph shows measurement of the radial trap frequency for the original QUIC trap. The position of the oscillating cloud is recorded for different storage times after the atoms are deflected from equilibrium. The red curve is a sine fit to the data whose period gives the trap frequency which is equal to 179.8±0.6 Hz. The lower graph shows the measured radial trap frequencies for different positions during the transport. The axial trap frequency could not be measured due to the very small deflection that was possible in that direction with the available field gradient. However, it is also assumed to have lower values at the end of the transport, the variation here being not so significant, since the axial trap frequency at the QUIC position is also low at 18 Hz. The drastic change in the trap frequency from 180 Hz to less than 70 Hz within 150 ms is observed. The QUIC and the MOT positions are labelled.

the dipole trap. The third problem was the drastic reduction of the trap frequencies. To evaluate this, the trap frequencies were measured for different positions during the transport. For this, the atoms were given a slight deflection using the levitation coil such that they were displaced from their equilibrium and start oscillating in the trap with their trap frequencies. For this purpose, a current of 750 mA was flown through this coil where it was ramped up in 40 ms and ramped down in 10 ms. The trap frequency was then measured by storing the atoms in the trap for various times (of the order of a few ms) and noting down the position of the cloud. The trap frequency measurement for the QUIC trap at its original position is shown in figure 4.3. The measured trap frequency of 179.8 ±0.6 Hz agrees quite well with the theoretical value of 180 Hz. This measurement was repeated for various stages of the transport i.e. at different cloud positions corresponding to different quadrupole currents. The trap frequencies are plotted against the quadrupole currents in figure 4.3. A drastic change in the frequencies from 180 Hz to 70 Hz is observed in the first 150 ms of the transport. This problem was solved by using the dipole trap during the transport and is discussed in the next section.

4.1.2 Magnetic Transport along with the Dipole Trap

The problem of the trap frequency change was taken care of by ramping up the axial arm of the dipole trap during the transport. This provided a better enclosure along the gravitation and imaging axes and stabilized the trap frequencies at 120 Hz.

The dipole trap was focussed onto the position of the quadrupole trap (MOT position). The details of the trap including the trap parameters have already been discussed in section 3.7. In order to align the trap, the dipole trap beam was overlapped at two positions, at the QUIC as well as at the quadrupole trap minima. The trap was then ramped up in 100 ms at the beginning of the transport to its maximum power of 2 W and was kept at this value till the end of the transport. This time was chosen for an adiabatic ramping. The ramp was linear with rounded ends in the beginning and in the end to avoid any excitations in the atom cloud during the ramping up of the dipole trap. At the same time, the levitation coil was also ramped up in 50 ms to a current of about 1.7 A and was kept at this value for 500 ms after which it was ramped down in 600 ms. This configuration maintained a constant trap frequency of 120 Hz at the end of the transport and also compensated for the gravitation sag. Changes in the dipole trap position could also be compensated by changing the levitation ramp. The ramps were optimized on the basis of experimental results, i.e. for optimal atom number and temperature of the clouds. A schematic of the ramps used are shown in figure 4.4. With this, a 1 μK cloud in the $|2, 2\rangle$ was transported to the centre of the quadrupole coils (quadrupole minima). As already mentioned, an exact overlap with the Cs MOT position will be discussed in the next chapter.

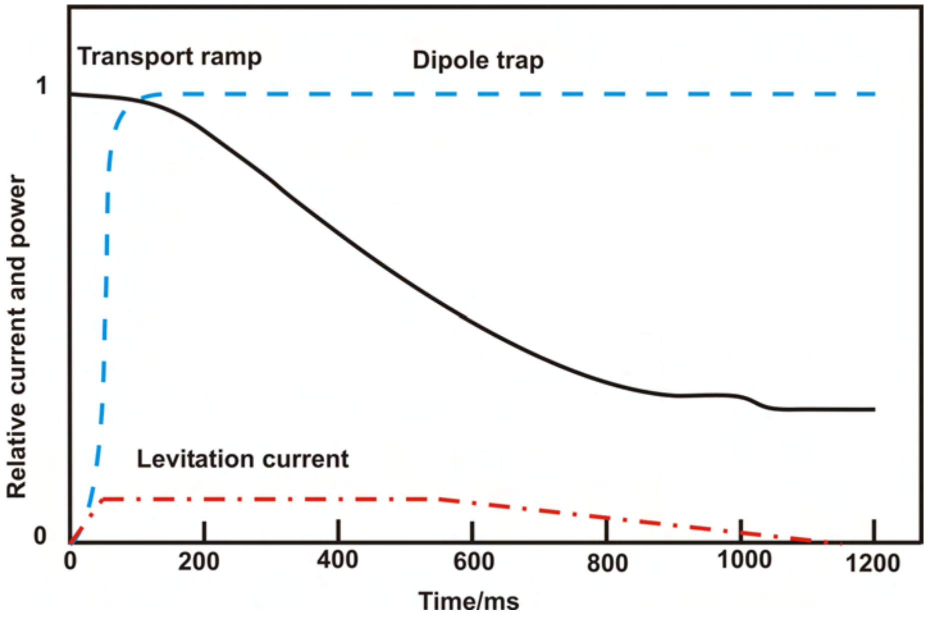

Figure 4.4: A schematic of the ramps used during the transport is shown. The x-axis shows the time in ms whereas the y-axis is arbitrary and shows the relative current and power normalized to one. The levitation coil current (red, dash dot curve) is ramped up to a current of 1.7 A and then ramped down after 500 ms. The dipole trap (blue, dashes curve) is ramped up to a power of 2 W in 100 ms and stays there. The transport curve (black line) shows the ramping down of the current through the quadrupole coil in two steps from 16.9 A to 5 A.

Having transported a thermal cloud to the position of the MOT, the next step is to obtain a Rb BEC in the dipole trap. This will be discussed in the next section.

4.2 BEC in the $|2,2\rangle$ State of the Crossed Dipole Trap

Although BEC was first realized in a magnetic trap, the various limitations of this trap, which have already been discussed earlier, have encouraged its production or transfer into the optical dipole trap for various experiments. Optical confinement of a BEC was demonstrated in [127] and evaporative cooling leading to an increase in phase space density [128] as well as condensation [129, 130] by lowering the trap depth have also been carried out in single beam as well as crossed dipole traps. In our case, optical confinement of the Rb BEC is necessary as we need to study its interaction with Cs which is trapped in a MOT. As already explained in the last section, the transport of a Rb BEC prepared in the QUIC trap in the $|2,2\rangle$ state over a period of 1 s is not possible due to its limited lifetime. Therefore, a 1 μK cloud is transported. This cloud is then evaporatively cooled in the dipole trap to quantum

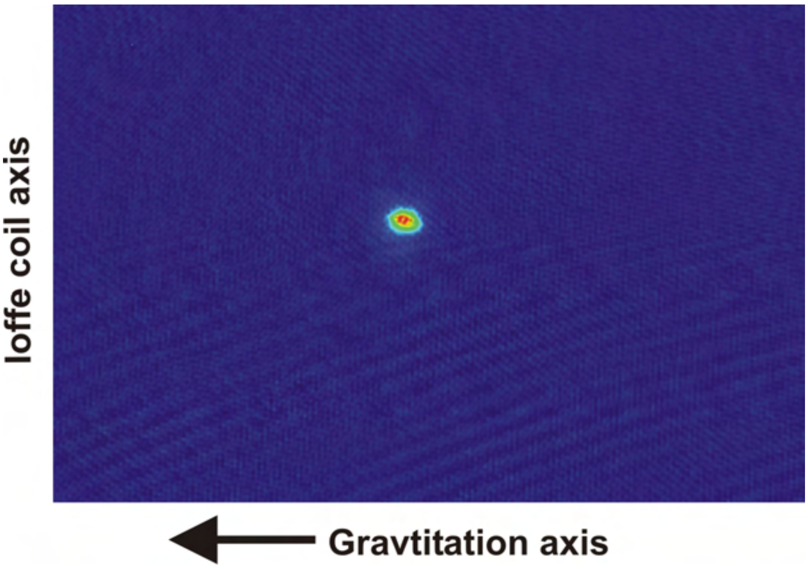

Figure 4.5: A false colour image of a Rb BEC obtained in a crossed dipole trap after a time of flight (TOF) of 32 ms is shown. The axes shown are the gravitation axis and the Ioffe coil axis. The arrow points in the direction of gravitation and depicts the direction in which the BEC falls during the TOF.

degeneracy.

Evaporative Cooling through Lowering the Trap Potential

The axial arm of the dipole trap is ramped up during the transport. However, in order to obtain a uniform confinement in 3D and a larger trap volume, a crossed dipole trap is employed. After the transport, the radial arm of the dipole trap is ramped up in 200 ms to its maximum power of 2 W and the magnetic fields are switched OFF such that the atoms are confined only optically. The ramping up time is chosen such that the transfer into the crossed trap is adiabatic. In the experiment it is optimized based on the atom number and the temperature of the transferred cloud. The radial beam is coarsely aligned by overlapping it with the cloud position. This is done with the help of both the cameras. The fine alignment is achieved again by optimizing the atom number and temperature in the trap. The atoms are stored in the crossed dipole trap for about 200 ms. This time is more than sufficient to get rid of any residual fields arising from the switching OFF of the magnetic trap or the levitation coil. After this, the evaporation is carried out. For this, the power of the axial as well as the radial arm of the dipole trap is lowered, thereby, lowering the trap depth. A logarithmic ramp is used where the power of the axial arm is reduced from 2 W to 1 W and that of the radial from 2 W to 0.8 W in 3 s. The quantization axis is provided by a pair of Helmholtz coils parallel to the quadrupole coils as shown in figure 3.3. A condensate with about 10^5 atoms is obtained. A picture of a Rb condensate in the dipole trap after a TOF of 32 ms is shown in figure 4.5.

Lowering the trap depth decreases the trap frequencies and therefore reduces the rate of elastic collisions. This leads to inefficient evaporation. Most experiments where the atoms are loaded directly from the MOT into the dipole trap, therefore, either use higher intensities or a tighter focus for a better confinement. However, in our case, since we already load a pre-cooled cloud ($1\,\mu$K) into the dipole trap, neither of the above is inevitable. Hence, we can work with relatively small powers (2 W in each beam) and larger beam waists (86-172 μm) which increases the trap volume in our case.

Trap Frequencies

Trap frequencies are important parameters characterizing a trapping potential. The trap frequencies for the crossed dipole trap have been calculated in section 3.7 for its maximum trap depth. This has been experimentally measured here. One way to do this is to displace the atoms from their equilibrium in the trap such that they start oscillating in the trap with the trap frequencies. This has been done in the magnetic trap in our case, the results of which have already been shown in section 4.1. Here, another method viz. the method of parametric heating [131, 132] has been employed to measure the trap frequencies.

This method is based on the observation of atom losses in the trap by a modulation of the laser intensity. Intensity fluctuations lead to heating, the rate of which depends on the second harmonic of the trap frequency, hence it is called parametric heating. Losses of atoms from the trap are observed for modulation at twice the trap frequency.

The Rb atoms are evaporatively cooled and a sample with $\sim 2 \times 10^5$ atoms at 200 nK is prepared in the dipole trap. The axial arm of the dipole trap is then modulated by a sine waveform with an amplitude corresponding to about 50% of the power in the axial beam, for 2 s. The modulation frequency is varied and the atom number is noted for each frequency. Figure 4.6 shows the measurement of the trap frequencies by the method of parametric heating. Two dips are observed in the atom number corresponding to losses at two different modulation frequencies. Since, losses are observed at a modulation frequency which is equal to twice the trap frequency, the trap frequency can be obtained from this measurement. The trap frequencies extracted from the measurement are therefore, given by $\omega_1 = 2\pi \times (53.2 \pm 0.7)\,\mathrm{Hz}$ and $\omega_2 = 2\pi \times (120 \pm 2)\,\mathrm{Hz}$. However, in our case, the trap frequencies are different in all the three directions (see section 3.7). The trap frequencies can be calculated for this lowered trap using equations (3.25) and (3.26) and are given by $\omega_x = 2\pi \times 166\,\mathrm{Hz}$, $\omega_y = 2\pi \times 59\,\mathrm{Hz}$ and $\omega_z = 2\pi \times 117\,\mathrm{Hz}$. The values of the trap frequencies from the measurement agree reasonably well with the theoretical values for the imaging axis (z) as well as the Ioffe axis (y). The small discrepancy is attributed to the uncertainties

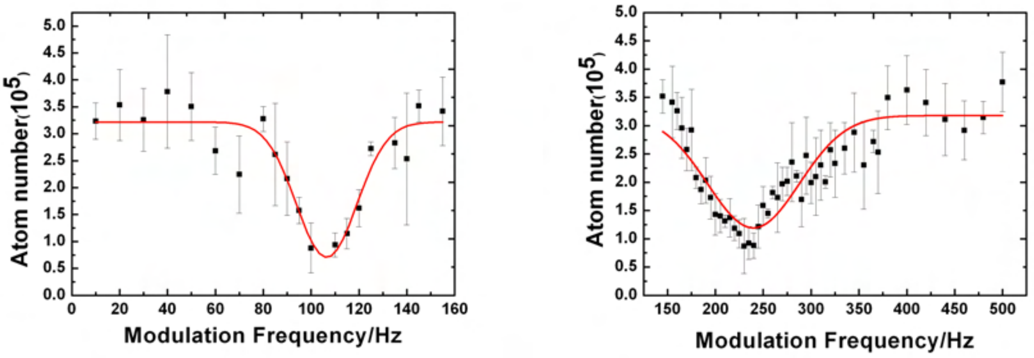

Figure 4.6: The measurement of the trap frequencies by the method of parametric heating is shown. The atom number is plotted against the modulation frequency. Loss features are observed at modulation frequencies equal to twice the trap frequencies. The red curves are the gaussian fits to the data points, the centre of which gives the modulation frequency corresponding to the atom losses. The corresponding trap frequencies are $\omega_y = 2\pi \times (53.2 \pm 0.7)\,\mathrm{Hz}$ and $\omega_z = 2\pi \times (120 \pm 2)\,\mathrm{Hz}$.

in the beam powers and beam waists. However, a third loss dip corresponding to the trap frequency along the gravitation axis (x) is not observed. This could be because of the broad spectrum of the second loss feature which is $96 \pm 10\,\mathrm{Hz}$ in terms of the modulation frequency. According to the calculated value of ω_x, this loss should be observed at a modulation frequency of 332 Hz, which is less than 100 Hz away from the dip corresponding to ω_z. Hence, it could probably not be resolved. An attempt was made to do this measurement at a lower modulation amplitude, but the losses observed in that case were smaller than the shot to shot atom number fluctuation.

4.3 Microwave Transition to the $|1, 1\rangle$ State

The $|2, 2\rangle$ state of ^{87}Rb is not convenient for the study of interactions as the condensate cannot be stored in this state for a long time. Hence, the Rb atoms need to be prepared in another state to facilitate such studies. In the absolute ground state of Rb i.e. the $|1, 1\rangle$ state, a suppression of the inelastic two body processes occurs due to the energy and angular momentum conservation laws. This state therefore, also has a larger lifetime due to the consequent suppression of losses. This is therefore, the state where the Rb condensate will be stored for all future experiments where Cs will be trapped in a species selective optical lattice (see chapter 6). For experiments demonstrated in this thesis, the Rb atoms are not stored in this state, because it is sensitive to the magnetic fields. However, the transition from the $|2, 2\rangle$ to the $|1, 1\rangle$ state has been demonstrated here as a requirement for future experiments with Cs in the species selective optical lattice and also as a pathway to the preparation of the atoms in the $m_f = 0$ state. Moreover, microwave spectroscopy has been carried out with this transition where a calibration of the offset coils used for creating a homogeneous magnetic field, has been done.

The theoretical framework of the interaction of a coherent radiation with a two level atom has been discussed in chapter 2. Here, it was shown that, if the atom can be considered as a two level system, then population transfer between these two levels occurs depending upon the radiation pulse applied. Application of a π pulse, leads to a complete transfer of atoms from one state to the other at resonance. Various extensions of this method have also been demonstrated, viz. transfer using two resonant pulses or a two photon transfer. These two methods will be discussed in the next section. Another alternative for population transfer is an adiabatic passage [133], where the frequency of the external field is slowly (adiabatically) tuned across the resonance. This method does not require an external field with very stable amplitudes and frequencies and leads to a 100% transfer. However, in our case, the amplitude and frequency fluctuations of the microwave as well as the RF (which will be discussed in the next section) are negligible, thereby providing stable and complete population transfer using resonant pulses. The advantage of using resonant pulses over the adiabatic transfer is that they are much faster, lying between 20 and $300\,\mu$s in our case compared to about a second required for an adiabatic transfer. A single photon microwave transition is discussed here.

4.3.1 Microwave Spectroscopy

The approximation of a two level system assumed in the model discussed in chapter 2 depends on various factors viz. the strength of the atom radiation coupling, the detuning of the radiation field from the atomic transition frequency and the monochromatic nature of the radiation field. The strength of the coupling depends on the Rabi frequency which in turn depends on the field strength and will be discussed in the next part of this section. The monochromatic nature of the radiation field is important so that it does not couple to the other states. Let us consider the ground state hyperfine structure of ^{87}Rb. In the absence of any external field, the $f = 2$ and $f = 1$ states are degenerate. Application of a magnetic field results in the splitting of these states into $2f + 1$ states, i.e. the $f = 2$ state is split into five and the $f = 1$ is split into three. We are interested in the transition $|2, 2\rangle \rightarrow |1, 1\rangle$. The splitting of the states depends on the strength of the applied magnetic field. For, weak magnetic fields, f is a good quantum number and the splitting is linear with respect to the magnetic field. For very strong fields of about a thousand Gauss, the energy shift is given by the Paschen-Back effect. The energy shift is in general given quantitatively by the Breit-Rabi formula [134, 135], which has a simple form for the ground state. This is given by

$$E_{j=1/2 m_j i m_i} = -\frac{\Delta E_{\text{hfs}}}{2\,(2i+1)} + g_i \mu_{\text{B}} m B \pm \frac{\Delta E_{\text{hfs}}}{2} \left(1 + \frac{4mx}{2i+1} + x^2\right)^{1/2} , \tag{4.1}$$

where ΔE_{hfs} is the hyperfine splitting, $m = m_i \pm m_j$ and x is given by

$$x = \frac{(g_j - g_i)\,\mu_{\text{B}} B}{\Delta E_{\text{hfs}}} , \tag{4.2}$$

where g_j and g_i are the Lande factors. For small values of x i.e. for $x < 0.1$, [134] the low field regime is valid where the splitting varies linearly with the magnetic field. The value of x was calculated to be ~ 0.04 for a magnetic field of 15 G for $i = 3/2$ in our case. Since, we work with fields < 15 G, we are well within the weak field regime where the Zeeman splitting is anomalous. Here, the splitting is given by 700 kHz/G for the ^{87}Rb ground state [96] which is very small compared to the hyperfine splitting given by 6.835 GHz. The coupling of the two states under consideration depends upon this splitting relative to the spectral width of the microwave frequency and its detuning from resonance. For the pulse durations considered in our experiment, the spectral width of the radiation is of the order of a few tens of kHz.

Resonance Measurement

The microwave setup has already been explained in section 3.5. The R&S 1 signal generator whose frequency is multiplied by the PLDRO is switched to 9.94671 MHz. The output of the PLDRO is added to the frequency generated from the R&S 2 signal generator using the mixer, which is then used for pulse generation. The R&S 2 generator is switched ON using the RF switch shown in figure 3.6, replacing the TABOR (used for evaporation). The rest of the setup is the same as that for evaporation. The entire setup is triggered from the pulse generator which is in turn triggered from the computer and a trigger from the mains. The pulse generator also sets the duration of the pulse. The timing of the pulse can be set by setting an appropriate delay using the pulse generator. However, this is accurate only to 20 ms which is limited by the trigger from the mains, which has a frequency of 50 Hz. Therefore, the offset field as well as the frequency generated from the signal generators should be timed accordingly.

The pulse is applied after the evaporation in the dipole trap. The offset field is already present during evaporation providing the necessary quantization axis as mentioned before. A current of 2.5 A is passed through these coils providing a field of about 10 G. The current to the coils is provided by a power supply (Toellner, Model no. TOE 8851-32). In order to measure the microwave spectrum, the power of the microwave radiation is attenuated by about 60% of the maximum power (8 W) using the PIN diode attenuator. This is done to alleviate power broadening to obtain a

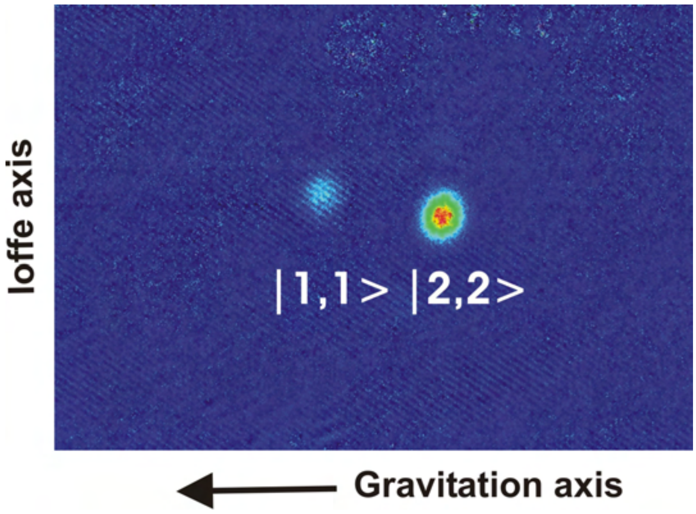

Figure 4.7: The two Rb clouds in the $|2,2\rangle$ and the $|1,1\rangle$ states are shown separated in space through a Stern Gerlach experiment. The gradient is applied during the TOF measurement and the clouds are imaged after a TOF of 13 ms. The thermal clouds have a temperature of about 200 nK and there are about 1.9×10^5 atoms in the $|2,2\rangle$ state and about 4.4×10^4 atoms in the $|1,1\rangle$ state. They are separated by $3\mu_\mathrm{B}B/2$ in space. The arrow along the gravitation axis points in the direction of gravitation and therefore, represents the direction in which the thermal cloud falls and expands during the TOF measurement.

narrow spectrum whose width is limited by the Fourier limit. The pulse duration is chosen to be 50 μs. A longer pulse would give a narrower spectrum, however, in our case, the spectral width is Fourier limited at the chosen pulse duration and microwave power, therefore, we do not use a longer pulse. The population in the two states is determined by the Stern Gerlach method. This is achieved by flowing a current through the levitation coil during the TOF measurement which provides the necessary gradient for the separation of the m_f states in space. The two clouds are separated by $3\mu_\mathrm{B}B/2$. Figure 4.7 shows the two Rb clouds in the $|2,2\rangle$ and $|1,1\rangle$ state separated in space. The repumper light is switched ON during the TOF to enable the observation of the atoms in the $f=1$ state. Therefore, both the clouds can be observed. The microwave spectrum is shown in figure 4.8. The errors represent the statistical error of the data points. A gauss is fitted onto the data, the centre of which corresponds to the resonance, the frequency of which is 52.9782 ± 0.0002 MHz. This is the frequency generated by the R&S2 generator which replaces the TABOR after evaporation. About 20% of the atoms are transferred to the $|1,1\rangle$ state at this frequency and microwave power.

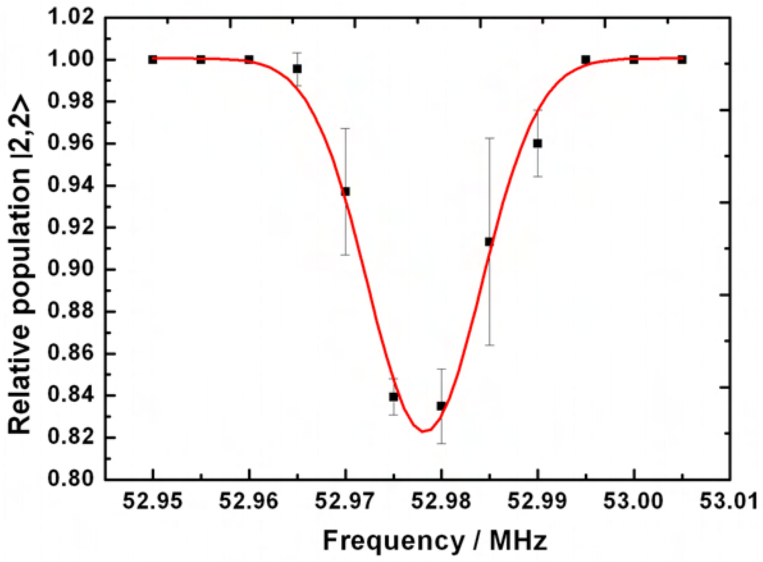

Figure 4.8: The relative population of the atoms in the $|2, 2\rangle$ state with respect to the total number of atoms in both the $|2, 2\rangle$ and $|1, 1\rangle$ states versus the microwave frequency generated by the R&S 2 generator is shown. The dip corresponds to the resonance frequency of the $|2, 2\rangle \rightarrow |1, 1\rangle$ atomic transition. The red curve is a gaussian fit to the data, whose parameters give the value of the resonance frequency. Note that at resonance only about 20% of the atoms are transferred to the $|1, 1\rangle$ state due to the attenuated microwave power.

Calibration of the Offset Field

The microwave radiation can be used for a calibration of the coils providing the offset fields necessary for the splitting of the degenerate hyperfine levels. In our case, we have done this for three pairs of coils in all the three axes viz. x, y and z. In the imaging axis (z), the coils used are the ones parallel to the MOT coils as shown in figure 3.3. In the other two axis, the coils used are simple wires, which do not allow flow of currents larger than about 10 A. All the three coils were calibrated by measuring the microwave spectrum for currents between 1-10 A flowing through them. Therefore, the resonance frequency corresponding to each current flowing through the coils was ascertained for all the coils for the $|2, 2\rangle \rightarrow |1, 1\rangle$ transition. Figure 4.9 shows the calibration of the three coils. The blue dot on each graph represents the frequency corresponding to the transition $|2, 0\rangle \rightarrow |1, 0\rangle$ calculated by subtracting the frequency generated by the PLDRO from 6.835 GHz (hyperfine splitting of the ground state). Ideally, an extrapolation of the linear fit to the frequencies should cross this point. The offset corresponds to stray magnetic fields or the earth magnetic field

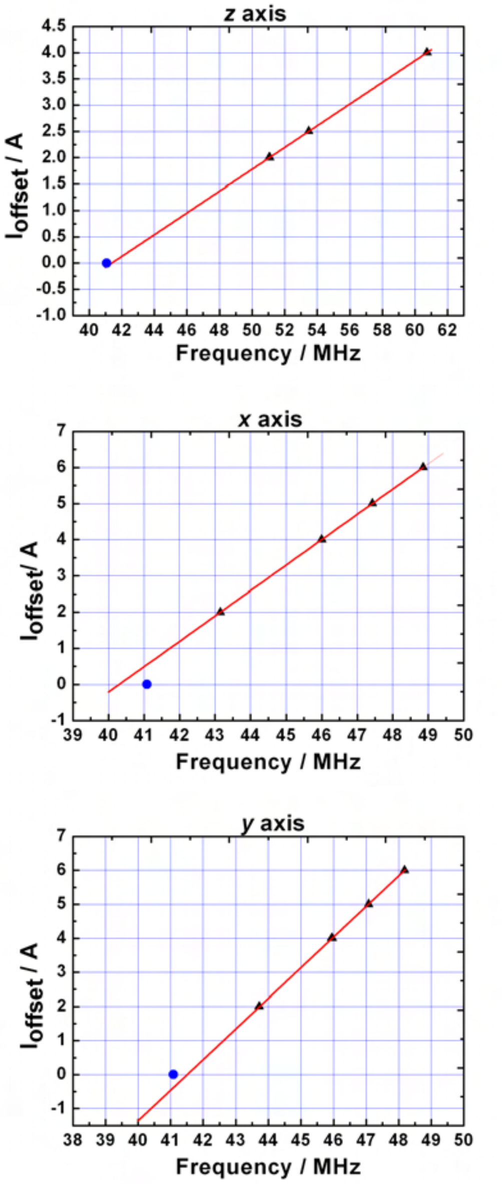

Figure 4.9: The calibration measurement of the offset coils in all the three directions is shown. The current through the coils is plotted vs. the resonance microwave frequency (frequency generated by the R&S 2 generator). The upper most graph represents the coil in the imaging axis (z), the middle one, the gravitation axis (x) and the lower one the axis of the Ioffe coil (y). The red curves are the linear fits to the data points. The blue dot in each graph represents the frequency corresponding to the zero magnetic field, which is also the frequency of the clock transition $|2,0\rangle \rightarrow |1,0\rangle$. Note that, an extrapolation of the linear fit does not pass through this dot.

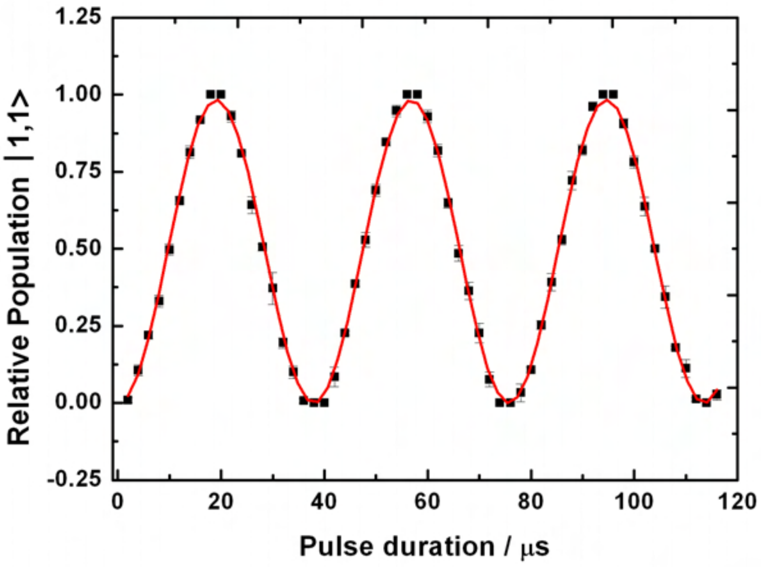

Figure 4.10: Rabi Flopping: The relative population of the atoms in the $|1,1\rangle$ state with respect to the total number of atoms in the $|1,1\rangle$ and $|2,2\rangle$ states versus the pulse duration is shown. The red curve is a sine squared fit to the data which gives the value of the Rabi frequency to be $2\pi \times (26.48 \pm 0.04)$ kHz. Note that a 100% population transfer is obtained after 19 μs.

along these directions. The splittings produced by the coils for the same current in the gravitation (Ioffe) axis are four (three) times smaller than that produced along the imaging axis due to a proportionally smaller magnetic field strength.

4.3.2 Rabi Oscillations

After having measured the resonance frequency, the coupling strength between the two levels can be determined. This can be done by measuring the Rabi frequency which is the frequency of the population oscillation between the two coupled states. For this, the frequency of the R&S 2 generator is kept at the resonance frequency and the duration of the microwave pulse is varied. The population of the two states is ascertained for each pulse duration. In our case, the first measurement of the Rabi oscillations gave a frequency of about 10 kHz. The microwave waveguide antenna was moved closer to the glass cell and the existing cable, connecting the amplifier to the waveguide, was replaced by a low loss cable with a length of 0.5 m . These two improvements led to a doubling of the measured Rabi frequency. Figure 4.10 shows the Rabi oscillations between the $|2,2\rangle$ and the $|1,1\rangle$ state. The Rabi frequency measured is $2\pi \times (26.48 \pm 0.04)$ kHz. A 100% population transfer is obtained after

19 μs. Moreover, the oscillations are very stable, even over time scales of a few ms which indicates a coherence time of the order of a few ms. The stability of the oscillations enables us to prepare the atoms in the $|1,1\rangle$ state using a single π pulse.

4.4 Preparation of the BEC in the $|1,0\rangle$ State

As already mentioned many times before, we prepare our Rb BEC or a cold thermal Rb cloud in the $m_f = 0$ state for experiments with Cs. This is because this state is magnetically insensitive. The Cs atoms are trapped in a high gradient MOT (300 G/cm) and this gradient would push out all the atoms if they are in any of the magnetically sensitive states viz. $m_f = 1, m_f = 2$ when the Cs MOT is overlapped with the Rb cloud. For all future experiments, however, Cs would be trapped in a species selective optical lattice and therefore Rb would be confined in the absolute ground state i.e. the $|1,1\rangle$ state.

The two states with $m_f = 0$ which are used in our experiments with Cs are the $|1,0\rangle$ state and the $|2,0\rangle$ state. The preparation of the atoms in the $|2,0\rangle$ state is relatively simple because of the use of two resonant microwave pulses, $|2,2\rangle \rightarrow |1,1\rangle$ and $|1,1\rangle \rightarrow |2,0\rangle$ one after the other. The Rabi frequency of the $|1,1\rangle \rightarrow |2,0\rangle$ transition is $2\pi \times (3.083 \pm 0.008)$ kHz. This therefore, does not require an extra RF setup. However, the preparation of the Rb atoms in the $|1,0\rangle$ state requires an additional RF setup. Two methods are discussed below.

4.4.1 Transfer to the $|1,0\rangle$ State through a Two Photon Microwave Transition

In order to transfer the atoms from the $|2,2\rangle \rightarrow |1,0\rangle$ state, a single photon transition is not sufficient. This is because $\Delta m_f = 2$ for this transition and is therefore, forbidden by the selection rules ($\Delta m_f = 0, \pm 1$). However, these two states can be coupled through a two photon transition. A schematic of the two photon transition is shown in figure 4.11. In order to couple the two states, the microwave frequency is detuned by a value Δ from the resonance frequency of the $|2,2\rangle \rightarrow |1,1\rangle$ transition. A RF is applied simultaneously where the RF frequency is detuned by the same value with respect to the $|1,1\rangle \rightarrow |1,0\rangle$ transition. When the detuning Δ is sufficiently larger than the individual Rabi frequencies of both these transitions then, the intermediate $|1,1\rangle$ state is not occupied. The three level system can then be considered as a two level system and the states $|2,2\rangle$ and $|1,0\rangle$ are considered to be coupled via the two photon transition. The corresponding two photon Rabi frequency is then given by [136]

$$\Omega \propto \frac{\Omega_1 \Omega_2}{\Delta} , \tag{4.3}$$

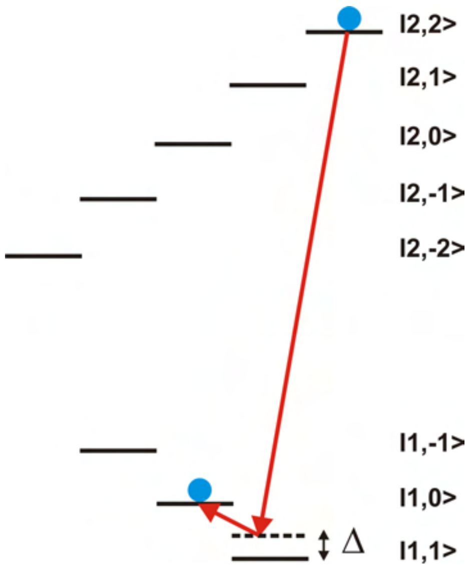

Figure 4.11: A schematic of the two photon transition is shown. The atoms in the $|2,2\rangle$ state are transferred to the $|1,0\rangle$ state via the intermediate $|1,1\rangle$ state. The detuning Δ is chosen such that the microwave frequency is smaller than the resonance frequency for the transition $|2,2\rangle \rightarrow |1,1\rangle$. The RF frequency is then chosen accordingly.

where Ω_1 and Ω_2 are the Rabi frequencies of the individual single photon microwave and RF transitions respectively and Δ is the detuning. Since the Rabi frequency is inversely proportional to the detuning Δ, the value of Δ needs to be chosen carefully. It should be set large enough such that the intermediate state is not occupied by the single photon transition and at the same time, it should be small enough to provide a strong coupling between the two states. The detuning can be chosen to be such that the microwave frequency is smaller than the resonance frequency of the $|2,2\rangle \rightarrow |1,1\rangle$ transition as shown in figure 4.11. It could also be chosen such that the frequency is larger than the resonance frequency. However, this needs to be decided keeping in mind the possibility of occupation of other states according to the selection rules.

The RF setup used in our case, consists of a waveform generator (Agilent, Model no. 8648C) which provides the necessary RF frequency. This is then connected to a preamplifier (Motorola) through an RF switch which receives the required trigger from the experimental sequence. The preamplifier is then connected to the main amplifier which gives a total output power of 10 W. The RF antenna is a simple coil which is wound around the glass cell. The polarization direction is along the gravitation axis, which is the same as that of the microwave antenna. The required offset field is provided by the same pair of Helmholz coils as in the case of the single photon transition discussed in the previous section.

The pulse is applied after the evaporation of the atoms. The two photon spec-

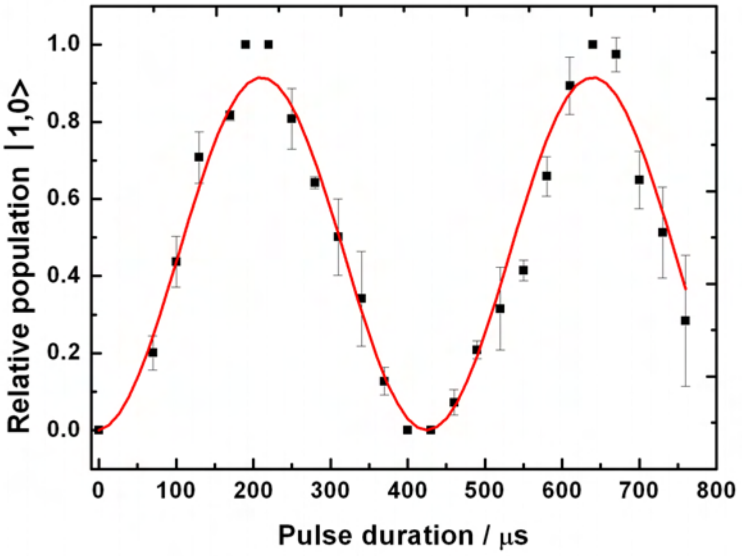

Figure 4.12: Rabi Flopping: The relative population of the atoms in the $|1,0\rangle$ state with respect to the total number of atoms in the $|1,0\rangle$ and $|2,2\rangle$ states versus the pulse duration is shown. The red curve is a sine squared fit to the data which gives the value of the Rabi frequency to be $2\pi \times (2.33 \pm 0.03)\,\mathrm{kHz}$. The error bars are the statistical error of the data points. Note that a 100% population transfer is obtained after 212 μs.

trum is first measured by keeping the microwave frequency fixed and varying the RF frequency. In our case Δ is chosen to be 80 kHz (below the resonance frequency corresponding to the $|2,2\rangle \rightarrow |1,1\rangle$ transition) such that the population in the intermediate state is less than 1% of the total population. The offset field used is about 4 G. The RF resonance was observed at a frequency of 1.662 MHz (frequency generated by the Agilent waveform generator). Keeping the waveform generator at this value and providing maximum microwave (8 W) and RF (10 W) powers, the two photon Rabi oscillations were measured as shown in figure 4.12. The Rabi frequency was measured to be $2\pi \times (2.33 \pm 0.03)\,\mathrm{kHz}$.

However, in our case, this was not very robust as the pulse duration for maximum transfer to the $|1,0\rangle$ state varied on a daily basis. This could be due to varying stray magnetic fields or the pointing stability of the dipole trap lasers to which this process is probably more sensitive. The efficiency of the transfer was also not always 100%. One way to go about this, was to do an adiabatic transfer where the exact frequency and power of the pulse is not very important. Another method is to use two resonant pulses, a microwave and an RF one after the other. We chose to use the second method as this was easier to apply and turned out to be quite robust and

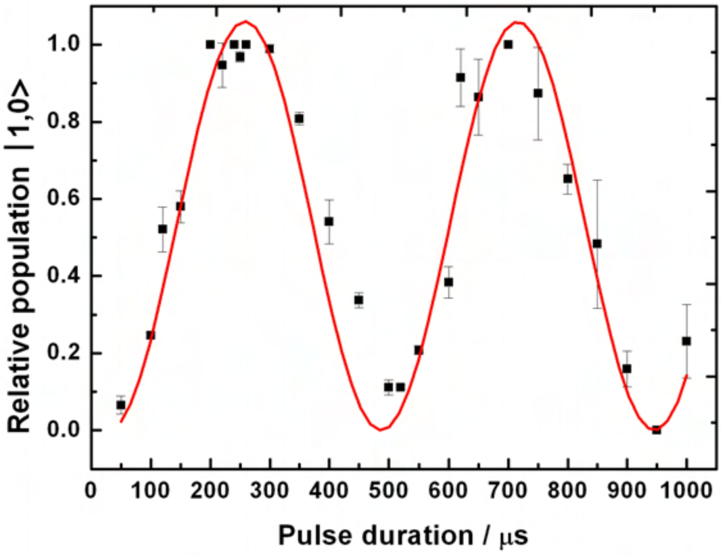

Figure 4.13: Rabi Flopping: The relative population of the atoms in the $|1,0\rangle$ state with respect to the total number of atoms in the $|1,1\rangle$ and $|1,0\rangle$ states versus the pulse duration is shown. The red curve is a sine squared fit to the data which gives the value of the Rabi frequency to be $2\pi \times (2.18 \pm 0.04)$ kHz. The error bars are the statistical error of the data points. Note that a 100% population transfer is obtained after 230 μs.

was also faster, a total time of about 250 μs for two resonant π pulses instead of a second required for an adiabatic transfer. This is discussed in the next part.

4.4.2 Transfer to the $|1,0\rangle$ State through a RF Pulse

In this method, two resonant π pulses are used to transfer the atoms from the $|2,2\rangle \rightarrow |1,0\rangle$ state. The atoms are first prepared in the $|1,1\rangle$ state through a resonant single photon microwave transition. This has already been explained in the previous section. After this, a second π pulse is applied, which is an RF pulse in this case. This resonant pulse transfers the atoms from the $|1,1\rangle \rightarrow |1,0\rangle$ state.

The setup used for the generation of the RF pulse is the same as that used for the two photon transition. However, here the offset field used is larger which is about 20 G. A smaller offset field of the order of 5 G led to a small linear splitting of the hyperfine states (anomalous Zeeman effect). Here, the two level atom criteria is not fulfilled due to the coupling of the RF to all the Zeeman states. At high powers (maximum power of 10 W), the large spectral width of the RF radiation led to the

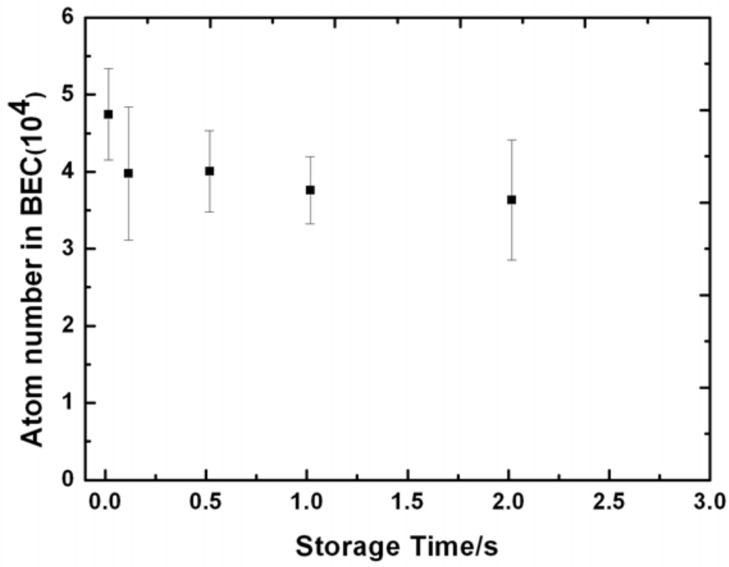

Figure 4.14: The number of atoms in the BEC in the $|1,0\rangle$ state is plotted against the storage time. The atoms have been stored for 2 s. A longer storage time was not possible. An exponential fit could therefore, not be fitted to the data points. Note that almost no losses are observed even after 2 s.

population of all the Zeeman split hyperfine states. At smaller powers, the strength of the field was not enough to couple out all the atoms from the $|1,1\rangle$ state. Hence, a higher magnetic field is applied such that the splitting is no longer linear. At a field strength of 20 G, the quadratic effect comes into play and the two levels viz. $|1,1\rangle$ and $|1,0\rangle$ are coherently coupled. The RF resonance frequency was measured and Rabi oscillations could be observed between the two states at resonance for maximum microwave and RF power. The Rabi oscillations are shown in figure 4.13. The Rabi frequency is measured to be $2\pi \times (2.18 \pm 0.04)$ kHz.

This method was quite robust and a 100% transfer was obtained at the application of a π pulse. This was therefore used to transfer the BEC from the $|2,2\rangle \rightarrow |1,0\rangle$ state.

4.4.3 Lifetime Measurement of a BEC in the $|1,0\rangle$ State

The lifetime of the BEC is important for all measurements concerned with Cs since the observation time for the interactions is of the order of 1 s in our case. This is the time required for the loading and observation of changes in the Cs MOT. This will be discussed in the next chapter. The lifetime of the BEC was measured by storing the condensate in the lowered trap (~1 W of power in each arm of the dipole trap, with a trap depth of $\sim 8\,\mu$K) after evaporation. Ideally, the trap should be ramped up for the lifetime measurement as a lowered trap leads to further cooling and a corresponding decrease in the atom number. However, in this case, it is immaterial as the cooling is minimal for the time duration within which the atoms are stored. Also, almost no losses are observed in the 2 s storage time. The condensate could not be stored longer due to technical limitations as the waveform generator responsible for controlling the power of the dipole trap has a limited storage memory. Nevertheless, since almost no losses are observed for a storage time of 2 s which is the time scale required for experimentation, a further storage is not inevitable. Figure 4.14 shows the lifetime measurement of the condensate. The data has not been fitted since there are not enough points to fit an exponential decay curve.

In this chapter, I have discussed the transport of the Rb cloud to the position of the Cs MOT in order to overlap these two entities. The preparation of the BEC or a thermal cloud in the magnetically insensitive states and the absolute ground state has also been shown. Since, the lifetimes are important for measurements between Rb and Cs, the lifetime measurement for a BEC in the $|1, 0\rangle$ state was done. This fulfils all the necessary conditions required to study the interactions between an ultracold Rb cloud in one of the $m_f = 0$ states and a single Cs atom in a MOT. This will be discussed in the next chapter.

5 Interaction of a Single Cs Atom in a MOT with an Ultracold Rb Cloud in the Dipole Trap

The interaction of a single Cs atom with an ultracold Rb cloud is a realization of the model system of the interaction between a few-body system and a many-body system. Such a model system opens the route for the investigations of many intriguing phenomena and the realization of many proposals, as discussed in the introduction to this thesis. This relatively new area of physics combining these two entities has been theoretically studied in various ways.

In our approach, a single Cs atom captured in a MOT is overlapped with an ultracold Rb cloud in a dipole trap and the interactions have been studied by analyzing the losses observed in Cs. Ideally, a species specific conservative trap for Cs (see chapter 6) will eventually be used where a spin polarized sample of Cs in the ground state can be prepared to study the coherent phenomena. Here, the interactions have been studied with Cs in a MOT. This allows studying the influence of one species over the other as well as developing certain methods for the analysis of the interspecies interactions. Cs has been used as a probe to study the interspecies inelastic collisional properties. These studies have been used to calculate the interspecies inelastic rate coefficients, which provide a useful insight into the nature of interactions between the two entities. Moreover, the method used here to determine the rate coefficients, by counting the loss rates, greatly simplifies the otherwise complicated differential equation used to determine such rates in mixtures with a large number of atoms.

5.1 Single Atom Cs MOT

The single atom Cs MOT has already been briefly described in section 3.3. The high magnetic field gradients, small beam sizes and a smaller MOT size is what differentiates this from a conventional MOT with a large number of atoms ($10^7 - 10^9$ atoms). A current of 25 A is passed through the MOT coils shown in figure 3.3 to produce a field gradient of 300 G/cm. The MOT beams have a radius of 1 mm with a total power of 1 mW divided among all the six beams. The cooling light is 6 MHz ($\sim 1.15\Gamma$) detuned from the cooling transition $f = 4 \rightarrow f' = 5$. The intensity of the

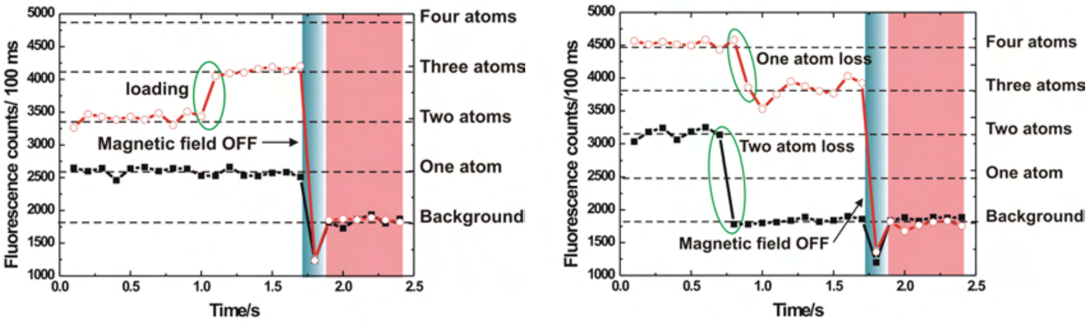

a) b)

Figure 5.1: Four typical traces of Cs MOT are shown as detected using the fluorescence detection system where the fluorescence counts are plotted against the time. The Cs MOT is first loaded using a low gradient followed by a ramping of the field gradient to 300 G/cm. The detection is done during the high gradient phase with a binning period of 100 ms. The MOT is ON for 1.7 s after which the repumper light and the magnetic field are switched OFF for 200 ms (denoted by the blue differentially shaded region). The repumper light is then switched ON after 200 ms for 500 ms to record the background (denoted by the pink shaded region). The dashed lines in the graphs represent one, two, three and four atoms as labelled. The left graph (labelled a)), shows a loading event (red trace with straight lines and hollow circles) after a time of 1 s and a trace with a single atom (black trace with straight lines and filled squares) without any losses. The graph on the right (labelled b)) shows two traces, one of which represents a one-atom loss after a period of 800 ms (red trace with straight lines and hollow circles) and the other represents a two-atom loss after a period of 700 ms (black trace with straight lines and filled squares).

light at the crossing point of all the lasers is $I_0 = P_{\mathrm{tot}}/\pi w_{\mathrm{b}}^2 = 31.85\,\mathrm{mW/cm^2}$, where P_{tot} is the total power of the beams and w_{b} is the radius of the MOT beam. The size of the single atom Cs MOT can be calculated using equations (3.1) and (3.3) where κ is given by

$$\kappa = \frac{\mu' A}{\hbar k}\beta \,. \tag{5.1}$$

Here, $k = 2\pi/\lambda$ is the wave number, A is the magnetic field gradient and $\mu' \equiv (g_{\mathrm{e}}m_{\mathrm{e}} - g_{\mathrm{g}}m_{\mathrm{g}})\,\mu_{\mathrm{B}}$ is the effective magnetic moment of the transition used, where $g_{\mathrm{g}} = 1/4$ and $g_{\mathrm{e}} = 2/5$ are the Landé factors of the ground and excited states respectively and m_{g} and m_{e}, the respective Zeeman states. Here, β is the damping coefficient and is given by equations (3.1) and (3.2) by writing equation (3.1) for an optical molasses as the sum of the forces in both the directions. The $1/e^2$ radius of the MOT, w_{Cs} can be written as [100]

$$k_{\mathrm{B}}T = \kappa w_{\mathrm{Cs}}^2 \,, \tag{5.2}$$

where T is the temperature of the MOT. Using equation (5.2), the $1/e$ radius of the Cs MOT was calculated to be $7.7\,\mu$m for a typical MOT temperature of $100\,\mu$K and averaging over all the relevant Zeeman states. The single atom Cs MOT is detected using a fluorescence detection set up already described in section 3.6. Figure 5.1 shows typical traces of a single atom MOT. Here, the loading and loss of atoms can be determined and counted individually. This is in contrast to systems with large number of atoms where an ensemble average is taken. The graphs show four typical events.

a): Neither a loading or loss occurs, the atom is not lost from the trap.

b): A loading event, where an atom is loaded, the rate at which this happens depends upon the magnetic field gradient of the MOT.

c): A one-atom loss event, where a single atom is lost from the trap. This occurs due to collisions with background gas and the rate is determined by the quality of the vacuum.

d): A two-atom loss event, where two atoms are lost from the trap. This is due to collisions between two atoms leading to a two-body loss. However, in a binning time of 100 ms (in our case), there is also a possibility of counting two one-atom loss events as a single two-atom loss event, which is less than 2% in this case.

5.2 Overlap of the Rb cloud with the Cs MOT

In order to study the interactions of the Cs atom in the MOT with that of the Rb cloud in the dipole trap, these two entities need to be spatially overlapped. In this context, the magnetic transport in conjunction with the dipole trap was discussed in the previous chapter where the Rb cloud is transported to the centre of the quadrupole trap, i.e. to the position of the Cs MOT. However, this was an approximate method and in order to study the interactions, an accurate overlap is required. This has been done in the following ways.

5.2.1 Overlap using Near Resonant Light

The position of the crossed dipole trap is determined using near resonant light along the dipole trap axis to push out atoms from the MOT. For this, the near resonant light is locked onto the cooling transition of the Cs MOT. This light is coupled into the fibers guiding the dipole trap light, therefore sharing the same spatial mode after the fiber. The light coupled out of the fiber is then superimposed to the Cs MOT by adjusting the dipole trap alignment mirrors resulting in the destruction of the MOT.

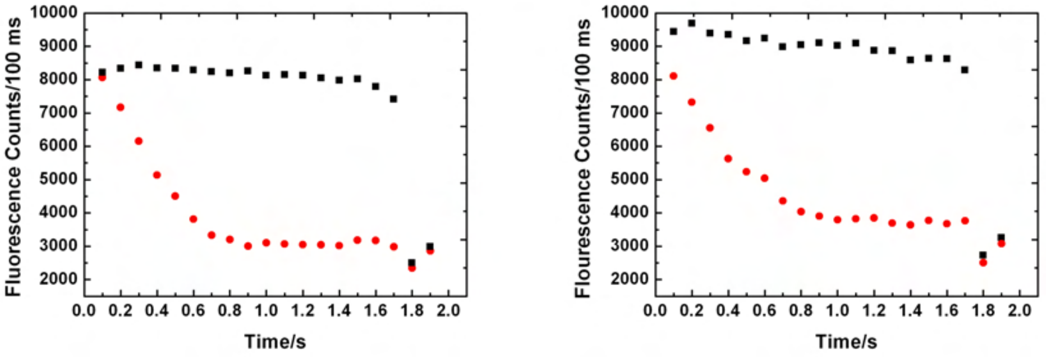

Figure 5.2: Overlapping the Rb cloud with the Cs MOT: In the graphs, the fluorescence counts of Cs is plotted in the presence and absence of Rb. The two graphs represent the optimization of the losses using the radial dipole trap beam mirrors for both degrees of freedom of the mirrors. The black squares represent the fluorescence counts without Rb and the red dots that with Rb. Cs losses are observed in each individual trace. Each point is the average of the fluorescence counts over the number of traces for a particular time. The binning time is 100 ms. The red dots represent the maximum losses in the shortest time possible for the optimal mirror position. A similar optimization technique is followed for the axial beam of the dipole trap.

This process is repeated several times by a subsequent reduction in the power of the near resonant light, in order to obtain a good overlap of this light with the centre of the MOT.

Since, the dipole trap beam and the near resonant light are coupled out of the same fiber and pass through the same set of optics before they enter the glass cell, this method yields a reasonably good overlap of the crossed dipole trap with that of the Cs MOT. The difference in optical paths due to a difference in the wavelengths (852 nm for the near resonant light and 1064 nm for the dipole trap) is negligible.

5.2.2 Overlap using the Ultracold Rb Cloud

Once, the crossed dipole trap is overlapped with the centre of the Cs MOT, the overlap is optimized using the Rb cloud. This can be done because Rb-Cs interactions lead to losses from the Cs MOT. This was first tried with the Rb BEC prepared in the $|1, 0\rangle$ state but no Cs losses were observed. This is because a BEC has a small spatial extent (see chapter 1) and hence, the overlap needs to be very accurate to observe losses. Therefore, an ultracold cloud of Rb at a temperature of ~ 600 nK was used, which has a larger spatial extent of about 25 μm. Losses were observed in Cs in the presence of this cold dense cloud of Rb in the dipole trap. The alignment was once again done using the dipole trap beam mirrors (both axial and radial) and the mirror positions were optimized for maximum losses observed in Cs in the shortest time (steepest losses). Figure 5.2 shows the maximization of losses by optimizing the mirrors of the radial arm of the dipole trap. In the graph, each point represents an average of the fluorescence counts over the number of traces for a particular time. The reduction in the fluorescence signal in the presence of Rb is evident from the graph. A similar optimization procedure is followed for the axial arm of the dipole trap. The change in the mirror positions do not drastically change the loading efficiency of the dipole trap. Small changes in the atom number or temperature of the Rb cloud are compensated by changing the gradient produced by the levitation coil during the loading of the dipole trap.

Once, the overlap is obtained, the interactions can now be studied quantitatively. This is shown in the next section.

5.3 Interaction of the Ultracold Rb Cloud with a Single or a Few Cs Atoms

The interaction between the Rb cloud and the Cs MOT leads to losses in the Cs atoms as already mentioned in the previous section and has been used to overlap these two entities. Beyond the plain observation of Cs losses in the presence of Rb, the nature and statistics of these loss events allow us to extract information on the underlying interaction processes. Here, our ability to identify and count individual loss events helps in determining various contributions to the loss rates independently. An analysis of these losses is discussed in this section.

5.3.1 Experimental Sequence

The Rb atoms are evaporated in the dipole trap to a temperature of $\sim 600\,\mathrm{nK}$ and then prepared in the $m_{\mathrm{f}} = 0$ state. These atoms are then stored in the trap for over 2 s. The Cs MOT is switched ON during this period by switching ON the magnetic field gradient and the Cs molasses. The observation time of the interactions is 1.7 s during which the Cs atoms are detected using the fluorescence detection technique. A TOF measurement is performed directly after this to determine the Rb atom number and temperature. The losses in the Cs MOT are studied by varying the Rb atom number. The Rb atom number is varied by loading less atoms in the Rb MOT in the beginning of the sequence. Therefore, the density of the cloud which scales linearly with the atom number changes proportional to the atom number, as the trap parameters remain unchanged. The Rb atoms are prepared both in the $|1,0\rangle$ state as well as in the $|2,0\rangle$ states for two independent measurements with the Cs MOT. The Rb atom number is taken to be constant during the short observation time of less than 2 s. This is evident in the $|1,0\rangle$ state from the lifetime measurement conducted (see figure 4.14). In the $|2,0\rangle$ state, the loss of atoms was calculated to be just about 5% during the observation time. The calculation was performed using the two-body loss rate coefficient of $8.8\times10^{-14}\,\mathrm{cm}^3/\mathrm{s}$ measured in [137]. This 5% loss was neglected and the atom number was assumed to be constant. Here, the three-body losses were neglected since the losses were two orders of magnitude smaller than the two-body losses.

5.3.2 Cs Dynamics

The dynamics of the Cs MOT is used to determine the interspecies inelastic rate coefficients. As already explained in chapter 1, the inelastic rate coefficients can be determined using the rate equation given in equation (1.18). For systems involving large number of atoms, the rate coefficients are determined by solving this differential equation. Equation (1.18) represents the rate equation for a homonuclear species. In our case, due to the involvement of two species, the rate equation for Cs can be written as

$$\begin{aligned}\frac{dN_{\mathrm{Cs}}}{dt} &= R_{\mathrm{L}} - L_1 \int n_{\mathrm{Cs}}\, d^3r - L_{\text{Cs-Rb}} \int n_{\mathrm{Cs}} n_{\mathrm{Rb}}\, d^3r - L_{\text{Cs-Rb-Rb}} \int n_{\mathrm{Cs}} n_{\mathrm{Rb}}^2\, d^3r \\ &\quad - L_2 \int n_{\mathrm{Cs}}^2\, d^3r - L_{\text{Cs-Cs-Rb}} \int n_{\mathrm{Cs}}^2 n_{\mathrm{Rb}}\, d^3r - L_3 \int n_{\mathrm{Cs}}^3\, d^3r \ , \qquad (5.3)\end{aligned}$$

where R_{L} is the loading rate of the Cs MOT, L_1 is the one-body loss rate due to collisions with the background gas, L_2 is the two-body loss rate due to collisions between two Cs atoms, $L_{\text{Cs-Rb}}$ is the two-body loss rate due to collisions between one Cs and one Rb atom, $L_{\text{Cs-Rb-Rb}}$ is the three-body loss rate due to collisions between two Rb atoms and one Cs atom, $L_{\text{Cs-Cs-Rb}}$ is the three-body loss rate due to collisions between two Cs atoms and one Rb atom and L_3 is the three-body loss rate due to collisions between three Cs atoms. Here, n_{Cs} and n_{Rb} are the Cs and Rb densities respectively and are given by

$$n_{\mathrm{Cs}} = \frac{N_{\mathrm{Cs}}}{\pi^{3/2} w_{\mathrm{Cs}}^3} e^{-r^2/w_{\mathrm{Cs}}^2} \ , \qquad (5.4)$$

$$n_{\mathrm{Rb}} = \frac{N_{\mathrm{Rb}}}{\pi^{3/2} w_1 w_2 w_3} e^{-x^2/w_1^2} e^{-y^2/w_2^2} e^{-z^2/w_3^2} \ . \qquad (5.5)$$

In equation (5.4), N_{Cs} is the Cs atom number and w_{Cs} is the $1/e$ radius of the Cs MOT and has already been determined using equations (5.1) and (5.2). In equation (5.5), N_{Rb} is the Rb atom number and w_1, w_2 and w_3 are the radii of the thermal cloud and are determined using the temperature of the cloud and the trap frequencies using equations (1.38), (3.25) and (3.26).

In our case, due to the high field gradient of the MOT, the loading events are rare and since the initial number of Cs atoms in the MOT is larger than two, the loss rate

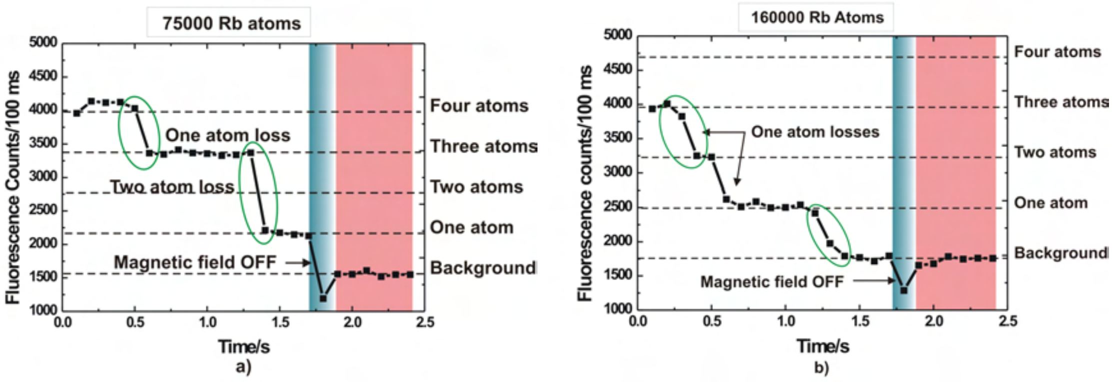

Figure 5.3: Cs Losses in the presence of Rb: The Cs one- and two-atom loss events are shown in the presence of Rb. The detection of the interactions is made for a time of 1.7 s. The magnetic field and the repumper light are then switched OFF for 200 ms (denoted by the blue differentially shaded region) after which the repumper light is switched ON again for 500 ms (denoted by the pink shaded region) to note the background. The left graph (labelled a)) shows one- and two-atom loss events in the presence of about 75000 atoms of Rb. The right graph (labelled b)) shows one-atom loss events in the presence of about 160000 atoms of Rb. As is evident from the graph, the loss rates are higher for larger Rb atom numbers.

is higher than the loading rate. Hence, the system is never in steady state. The LHS in equation (5.3), dN_{Cs}/dt, is therefore, not equal to zero. This makes the solution of an already complicated differential equation more cumbersome and the equation cannot be solved analytically.

To go about this problem, another procedure has been implemented here, to determine the various rate constants. This takes advantage of the fact that the one-atom, two-atom and three-atom loss events can be counted in the case of the Cs MOT. Figure 5.3 shows the one and two atoms loss events in Cs in the presence of different Rb atom numbers. Using this, the individual terms in the differential equation (5.3) have been solved independently to obtain the rate coefficients. As already mentioned, this has been done independently for Rb atoms in the $|1,0\rangle$ as well as the $|2,0\rangle$ states. First the Rb atoms in the $|1,0\rangle$ state is considered.

Cs Atom Losses in the Presence of Rb in the $|1,0\rangle$ State

The Rb atoms are prepared in the $|1,0\rangle$ state using a microwave π pulse followed by a RF π pulse as explained in section 4.4.2. The Cs atom losses are first segregated into one-atom, two-atom and three-atom loss events for different Cs atom numbers without the Rb atoms. The three-body loss events in the absence of Rb is very small (two orders of magnitude smaller than the one-atom loss rate) and therefore the last term in the rate equation (5.3) can be neglected. The one- and two-body loss events are analyzed in the presence of Rb for different Rb atom numbers.

One Cs Atom Loss Events

The loss of a single Cs atom in the presence of Rb could be due to three processes.

a) Background gas collisions : This is the second term in the rate equation (5.3).

b) Two-body loss : This is due to collision with a single Rb atom and is represented by the third term in the rate equation (5.3).

c) Three-body loss : This is due to collisions with two Rb atoms and is given by the fourth term in the rate equation (5.3).

Figure 5.4 shows the one-atom loss rate (number of single atom loss events/s) varying with the Rb atom number. Three different measurements have been done for three different Cs atom numbers viz. $N_{\text{Cs}} = 1, 2, 3$. In order to determine the contributions of the various terms in the rate equation a parabola of the form

$$A_{\text{N}} + N_{\text{Cs}} B_{\text{N}} N_{\text{Rb}} + N_{\text{Cs}} C_{\text{N}} N_{\text{Rb}}^2 \,, \tag{5.6}$$

has been fitted to the data to check the linear and quadratic dependence of the loss rates on the Rb atom number. Here N_{Rb} represents the Rb atom number. The first term, A_{N}, is the constant term independent of the Rb atom number and is therefore, the contribution to the losses due to background gas collisions. This has been kept constant during the fit with a value which has been determined independently via another measurement to be (0.03 ± 0.01)/s [55]. The coefficients B_{N} and C_{N} of the second and the third terms of the fit function respectively, are used to determine $L_{\text{Cs-Rb}}$ and $L_{\text{Cs-Rb-Rb}}$ respectively by comparing the fit function with the rate equation since the third term has a linear dependence on the Rb atom number and the fourth term has a quadratic dependence on the Rb atom number. The loss rates were calculated using the Cs and Rb densities given in equations (5.4) and (5.5) respectively. The size of the Cs MOT has already been calculated in section 5.1. The Rb cloud size of about 25 μm is calculated using the trap frequencies $\omega_x = 2\pi \times 187\,\text{Hz}$, $\omega_y = 2\pi \times 66\,\text{Hz}$ and $\omega_z = 2\pi \times 132\,\text{Hz}$ at a temperature of 600 nK. The loss rates obtained from the fits are displayed in table 5.1.

Two Cs Atom Loss Events

The loss of two Cs atoms in the presence of Rb could be due to the following processes

a) Two-body loss : This is due to collisions between two Cs atoms and is independent of the Rb atom number. This is represented by the fifth term in the rate

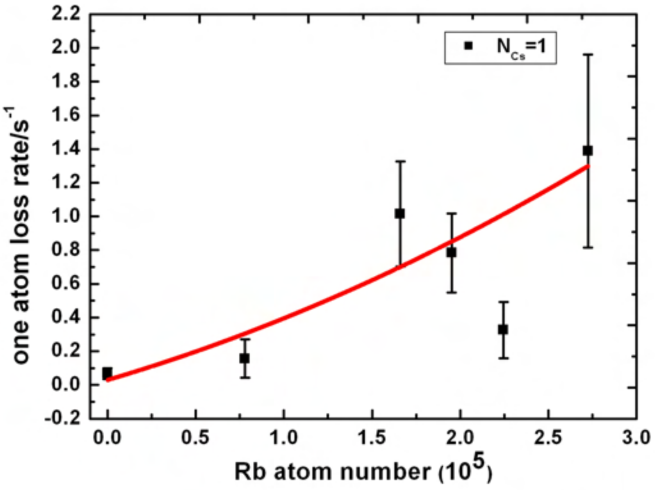

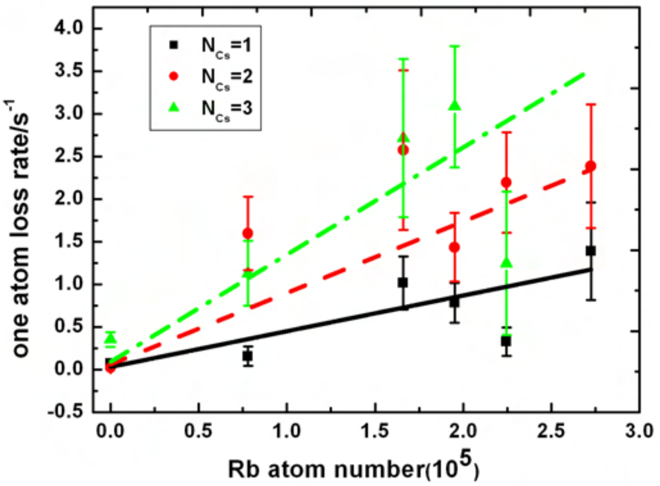

Figure 5.4: The Cs one-atom loss rate is plotted against the Rb atom number in the $|1,0\rangle$ state. The upper graph shows the loss rate for a constant Cs atom number of 1 ($N_{\mathrm{Cs}}=1$). The lower graph shows three data sets corresponding to $N_{\mathrm{Cs}}=1$ (black squares), $N_{\mathrm{Cs}}=2$ (red dots) and $N_{\mathrm{Cs}}=3$ (green triangles). The data sets have been fitted simultaneously to obtain common fit parameters for all the three data sets. The fitting function used in both the cases is the one given in equation (5.6). The errors have been computed assuming a normal distribution. This is because, the loss rates follow a continuous distribution over the time. The fits (black straight, red dashed and green dash-dot curves) are weighted with the errors.

equation (5.3).

b) Three-body loss : This is due to collisions between two Cs atoms and one Rb atom and is represented by the sixth term in the rate equation (5.3).

However, in our case, for a binning time of 100 ms, the possibility of counting two one-atom loss events as a single two-atom loss event is not negligible. Hence, the one- and two-atom loss rates are corrected taking the two one-atom loss events within 100 ms into consideration. About 50-100% (depending upon the Rb atom number) of the two-atom loss events were found to be two one-atom loss events. The resulting remaining two-atom loss rates turned out to vary randomly with the Rb atom number. Hence, the dependence of the two-atom loss rate on the Rb atom number could not be ascertained. A better analysis of the two-atom loss rates could be made by using a smaller binning time of say, 10 ms. This would give a better resolution and the actual two-atom loss rates can be determined experimentally. The two-atom loss rate in the absence of Rb could however be measured. This was done for two different Cs atom numbers viz. $N_{\text{Cs}} = 2, 3$ and was used to calculate the two-body loss rate coefficient L_2 due to collisions between two Cs atoms.

The results of all contributions to the loss processes in the presence of Rb in the $|1, 0\rangle$ state are displayed in table 5.1 giving an insight into the nature of the interactions between the two entities. A similar measurement and analysis has been done in the presence of Rb in the $|2, 0\rangle$ state. This is discussed below.

Cs Atom Losses in the Presence of Rb in the $|2, 0\rangle$ State

The Rb atoms are prepared in the $|2, 0\rangle$ state using two microwave π pulses one after the other as explained in section 4.4. For the analysis, an exact procedure is followed for the Rb atoms in the $|2, 0\rangle$ state. One- and two-atom loss rate measurements are made for three different Cs atom numbers ($N_{\text{Cs}} = 1, 2, 3$). Figure 5.5 shows the one-atom loss rates fitted with the fit function given in equation (5.6) in order to determine the loss rate coefficients as in the case of the atoms in the $|1, 0\rangle$ state. Here again the two-atom loss rate does not show an expected linear dependence on the Rb atom number.

The various rate coefficients determined from the fit to the data are shown in table 5.1 for Rb in the $|2, 0\rangle$ state.

5.3.3 Interpretation of the Results

There are no direct literature values available to compare the interspecies inelastic loss rate coefficients with one of the species in a MOT and the other in a conservative potential. The homonuclear loss rates have been determined for Rb as well as Cs in a conventional MOT with a large number of atoms as well as in a conservative potential. Some of the references are given in table 1.1. However, a comparison can

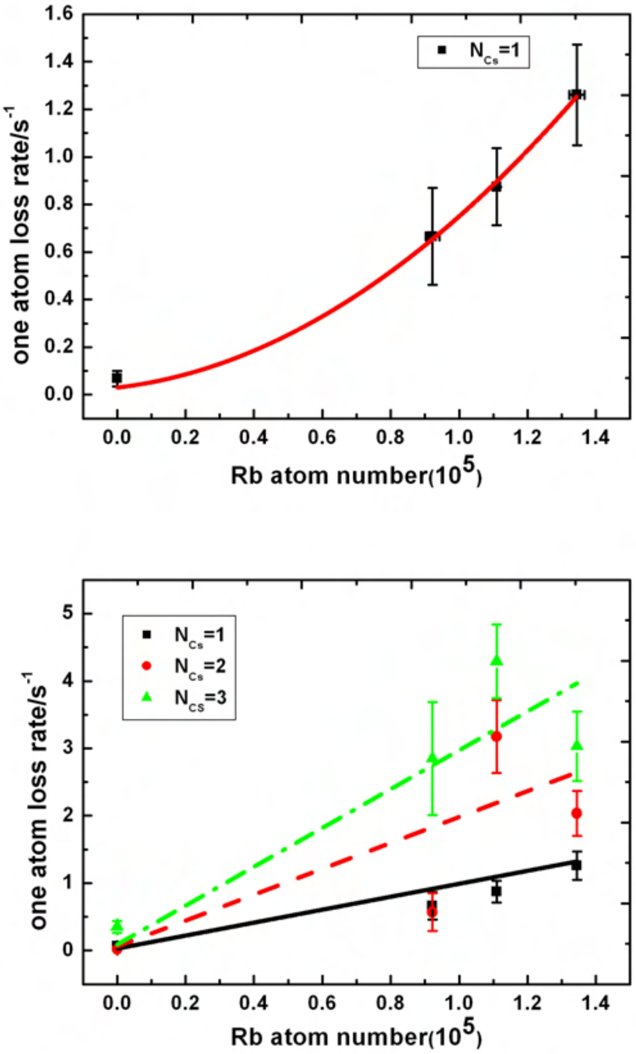

Figure 5.5: The Cs one-atom loss rate is plotted against the Rb atom number in the $|2,0\rangle$ state. The upper graph shows the loss rate for a constant Cs atom number of 1 ($N_{\mathrm{Cs}} = 1$). The lower graph shows three data sets corresponding to $N_{\mathrm{Cs}} = 1$ (black squares), $N_{\mathrm{Cs}} = 2$ (red dots) and $N_{\mathrm{Cs}} = 3$ (green triangles). The data sets have been fitted simultaneously to obtain common fit parameters for all the three data sets. The fitting function used in both the cases is the one given in equation (5.6). The errors have been computed assuming a normal distribution. This is because, the loss rates follow a continuous distribution over the time. The fits (black straight, red dashed and green dash-dot curves) are weighted with the errors.

be made between the two-body light-induced homonuclear loss rate in Cs obtained here with that obtained in [74].

		One atom loss		Two atom loss
State	N_{Cs}	$L_{\text{Cs-Rb}}$	$L_{\text{Cs-Rb-Rb}}$	$L_{\text{Cs-Cs}}$
No Rb	2			$(4 \pm 3) \times 10^{-9}\,\text{cm}^3/\text{s}$
	3			$(8 \pm 7) \times 10^{-10}\,\text{cm}^3/\text{s}$
$\|1, 0\rangle$	1	$\sim 10^{-13}\,\text{cm}^3/\text{s}$	$\sim 10^{-26}\,\text{cm}^6/\text{s}$	
	Common Fit	$(9 \pm 0.9) \times 10^{-13}\,\text{cm}^3/\text{s}$		
$\|2, 0\rangle$	1	$(4 \pm 2) \times 10^{-13}\,\text{cm}^3/\text{s}$	$(2.7 \pm 0.3) \times 10^{-25}\,\text{cm}^6/\text{s}$	
	Common Fit	$(2 \pm 0.2) \times 10^{-12}\,\text{cm}^3/\text{s}$		

Table 5.1: Interspecies inelastic rate coefficients: The interspecies inelastic rate coefficients calculated from the measured one and two atom Cs loss rates are shown. The Cs-Cs two body loss rate is determined for $N_{\text{Cs}} = 2, 3$. The Cs-Rb and Cs-Rb-Rb loss rates are determined for Rb atoms in the $|1, 0\rangle$ as well as the $|2, 0\rangle$ states for $N_{\text{Cs}} = 1$ separately and simultaneously fitting the rates obtained for $N_{\text{Cs}} = 1, 2, 3$ (referred to as Common Fit in the table). As can be seen from the values in the table, the loss rates obtained for $N_{\text{Cs}} = 1$ and from the common fit do not agree with each other. This is attributed to the uncertainty in the fit parameters due to poorer statistics for $N_{\text{Cs}} = 2, 3$. The grey shaded regions represent cells where no values are expected (Not Applicable).

The two-body loss rates obtained due to collisions between two Cs atoms in our experiment lie in the range $L_2 \sim 10^{-10} - 10^{-9}\,\text{cm}^3/\text{s}$. These losses are attributed to all the three collisional loss mechanisms in a MOT viz. light-induced (radiative escape and fine structure changing collisions) and ground state collisions (hyperfine changing collisions). The rates in our high gradient MOT are higher than that in a conventional MOT ($10^{-12} - 10^{-10}\,\text{cm}^3/\text{s}$) due to an effective reduction in the trap depth at a large field gradient (300 G/cm in our case) because of a reduction in the recapture ability, resulting in more losses from the trap. The Cs MOT in our case has a saturation parameter $s_0 = I_0/I_\text{s} = 29$ where I_s is the saturation intensity. The effective saturation parameter is then given by $s = s_0/\left[1 + \left(\frac{2\Delta}{\Gamma}\right)^2\right] = 1.84$. For this saturation parameter, the light-induced two-body loss rate in [74] is $\sim 2 \times 10^{-10}\text{cm}^3/\text{s}$. Our rates are larger than this. However, since the loss rates in a MOT depend

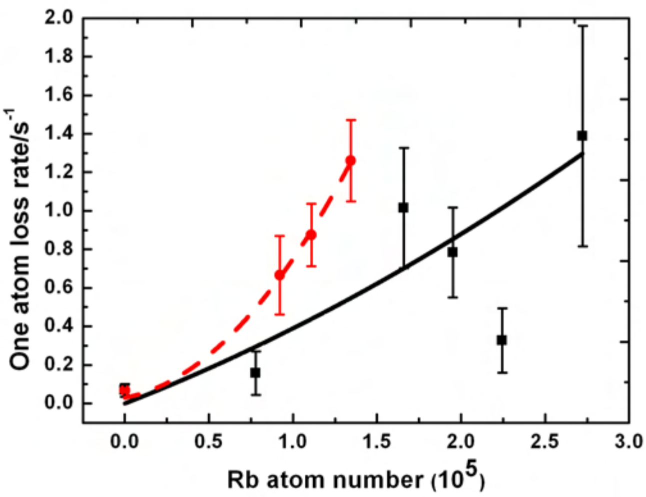

Figure 5.6: The Cs one-atom loss rate is plotted for $N_{\mathrm{Cs}} = 1$ in the presence of Rb in the $|1,0\rangle$ state (black squares) and $|2,0\rangle$ state (red dots) with their respective fits (black straight lines and red dashes lines). The stronger curvature of the fit for Rb in the $|2,0\rangle$ state indicates a higher quadratic dependence of the loss rate on the Rb atom number. The quadratic dependence is due to the loss rate $L_{\text{Cs-Rb-Rb}}$ as already mentioned before and this is an indication of a higher $L_{\text{Cs-Rb-Rb}}$ value in the presence of Rb in the $|2,0\rangle$ state.

strongly on the detuning, intensity and the trap depth, all of which are not the same for the two experiments, an exact comparison cannot be made and it is quite possible that the trap and beam parameters in our case lead to larger losses.

The two-body loss rate $L_{\text{Cs-Rb}}$ lies in the range $10^{-12} - 10^{-13}\,\mathrm{cm}^3/\mathrm{s}$. This value lies between the heteronuclear (Rb-Cs) loss rate obtained for Cs in a high gradient MOT (order of $10^{-10}\,\mathrm{cm}^3/\mathrm{s}$) and the homonuclear loss rate for Rb in a conservative trap (order of $10^{-14}\,\mathrm{cm}^3/\mathrm{s}$). The heteronuclear loss rate in the MOT is due to light of two wavelengths viz. 780 nm and 852 nm. In the conservative trap, light is absent and therefore, the collisions are not light-induced. In our case, light of only one wavelength viz. 852 nm is present. Since the dominant loss mechanism is still light-induced due to the presence of Cs light (852 nm), our value lies in between these two known values.

The three-body loss rate $L_{\text{Cs-Rb-Rb}}$ is $\sim 10^{-26}\mathrm{cm}^6/\mathrm{s}$ in the $|1,0\rangle$ state and $\sim 10^{-25}\mathrm{cm}^6/\mathrm{s}$ in the $|2,0\rangle$ state. The loss rate obtained for Rb in the $|1,0\rangle$ state is one order of magnitude lower than that in the $|2,0\rangle$ state. In figure 5.6, the one atom loss rates for $N_{\mathrm{Cs}} = 1$ has been plotted for both Rb in the $|1,0\rangle$ as well as the $|2,0\rangle$ states to graphically illustrate this difference. The difference in the loss rates can be attributed to the larger number of loss channels present for the atoms in the $|2,0\rangle$ state than in the $|1,0\rangle$ state. This means that despite the large loss rates of light-induced collisions, the number of loss channels in $f = 2$ seem to contribute significantly to the loss rates. However, the errors obtained in the loss rate coefficient values of the $|1,0\rangle$ state are too large to really come to any conclusions on this.

The method described in this section, is quite useful in determining the interspecies interactions of a many-body system with a few-body system quantitatively. The results obtained are meaningful but the accuracy is limited due to poor statistics. This is because of the long experimental cycle time of the order of a minute. Such long cycles are inevitable in our case due to the production of a BEC. However, the traces involving single Cs atoms require a large number of experimental runs because the statistics is based on a time average rather than an ensemble average. Since, the number of experimental runs that can be performed in a day is limited due to the cycle time of a minute, the number of data points obtained are inadequate for a good statistical analysis. A better data with more statistics would help in determining the rate coefficients with a much better accuracy. For this, however, changes need to be made for a faster experimental cycle.

The interactions between the two entities have been studied by observation of losses in the few-body system (Cs MOT). No changes were observed in the Rb cloud within the accuracy of your imaging technique. Hence, the method is non-destructive as far as the many-body system is concerned.

5.3.4 Possible Improvements in Statistical Analysis

The method used in the analysis of the loss rates in this thesis is based on the assumption of a normal distribution. Using this, the mean value and the corresponding errors have been calculated. This method works perfectly for a large number of loss events or for large statistics. However, the number of loss events in this analysis is not very large and hence a method based on e.g. Bayes statistics can possibly give a more accurate result. Bayes statistics is based on the relation between the conditional probabilities of the measured data and the hypothesis [138] and works quite well for a small data sample. The Bayes formula is written as

$$P(H|D) = \frac{P(D|H)P(H)}{P(D)}\ , \tag{5.7}$$

where $P(H|D)$ is the conditional probability of H given D is true, $P(D|H)$ is the conditional probability of D given H is true and $P(H)$ and $P(D)$ are the independent probabilities of H and D, respectively. Suppose, H represents the hypothesis and D the data. The relevance of this formula or method is that it confirms the truth of a prior hypothesis based on the conditional probability that the data is true. In [43], the number of atoms in a particular hyperfine level is determined by analyzing the fluorescence signals using the Bayesian statistics. Here, the state of the atom could

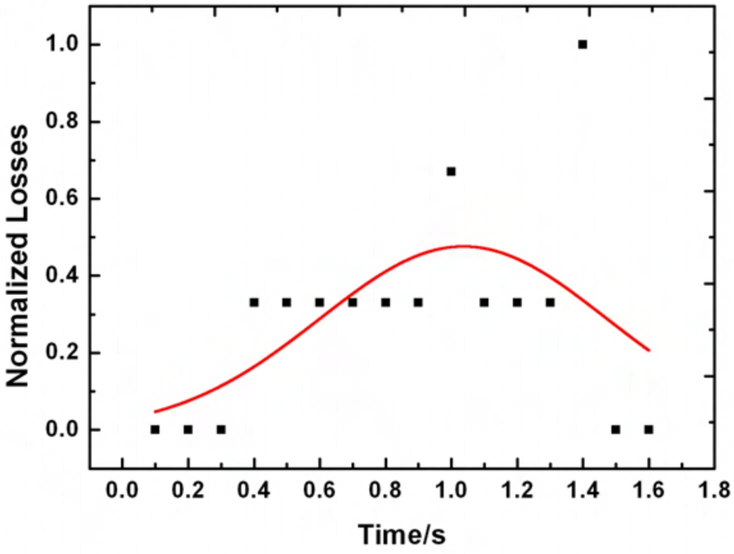

Figure 5.7: The graph shows the normalized losses plotted against the dwell time of the Cs atoms in the trap. The red curve is a Gauss fit to the data points. The centre of the Gauss fit gives the most probable dwell time and is in agreement with the statistical mean value.

be determined despite the fact that the signal to noise ratio of the fluorescence signal was extremely low. Figure 5.7 shows the plot of the normalized losses against the dwell time of the atoms (for $N_{\mathrm{Cs}} = 1$) in the trap for a particular Rb atom number in our experiment. The losses were determined by counting the steps in the fluorescence signal where the steps can be clearly differentiated. A Gauss is fitted to the data to determine the most probable dwell time. This is in agreement with the mean calculated from the loss rates within the accuracy of the fit. Small discrepancies are due to the fact that the observation time of the interactions (1.7 s) is smaller than the lifetime of the Cs atoms. For an exact concurrence, the observation time should be much larger than the lifetime. For the Gaussian fit, the values converge with that of the mean since this has been done for an individual loss rate for a particular Rb atom number.

However, for a more accurate result, the loss rates need to be calculated taking into account the dependence on the Rb atom number. To calculate the loss rates, a model based on the rate equations is used in the Bayes analysis. Since, in our case, the loss rates exhibit a dependence on the Rb atom number, this needs to be incorporated into the model as well. The Bayes algorithm should then be modified to provide solutions to this model. This will presumably be incorporated for the analysis of ground state collisions between a Cs atom and a Rb BEC in the future.

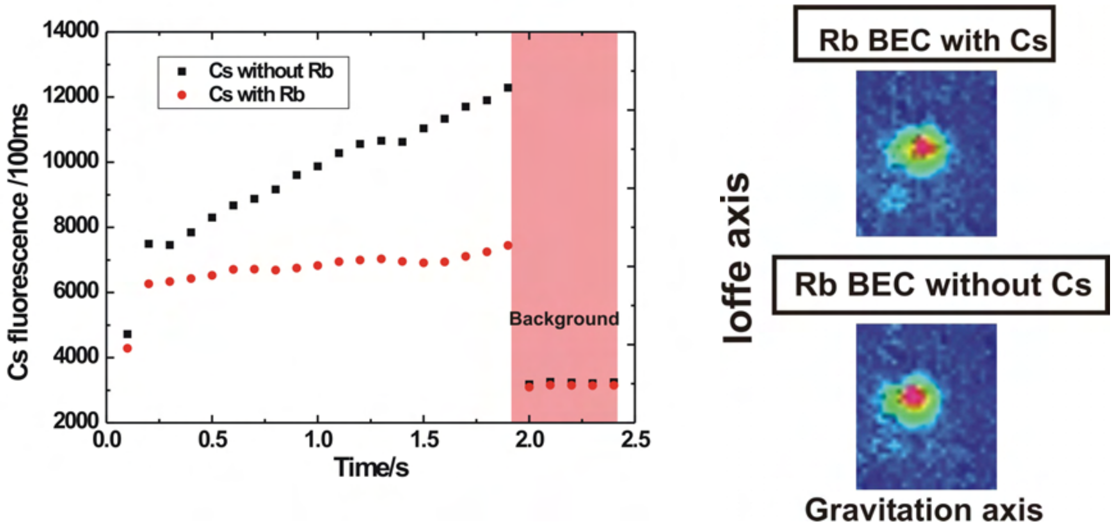

Figure 5.8: Cs Losses in the presence of Rb BEC: In the graph, the fluorescence counts are plotted against the time. The binning time is 100 ms. Each point represents the average of the fluorescence counts over the number of traces (22 in this case) recorded for a particular time. The black squares are the data points for Cs without Rb and the red dots for Cs in the presence of Rb. The Cs MOT has a gradient of 200 G/cm. Cs losses are observed in the presence of the Rb BEC in each individual trace. In the graph, the average of these traces is plotted. The large difference in the fluorescence counts in the absence and presence of Rb is evident from the graph. An increase in the fluorescence counts with time is due to the higher loading rates at lower field gradients. The interactions are observed for a time of 2 s. In the last 500 ms the background is recorded by switching OFF the magnetic fields and leaving the MOT lasers ON (denoted by the pink shaded region). The pictures on the right are the absorption images of the Rb BEC in the presence and absence of Cs atoms. As is evident from these images, the Rb BEC remains unaffected by Cs within the accuracy of our imaging technique.

5.4 Interaction of the Rb BEC with a Few Cs Atoms

An interesting experiment is to check for changes in a BEC e.g. heating or destruction of a BEC in the presence of single Cs atoms by inducing dissipation in a BEC or the possibility of a controlled adjustable coupling of these single atoms to a BEC.

The Rb BEC was prepared in the $|1, 0\rangle$ state. The Cs MOT was then switched ON for 2 s with a field gradient of 200 G/cm and the interactions were observed. A lower gradient was taken compared to the previous measurements in order to load comparatively larger number of Cs atoms (4-10) in order to check for any kind of heating or excitations in the BEC. The BEC however, remained unaffected within the accuracy of our imaging technique. Cs atom losses were observed. Figure 5.8 shows the fluorescence signal of Cs in the presence and absence of the Rb BEC. The points plotted in the graph are the average of the fluorescence counts over the number of traces recorded for a particular time. Each individual trace shows loss events. The increase in the fluorescence signal in the absence of Rb is due to the higher loading rate at a smaller field gradient.

The Cs MOT has a typical temperature of about 100 μK whereas the trap depth of the lowered dipole trap is about 8 μK. The high energy atoms from the Cs MOT knock out atoms from the BEC instantaneously. This indicates the need for a conservative trap for Cs to get rid of light-induced collisions, to see the effect of Cs on the condensate. A complete transfer of the energy of a Cs atom to the Rb BEC can lead to an increase in the condensate temperature or a loss of atoms resulting in the destruction of the condensate.

6 Summary and Outlook

In this thesis, I have discussed the interactions between an ultracold Rb cloud in a dipole trap, which represents a many-body system and a single or few Cs atoms in a MOT. These studies have been carried out to understand the nature of influence of one system over the other and for the development of various methods and techniques required for interesting experiments between a Rb BEC and a spin polarized single Cs atom. The technical aspects of overlapping the two entities and the coherent manipulation of the atomic states of Rb with a microwave and a RF radiation are discussed. The method used to study the interactions between Rb and Cs is simple and elegant and can be used for future experiments of the unbalanced mixture.

A pre-cooled cloud of Rb is prepared in the QUIC trap. The overlapping of the two entities (Rb and Cs) which are 7 mm apart from each other (since, Cs is in a MOT) is achieved by the method of magnetic transport along with the optical dipole trap. The Rb cloud is transported to the position of the MOT . The transport has a good efficiency with negligible atom losses and negligible heating. The Rb atoms are loaded into a crossed dipole trap and cooled evaporatively to quantum degeneracy with $\sim 10^5$ atoms in the condensate. The Rb BEC in the dipole trap is prepared in the $|1, 0\rangle$ state using a microwave and a RF radiation. A cold thermal cloud of Rb is also prepared in the $|2, 0\rangle$ state. The $m_f = 0$ states have been used for experiments with Cs since, they are insensitive to the high field gradient (300 G/cm) of the Cs MOT. The Rb BEC is also prepared in the absolute ground state which is required for all future experiments with spin polarized Cs atoms. Finally, the interactions between the two entities are studied in the form of losses in Cs atoms in the presence of a 600 nK cloud of Rb. The method used to study these interactions relies on the determination of the loss rates by counting the individual one- and two-body losses in Cs. Their variation with the Rb atom number is analysed, to determine individually the various interspecies inelastic loss rate coefficients. This greatly simplifies the problem of solving the complicated rate equation which is employed to determine the loss rate coefficients for systems with large number of atoms. This method can therefore, also be used for the future experiments.

6.1 Outlook

Experiments and methods presented in this thesis are the initial steps towards studying the interactions of a many-body system and a few-body system. The Rb atoms are in a conservative potential but Cs is trapped in a MOT, where a spin polarized sample of Cs cannot be prepared since Cs occupies all the Zeeman split hyperfine states. Moreover, the rate of light-induced Rb-Cs inelastic collisions is very high ($\sim 10^{-10}\,\mathrm{cm}^3/\mathrm{s}$ for the two-body loss rate [74]) in this dissipative potential due to a high photon scattering rate of $\sim 13\,\mathrm{MHz}$ leading to trap loss and heating. Also, in order to tune the interactions between the two species, e.g via interspecies Feshbach resonances, the magnetic field needs to be used as an independent parameter which is not possible due to the magnetic trapping potential of the single atom MOT. Hence, Cs needs to be trapped in a conservative potential.

6.1.1 Species Selective Optical Lattice for Cs

We plan to use a species selective optical lattice to trap and store the single Cs atoms. The lattice would be loaded from the high gradient Cs MOT. An optical lattice is formed by two counter-propagating laser beams which interfere to create a standing wave periodic potential where the atoms are stored in the nodes or antinodes depending upon the sign of the detuning of the laser beams with respect to the atomic transition. If only one pair of counter-propagating light beams interfere, then it is a 1D optical lattice. An optical lattice provides a tight confinement in space which is required for a good spatial overlap with the condensate which has a size of a few μm (see section 1.3). Moreover, a species selective trap allows the manipulation of either species independent of each other e.g. moving the Cs atom independently with respect to the Rb condensate.

Two forms of species selective optical lattices are discussed in [139] which takes advantage of the dependence of the potential shift on the wavelength of the atomic species and the fine structure splitting of the atom which forms the doublet lines D_1 and D_2. The so called "tune in" and "tune out" schemes discussed in [139] are used to choose the wavelength of the trapping light in such a way that the trapping potential affects only the target species (the species meant to be trapped) while the scattering rate for both the species is low. In the "tune in" approach the wavelength is chosen close to resonance of the target species which provides a good selective confinement of this species but also increases the scattering rate, which is inversely proportional to the square of the detuning. A trade off needs to be made between the two, while choosing the detuning from resonance. In the "tune out" approach, the wavelength of the trapping potential is chosen such that the spectator species (the species meant not to be trapped in the lattice) has zero dipole potential, which can be achieved by choosing a wavelength between the D_1 and D_2 lines, and is not trapped at all. However, the scattering rate of the spectator species cannot be neglected. In our case, Cs is the target species and Rb is the spectator species. A "tune out" approach will require a blue detuned trap for Cs, since the "tune out" wavelength for Rb is at 790 nm and this requires additional radial confinement. Hence, a "tune in" approach is followed due to technical conveniences. Moreover, since the rate of thermalization between Rb and Cs is large compared to the experiment time scales as has been demonstrated by the sympathetic cooling experiments in [51], a "tune in" approach will be convenient to cool the single Cs atom. This is because, here the scattering rate of the target (Cs atom) is relevant and this can quickly thermalize with Rb and get cooled.

A Titanium Sapphire (Ti:Sa) laser operating at a wavelength of 899 nm has already been incorporated into the experimental setup to create an optical lattice for Cs. The optical lattice has a waist of $\sim 30\,\mu$m with $\sim 100\,$mW of power in each arm. This gives a trap depth of $\sim 1\,$mK for Cs. Here, the Cs atoms will be stored in the absolute ground state which is the $|3,3\rangle$ state for all the experiments due to the absence of inelastic two body collisions and hence, a consequent suppression of losses. At present, the trap is being characterized for the loading of single Cs atoms from the MOT.

6.1.2 Interspecies Feshbach Resonances

For various applications of a single Cs atom and a Rb BEC, it is handy to be able to tune the interactions between the two species. This can be done with the help of magnetic Feshbach resonances.

Figure 6.1 shows the molecular potentials corresponding to two different channels, where a channel corresponds to a particular internal state described by a set of quantum numbers. The atoms collide with each other with an energy E in the "open channel". This is called "open" because this channel is energetically accessible to the atoms. The upper channel (see figure) has a dissociation energy higher than the energy of the colliding atoms. Therefore, this state is energetically inaccessible to the atoms and hence, called a "closed channel". A "closed channel" supports bound states near the dissociation threshold of the "open channel". A Feshbach resonance occurs when the energy of a bound state of the "closed channel" becomes degenerate with that of the energy of the colliding atoms leading to the formation of a quasi-molecule when a coupling exists between the two channels. This energy can be tuned using a magnetic field if the magnetic moments of the two channels are different. Hence, these resonances are called magnetic Feshbach resonances.

The scattering properties are drastically altered at the position of the resonance. The scattering length diverges at the resonance and is positive (negative) when the energy of the bound state is below (above) the energy of the open channel. Far away from the resonance, the scattering length has a value equal to the scattering length a_{bg} of the "open channel". The scattering length as a function of the magnetic field is given by [140]

$$a(B) = a_{\mathrm{bg}}\left(1 - \frac{\delta}{B - B_0}\right) , \tag{6.1}$$

where B_0 is the resonance position and δ represents the width of the resonance, which

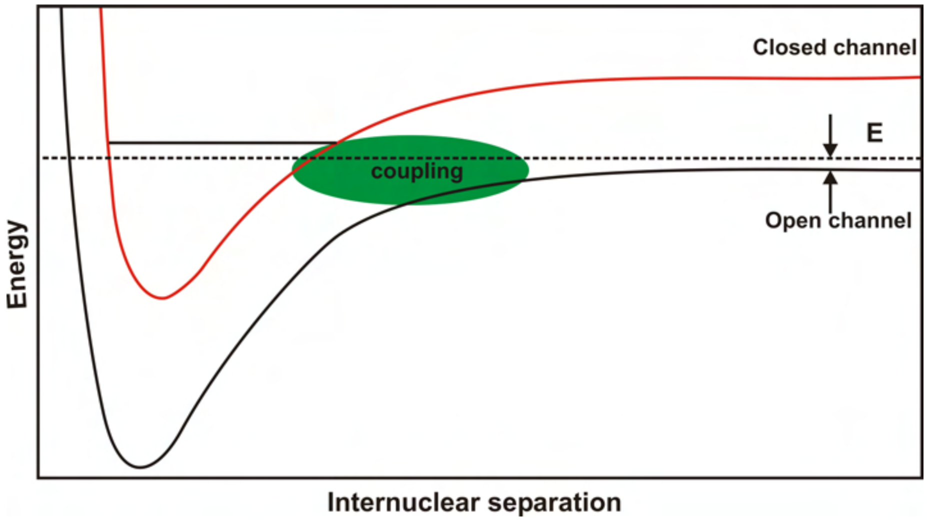

Figure 6.1: A schematic of the molecular potentials of the open (black curve) and closed channel (red curve) are shown. The energy is plotted against the internuclear separation. The atoms collide in the open channel with an energy E. A coupling exists between the two channels. When the energy of the colliding atoms becomes degenerate with the energy of the bound state (shown by the black line) of the closed channel, a quasimolecule is formed in the bound state. This corresponds to a Feshbach resonance.

is the difference between the magnetic field values corresponding to the resonance and the zero crossing of the scattering length. The width indicates the strength of the resonance. The picture depicted in figure 6.1 is a simple picture involving only two internal states or channels. A real system consists of multiple channels.

The elastic and inelastic scattering rates increase drastically at the position of a Feshbach resonance. A Feshbach resonance is typically located by measuring the trap loss due to the inelastic collisions by ramping the magnetic field across a resonance. Inelastic collisions could be two-body or three-body collisions. As already mentioned, a real system consists of multiple channels and therefore, there is usually more than one open channel available for the decay of a quasi-molecule. Hence, a change in the internal state can take place during the collision resulting in inelastic two-body losses. However, in the absolute ground state, which we are interested in, the inelastic two-body collisions are suppressed and the dominant loss mechanism is the three body recombination. Feshbach resonances can also be located by measuring the elastic scattering rate [121].

Homonuclear Feshbach resonances have been experimentally measured for Rb in [141, 122], for Cs in [121, 142] and heteronuclear Rb-Cs Feshbach resonances in [53]. In [53], Feshbach resonances were measured for magnetic field values between 20 to 300 G. Twenty-three interspecies Feshbach resonances were identified for the mixture in the absolute ground state. A broad resonance with a Full Width at Half Maximum (FWHM) of $\delta = 3\,\mathrm{G}$ is observed at a magnetic field of about $B_0 = 180\,\mathrm{G}$. In our experiment, the MOT quadrupole coils would be used in a Helmholtz configuration to provide the homogeneous field required for a Feshbach resonance. Our coils can provide fields up to 1000 G (limited by the power dissipation), hence increasing the range over which the interspecies Feshbach resonances can be examined, providing the possibility of finding broader resonances which can be used to tune the interspecies interactions.

6.1.3 Experiments with a Rb BEC and a Single Cs Atom

There are quite a few proposals for experiments with a single atom in a condensate (see introduction). Here, I will just discuss one of them, which can be tried out with our setup in the near future.

Cooling of a Single Atom to its Motional Ground State by Immersion in a Superfluid

A single neutral atom finds use in quantum information as a qubit that can store quantum information. A heating of these atoms and a subsequent decoherence can occur due to various operations e.g. the transport of qubits. Hence, a cooling of these atoms is required.

A possible method to cool them to their motional ground state while preserving the internal state coherence is to immerse the single atoms into a condensate [45]. The atoms are cooled sympathetically by inducing Bogoliubov excitations in the condensate. In this proposal [45], the single atom is considered to be trapped in an optical lattice, which represents many periodic harmonic potentials. Figure 6.2 shows a schematic of the cooling process. An excitation in the condensate leads to the transition of the single atom from an upper vibrational state to a lower vibrational state or the motional ground state, where each state $|n_i\rangle$ has an energy given by $E(n_i) = n_i \hbar\omega$. Here, ω is the trap frequency of the optical lattice where the single atom is trapped. The rate of energy loss $\dot{E}$ due to such a transition or equivalently, the cooling rate is derived by considering two regimes which depend upon the trap frequency of the lattice and the speed of sound in the condensate. The two regimes are the supersonic and the subsonic regime. In the supersonic regime, $\hbar\omega \gg M_\mathrm{b} v_\mathrm{s}^2/2$, where M_b is the mass of the atoms in the BEC and v_s is the speed of sound in the condensate and in the subsonic regime, $\hbar\omega \ll M_\mathrm{b} v_\mathrm{s}^2/2$. In the supersonic regime, the cooling rate is high (at least about 10 oscillator cycles/s) with significant number of transitions occurring directly to the motional ground state. The cooling rate depends upon the density of the condensate and the interspecies scattering length. The larger the scattering length, the smaller is the time required for the transitions and the

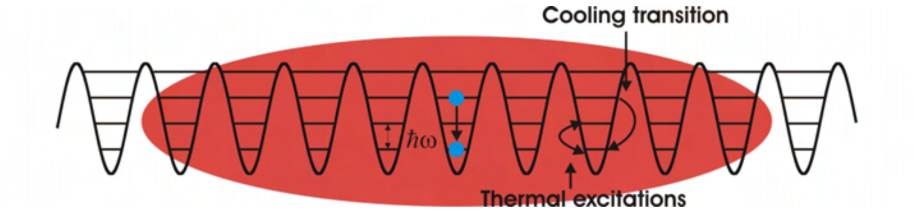

Figure 6.2: Single atom cooling by a BEC : The single atoms (blue spheres) are trapped in a optical lattice with a trap frequency ω. The black lines in each potential of the lattice correspond to the vibrational levels with an energy spacing of $\hbar\omega$ between them. The condensate is shown by the red ellipse. A cooling from a higher to the lower vibrational level occurs as shown in the figure by inducing excitations in the BEC. The temperature achieved by the single atom is restricted by interactions with thermal excitations at a finite BEC temperature resulting in transitions between higher and lower vibrational states.

higher the rate of cooling. In the subsonic regime, transitions occur only to the next lower vibrational level and hence, the cooling rate is lower than in the supersonic regime. The speed of sound in the condensate depends upon the scattering length of the atoms in the condensate and the density of the condensate. For a Rb BEC, for a scattering length of $\sim 100\,a_0$ and a density of $\sim 10^{14}\,\mathrm{cm}^{-3}$, ω is calculated to be $\sim 2\pi \times 400\,\mathrm{Hz}$. Therefore, for typical lattice trap frequencies of a few to few hundreds of kHz, the supersonic regime is relevant.

The single atoms are cooled to the temperature of the condensate. For a finite condensate temperature, transitions can occur between a higher and a lower vibrational level of the optical lattice due to thermal excitations. However, if the temperature of the condensate T is such that the corresponding energy is much lower than the spacing between the vibrational levels $k_\mathrm{B}T \ll \hbar\omega$, then almost all the atoms will be cooled to the motional ground state. Hence, for a Rb condensate temperature of $\sim 100\,\mathrm{nK}$, the trap frequency of the Cs lattice should be of the order of $\sim 20\,\mathrm{kHz}$ to allow efficient cooling. The most important criterion is the avoidance of decoherence during the cooling process. This means that the internal state of the atom should remain unchanged. This can be done by a proper choice of the initial internal states such that the interspecies scattering length (between the neutral atom and the condensate) and the trapping potential is the same for all the internal states.

Bibliography

[1] W. D. Phillips, "Laser cooling and trapping of neutral atoms," *Reviews of Modern Physics*, vol. 70, pp. 721–741, 1998.

[2] C. Cohen-Tannoudji, "Manipulating atoms with photons," *Reviews of Modern Physics*, vol. 70, pp. 707–719, 1998.

[3] Chu, "The manipulation of neutral particles," *Reviews of Modern Physics*, vol. 70, pp. 685–706, 1998.

[4] W. Ketterle and V. Druten, "Evaporative cooling of atoms," *Advances in Atomic, Molecular and Optical Physics*, vol. 37, p. 181, 1996.

[5] K. B. Davis, M.-O. Mewes, M. A. Joffe, M. R. Andrews, and W. Ketterle, "Evaporative Cooling of Sodium Atoms," *Phys. Rev. Lett.*, vol. 74, pp. 5202–5205, 1995.

[6] E. L. Raab, M. Prentiss, A. Cable, S. Chu, and D. E. Pritchard, "Trapping of Neutral Sodium Atoms with Radiation Pressure," *Phys. Rev. Lett.*, vol. 59, pp. 2631–2634, Dec 1987.

[7] D. E. Pritchard, E. L. Raab, and V. Bagnato, "Light Traps using Spontaneous Forces," *Phys. Rev. Lett.*, vol. 57, pp. 310–313, 1986.

[8] A. L. Migdall, J. V. Prodan, W. D. Phillips, T. H. Bergeman, and H. J. Metcalf, "First Observation of Magnetically Trapped Neutral Atoms," *Phys. Rev. Lett.*, vol. 54, pp. 2596–2599, Jun 1985.

[9] T. Bergeman, G. Erez, and H. J. Metcalf, "Magnetostatic trapping fields for neutral atoms," *Phys. Rev. A*, vol. 35, pp. 1535–1546, Feb 1987.

[10] W. Petrich, M. H. Anderson, J. R. Ensher, and E. A. Cornell, "Stable, Tightly Confining Magnetic Trap for Evaporative Cooling of Neutral Atoms," *Phys. Rev. Lett.*, vol. 74, pp. 3352–3355, Apr 1995.

[11] E. A. Cornell and C. Wieman, "Nobel Lecture: Bose-Einstein condensation in a dilute gas, the first 70 years and some recent experiments," *Reviews of Modern Physics*, vol. 74, pp. 875–893, 2002.

[12] W. Ketterle, "Nobel lecture: When atoms behave as waves: Bose-Einstein condensation and the atom laser," *Reviews of Modern Physics*, vol. 74, pp. 1131–1151, 2002.

[13] M. H. Anderson, J. R. Ensher, M. R. Matthews, C. E. Wieman, and E. A. Cor-

nell, “Observation of Bose-Einstein Condensation in a Dilute Atomic Vapor,” *Science*, vol. 269, no. 5221, pp. 198–201, 1995.

[14] K. B. Davis, M. O. Mewes, M. R. Andrews, N. J. van Druten, D. S. Durfee, D. M. Kurn, and W. Ketterle, “Bose-Einstein Condensation in a Gas of Sodium Atoms,” *Phys. Rev. Lett.*, vol. 75, pp. 3969–3973, Nov 1995.

[15] S. Chu, J. E. Bjorkholm, A. Ashkin, and A. Cable, “Experimental Observation of Optically Trapped Atoms,” *Phys. Rev. Lett.*, vol. 57, pp. 314–317, Jul 1986.

[16] J. D. Miller, R. A. Cline, and D. J. Heinzen, “Far-off-resonance optical trapping of atoms,” *Phys. Rev. A*, vol. 47, p. R4567, 1993.

[17] H. Feshbach, “Unified theory of nuclear reactions,” *Annals of Physics*, vol. 5, no. 4, pp. 357 – 390, 1958.

[18] C. Chin, R. Grimm, P. Julienne, and E. Tiesinga, “Feshbach resonances in ultracold gases,” *Reviews of Modern Physics*, vol. 82, pp. 1225–1286, 2010.

[19] T. Köhler, K. Góral, and P. S. Julienne, “Production of cold molecules via magnetically tunable Feshbach resonances,” *Rev. Mod. Phys.*, vol. 78, no. 4, p. 1311, 2006.

[20] C. Chin, A. Kerman, V. Vuletić, and S. Chu, “Sensitive Detection of Cold Cesium Molecules Formed on Feshbach Resonances,” *Phys. Rev. Lett.*, vol. 90, p. 033201, 2003.

[21] S. Jochim, M. Bartenstein, A. Altmeyer, G. Hendl, S. Riedl, C. Chin, J. Hecker Denschlag, and R. Grimm, “Bose-Einstein Condensation of Molecules,” *Science*, vol. 302, no. 5653, pp. 2101–2103, 2003.

[22] J. Herbig, T. Kraemer, M. Mark, T. Weber, C. Chin, H.-C. Nägerl, and R. Grimm, “Preparation of a Pure Molecular Quantum Gas,” *Science*, vol. 301, no. 5639, pp. 1510–1513, 2003.

[23] G. Thalhammer, G. Barontini, L. D. Sarlo, J. Catani, F. Minardi, and M. Inguscio, “Double Species Bose-Einstein Condensate with Tunable Interspecies Interactions,” *Phys. Rev. Lett.*, vol. 100, no. 21, p. 210402, 2008.

[24] C. A. Regal, M. Greiner, and D. S. Jin, “Observation of Resonance Condensation of Fermionic Atom Pairs,” *Phys. Rev. Lett.*, vol. 92, p. 040403, Jan 2004.

[25] M. W. Zwierlein, C. A. Stan, C. H. Schunck, S. M. F. Raupach, A. J. Kerman, and W. Ketterle, “Condensation of Pairs of Fermionic Atoms near a Feshbach Resonance,” *Phys. Rev. Lett.*, vol. 92, p. 120403, Mar 2004.

[26] M. Bartenstein, A. Altmeyer, S. Riedl, S. Jochim, C. Chin, J. H. Denschlag, and R. Grimm, “Collective Excitations of a Degenerate Gas at the BEC-BCS Crossover,” *Phys. Rev. Lett.*, vol. 92, p. 203201, 2004.

[27] P. S. Jessen and I. H. Deutsch, “Optical Lattices,” *Advances in Atomic, Molecular and Optical Physics*, vol. 37, pp. 95–138, 1996.

[28] B. P. Anderson, T. L. Gustavson, and M. A. Kasevich, "Atom trapping in nondissipative optical lattices," *Phys. Rev. A*, vol. 53, pp. R3727–R3730, 1996.

[29] I. Bloch, "Ultracold quantum gases in optical lattices," *Nature Physics*, vol. 1, pp. 23–30, 2005.

[30] D. Jaksch, C. Bruder, J. I. Cirac, C. W. Gardiner, and P. Zoller, "Cold Bosonic Atoms in Optical Lattices," *Phys. Rev. Lett.*, vol. 81, pp. 3108–3111, 1998.

[31] M. Greiner, O. Mandel, T. Esslinger, T. W. Hänsch, and I. Bloch, "Quantum phase transition from a superfluid to a Mott insulator in a gas of ultracold atoms," *Nature*, vol. 425, pp. 39–44, 2002.

[32] O. Mandel, M. Greiner, A. Widera, T. Rom, T. W. Hänsch, and I. Bloch, "Coherent Transport of Neutral Atoms in Spin-Dependent Optical Lattice Potentials," *Phys. Rev. Lett.*, vol. 91, p. 010407, 2003.

[33] O. Mandel, M. Greiner, A. Widera, T. Rom, T. W. Hänsch, and I. Bloch, "Controlled collisions for multi-particle entanglement of optically trapped atoms," *Nature*, vol. 425, p. 937, 2003.

[34] I. Bloch, "Quantum coherence and entanglement with ultracold atoms in optical lattices," *Nature*, vol. 453, pp. 1016–1022, 2008.

[35] F. J. Sherson, C. Weitenberg, M. Endres, M. Cheneau, I. Bloch, and S. Kuhr, "Single-atom-resolved fluorescence imaging of an atomic Mott insulator," *Nature*, vol. 467, pp. 68–72, 2010.

[36] W. S. Bakr, A. Peng, M. Tai, R. Ma, J. Simon, J. I. Gillen, S. Fölling, L. Pollet, and M. Greiner, "Probing the Superfluid–to–Mott Insulator Transition at the Single-Atom Level," *Science*, vol. 329, pp. 547–550, 2010.

[37] S. Kuhr, W. Alt, D. Schrader, M. Muller, V. Gomer, and D. Meschede, "Deterministic Delivery of a Single Atom," *Science*, vol. 293, no. 5528, pp. 278–280, 2001.

[38] D. Schrader, S. Kuhr, W. Alt, M. Müller, V. Gomer, , and D. Meschede, "An optical conveyor belt for single neutral atoms," *Applied Physics B*, vol. 73, p. 1432, 2001.

[39] D. Schrader, I. Dotsenko, M. Khudaverdyan, Y. Miroshnychenko, A. Rauschenbeutel, and D. Meschede, "Neutral Atom Quantum Register," *Phys. Rev. Lett.*, vol. 93, p. 150501, Oct 2004.

[40] Y. Miroshnychenko, W. Alt, I. Dotsenko, L. Förster, M. Khudaverdyan, D. Meschede, D. Schrader, and A. Rauschenbeutel, "Quantum engineering: An atom-sorting machine," *Nature*, vol. 442, p. 151, 2006.

[41] Y. Miroshnychenko, W. Alt, I. Dotsenko, L. Forster, M. Khudaverdyan, A. Rauschenbeutel, and D. Meschede, "Precision preparation of strings of trapped neutral atoms," *New Journal of Physics*, vol. 8, no. 9, p. 191, 2006.

[42] M. Khudaverdyan, W. Alt, T. Kampschulte, S. Reick, A. Thobe, A. Widera, and D. Meschede, "Quantum Jumps and Spin Dynamics of Interacting Atoms in a Strongly Coupled Atom-Cavity System," *Phys. Rev. Lett.*, vol. 103, p. 123006, 2009.

[43] S. Reick, K. Mölmer, W. Alt, M. Eckstein, T. Kampschulte, L. Kong, R. Reimann, A. Thobe, A. Widera, and D. Meschede, "Analyzing quantum jumps of one and two atoms strongly coupled to an optical cavity," *Journal of Optical Society of America B*, vol. 27, pp. A152–A163, 2010.

[44] M. Karski, L. Förster, J. M. Choi, W. Alt, A. Widera, and D. Meschede, "Nearest-Neighbor Detection of Atoms in a 1D Optical Lattice by Fluorescence Imaging," *Phys. Rev. Lett.*, vol. 102, no. 5, p. 053001, 2009.

[45] A. J. Daley, P. O. Fedichev, and P. Zoller, "Single-atom cooling by superfluid immersion: A nondestructive method for qubits," *Phys. Rev. A*, vol. 69, p. 022306, Feb 2004.

[46] A. Griessner, A. J. Daley, S. R. Clark, D. Jaksch, and P. Zoller, "Dark-State Cooling of Atoms by Superfluid Immersion," *Phys. Rev. Lett.*, vol. 97, no. 22, p. 220403, 2006.

[47] A. Micheli, A. J. Daley, D. Jaksch, and P. Zoller, "Single Atom Transistor in a 1D Optical Lattice," *Phys. Rev. Lett.*, vol. 93, p. 140408, 2004.

[48] A. Klein and M. Fleischhauer, "Interaction of impurity atoms in Bose-Einstein condensates," *Phys. Rev. A*, vol. 71, p. 033605, Mar 2005.

[49] M. Bruderer and D. Jaksch, "Probing BEC phase fluctuations with atomic quantum dots," *New Journal of Physics*, vol. 8, no. 6, p. 87, 2006.

[50] H. T. Ng and S. Bose, "Single-atom-aided probe of the decoherence of a Bose-Einstein condensate," *Phys. Rev. A*, vol. 78, no. 2, p. 023610, 2008.

[51] M. Haas, V. Leung, D. Frese, D. Haubrich, S. John, C. Weber, A. Rauschenbeutel, and D. Meschede, "Species-selective microwave cooling of a mixture of rubidium and caesium atoms," *New Journal of Physics*, vol. 9, no. 5, p. 147, 2007.

[52] M. Haas, *Sympathetisches Kühlen in einer Rubidium-Cäsium-Mischung: Erzeugung ultrakalter Cäsiumatome.* PhD thesis, 2007.

[53] K. Pilch, A. D. Lange, A. Prantner, G. Kerner, F. Ferlaino, H.-C. Nägerl, and R. Grimm, "Observation of interspecies Feshbach resonances in an ultracold Rb-Cs mixture," *Phys. Rev. A*, vol. 79, no. 4, p. 042718, 2009.

[54] C. Weber, *Controlled few-body interactions in ultracold bosonic mixtures.* PhD thesis, Universität Bonn, 2010.

[55] C. Weber, S. John, N. Spethmann, D. Meschede, and A. Widera, "Single Cs

atoms as collisional probes in a large Rb magneto-optical trap," *Phys. Rev. A*, vol. 82, p. 042722, 2010.

[56] J. Dalibard, "Collisional dynamics of ultra-cold atomins gases," in *M. INGUSCIO, S. STRINGARI AND C. WIEMAN, Bose-Einstein Condensation in Atomic Gases, Proceedings of The International School of Physics Enrico Fermi-Course CXL, 351, IOS Press, Amsterdam*, 1999.

[57] J. Weiner, V. S. Bagnato, S. Zilio, and P. S. Julienne, "Experiments and theory in cold and ultracold collisions," *Rev. Mod. Phys.*, vol. 71, pp. 1–85, Jan 1999.

[58] J. Vigué, "Possibility of applying laser-cooling techniques to the observation of collective quantum effects," *Phys. Rev. A*, vol. 34, pp. 4476–4479, Nov 1986.

[59] A. Gallagher and D. E. Pritchard, "Exoergic collisions of cold Na^*-Na," *Phys. Rev. Lett.*, vol. 63, pp. 957–960, Aug 1989.

[60] P. S. Julienne and J. Vigué, "Cold collisions of ground- and excited-state alkali-metal atoms," *Phys. Rev. A*, vol. 44, pp. 4464–4485, Oct 1991.

[61] A. Lagendijk, I. F. Silvera, and B. J. Verhaar, "Spin exchange and dipolar relaxation rates in atomic hydrogen: Lifetimes in magnetic traps," *Phys. Rev. B*, vol. 33, pp. 626–628, Jan 1986.

[62] P. Julienne, F. H. Mies, E. Tiesinga, and C. J. Williams, "Collisional Stability of Double Bose Condensates," *Phys. Rev. Lett.*, vol. 78, pp. 1880–1883, 1997.

[63] F. H. Mies, C. J. Williams, P. S. Julienne, and M. Krauss, "Estimating Bounds on Collisional Relaxation Rates of Spin-Polarized ^{87}Rb Atoms at Ultracold Temperatures," *J. Res. Natl. Inst. Stand. Technol.*, vol. 101, p. 521, 1996.

[64] H. M. J. M. Boesten, A. J. Moerdijk, and B. J. Verhaar, "Dipolar decay in two recent Bose-Einstein condensation experiments," *Phys. Rev. A*, vol. 54, pp. R29–R32, 1996.

[65] P. J. Leo, E. Tiesinga, and P. Julienne, "Elastic and Inelastic Collisions of Cold Spin-Polarized ^{133}Cs Atoms," *Phys. Rev. Lett.*, vol. 81, pp. 1389–1392, 1998.

[66] J. Söding, D. Guéry-Odelin, P. Desbiolles, F. Chevy, H. Inamori, and J. Dalibard, "Three-body decay of a rubidium Bode-Einstein condensate," *Applied Physics B*, vol. 69, pp. 257–261, 1999.

[67] P. O. Fedichev, M. W. Reynolds, and G. V. Shlyapnikov, "Three-Body Recombination of Ultracold Atoms to a Weakly Bound s Level," *Phys. Rev. Lett.*, vol. 77, pp. 2921–2924, 1996.

[68] P. Feng, D. Hoffmann, and T. Walker, "Comparison of trap-loss collision spectra for ^{85}Rb and ^{87}Rb ," *Phys. Rev. A*, vol. 47, pp. R3495–R3498, 1993.

[69] D. Wallace, P. Dinneen, N. K.-Y. Tan, T. T. Grove, and L. P. Gould, "Isotopic Difference in Trap Loss Collisions of Laser Cooled Rubidium Atoms," *Phys. Rev. Lett.*, vol. 69, pp. 897–900, 1992.

[70] D. Hoffmann, P. Feng, and T. Walker, "Measurements of Rb trap-loss collision spectra," *J.Opt.Soc.Am.B*, vol. 11, pp. 712–719, 1994.

[71] D. Sesko, T. Walker, C. Monroe, A. Gallagher, and C. Wieman, "Collisional losses from a light-force atom trap," *Phys. Rev. Lett.*, vol. 63, pp. 961–964, Aug 1989.

[72] A. Fioretti, J. Müller, P. Verkerk, M. Allegrini, E. Arimondo, and P. Julienne, "Direct measurement of fine-structure collisional losses from a Cs magneto-optical trap," *Phys. Rev. A*, vol. 55, pp. R3999–R4002, 1997.

[73] M. L. Harris, P. Tierney, and S. L. Cornish, "Magnetic trapping of a cold Rb-Cs atomic mixture," *Journal of Physics B*, vol. 41, no. 3, p. 035303 (9pp), 2008.

[74] B. Ueberholz, S. Kuhr, D. Frese, V. Gomer, and D. Meschede, "Cold collisions in a high-gradient magneto-optical trap," *Journal of Physics B*, vol. 35, no. 23, pp. 4899–4914, 2002.

[75] P. Willems, R. Boyd, J. Bliss, and K. Libbrecht, "Stability of Magneto-optical Traps with Large Field Gradients:Limits on the Tight Confinement of Single Atoms," *Phys. Rev. Lett.*, vol. 78, pp. 1660–1663, 1997.

[76] J. Söding, D. Guéry-Odelin, P. Desbiolles, G. Ferrari, and J. Dalibard, "Giant Spin Relaxation of an Ultracold Cesium Gas," *Phys. Rev. Lett.*, vol. 80, pp. 1869–1872, 1998.

[77] D. Guéry-Odelin, J. Söding, P. Desbiolles, and J. Dalibard, "Is Bose-Einstein condensation of atomic cesium possible?," *Europhysics Letters*, vol. 44, pp. 25–30, 1998.

[78] T. Weber, J. Herbig, M. Mark, H.-C. Nägerl, and R. Grimm, "Three-Body Recombination at Large Scattering Lengths in an Ultracold Atomic Gas," *Phys. Rev. Lett.*, vol. 91, p. 123201, 2003.

[79] E. Burt, R. Ghrist, C. Myatt, M. Holland, E. A. Cornell, and C. Wieman, "Coherence, Correlations, and Collisions: What One Learns about Bose-Einstein Condensates from their Decay," *Phys. Rev. Lett.*, vol. 79, pp. 337–340, 1997.

[80] S. Bose *Z.Phys.*, vol. 26, p. 178, 1924.

[81] A. Einstein, "Quantentheorie des einatomigen idealen Gases," *Sitzungsberichte der Preussischen Akademie der Wissenschaften, Physikalisch-mathematische Klasse*, p. 261–267, 1924.

[82] C. C. Bradley, C. A. Sackett, and R. G. Hulet, "Bose-Einstein Condensation of Lithium: Observation of Limited Condensate Number," *Phys. Rev. Lett.*, vol. 78, pp. 985–989, 1997.

[83] D. G. Fried, T. C. Killian, L. Willmann, D. Landhuis, S. C. Moss, D. Kleppner, and T. J. Greytak, "Bose-Einstein Condensation of Atomic Hydrogen," *Phys. Rev. Lett.*, vol. 81, pp. 3811–3814, 1998.

[84] C. Pethick and H. Smith, *Bose Einstein Condensation in dilute gases.* Cambridge University Press, 2002.

[85] F. Bloch, "Nuclear Induction," *Phys. Rev.*, vol. 70, pp. 460–474, 1946.

[86] I. I. Rabi, "Space Quantization in a Gyrating Magnetic Field," *Phys. Rev.*, vol. 51, pp. 652–654, 1937.

[87] L. Allen and J. Eberly, *Optical Resonance and Two-Level Atoms.* Dover Publications, Inc., New York, 1987.

[88] C. Cohen-Tannoudji, B. Diu, and F. Laloe, *Quantum Mechanics.* John Wiley and Sons, 1977.

[89] H. Haken and H. Wolf, *The Physics of Atoms and Quanta.* Springer Verlag, 1996.

[90] C. Wiemann, D. E. Pritchard, and D. J. Wineland, "Atom Cooling, trapping, and quantum manipulation," *Reviews of Modern Physics*, vol. 71, pp. S253–S262, 1999.

[91] C. E. Wiemann and L. Hollberg, "Using diode lasers for atomic physics," *Review of Scientific Instruments*, vol. 62, pp. 1–20, 1991.

[92] C. Wieman and T. W. Hänsch, "Doppler-Free Laser Polarization Spectroscopy," *Phys. Rev. Lett.*, vol. 36, pp. 1170–1173, May 1976.

[93] K. L. Corwin, Z.-T. Lu, C. F. Hand, R. J. Epstein, and C. E. Wieman, "Frequency-Stabilized Diode Laser with the Zeeman Shift in an Atomic Vapor," *Appl. Opt.*, vol. 37, no. 15, pp. 3295–3298, 1998.

[94] M. A. Sikking, G. I. Hughes, P. Tierney, and S. L. Cornish, "DAVLL lineshapes in atomic rubidium," *Journal of Physics B: Atomic, Molecular and Optical Physics*, vol. 40, pp. 187–198, 2007.

[95] W. Demtröder, *Laser Spectroscopy.* Springer Verlag, 1996.

[96] D. A. Steck, "Rubidium 87 D Line Data," *http://steck.us/alkalidata*, vol. revision 2.0.1, May 2008.

[97] E. A. Donley, T. Heavner, F. Levi, M. Tataw, and S. Jefferts, "Double-pass acousto-optic modulator system," *Review of Scientific Instruments*, vol. 76, p. 063112, 2005.

[98] D. A. Steck, "Cesium D Line Data ," *http://steck.us/alkalidata*, vol. revision 1.6, 2003.

[99] B. Bransden and C. Joachain, *Physics of Atoms and Molecules.* Longman Group Ltd, 1983.

[100] H. J. Metcalf and P. van der Straten, *Laser Cooling and Trapping.* Springer Verlag, 1999.

[101] P. D. Lett, W. Philipps, S. Rolston, C. Tanner, R. N. Watts, and C. I. West-

brook, “Optical molasses,” *Journal of Optical Society of America B*, vol. 6, pp. 2084–2107, 1989.

[102] C. Saloman, J. Dalibard, W. D. Phillips, A. Clairon, and S. Guellati, “Laser Cooling of Cesium Atoms below 3μK,” *Europhysics Letters*, vol. 12, pp. 683–688, 1990.

[103] S. Chu, L. Hollberg, J. E. Bjorkholm, A. Cable, and A. Ashkin, “Three-dimensional viscous confinement and cooling of atoms by resonance radiation pressure,” *Phys. Rev. Lett.*, vol. 55, pp. 48–51, Jul 1985.

[104] C. Monroe, W. Swann, H. Robinson, and C. Wieman, “Very cold trapped atoms in a vapor cell,” *Phys. Rev. Lett.*, vol. 65, pp. 1571–1574, Sep 1990.

[105] J. Dalibard and C. Cohen-Tannoudji, “Laser cooling below the Doppler limit by polarization gradients: simple theoretical models,” *J. Opt. Soc. Am. B*, vol. 6, no. 11, pp. 2023–2045, 1989.

[106] P. D. Lett, R. N. Watts, C. I. Westbrook, W. D. Phillips, P. L. Gould, and H. J. Metcalf, “Observation of Atoms Laser Cooled below the Doppler Limit,” *Phys. Rev. Lett.*, vol. 61, pp. 169–172, Jul 1988.

[107] A. Aspect, E. Arimondo, R. Kaiser, N. Vansteenkiste, and C. Cohen-Tannoudji, “Laser Cooling below the One-Photon Recoil Energy by Velocity-Selective Coherent Population Trapping,” *Phys. Rev. Lett.*, vol. 61, pp. 826–829, 1988.

[108] D. Haubrich, A. Höpe, and D. Meschede, “A simple model for optical capture of atoms in strong magnetic quadrupole fields,” *Opt. Commun.*, vol. 102, p. 225, 1993.

[109] T. Weikum, “Ein System zur Fluoreszenzdetektion einzelner Cäsiumatome in einem Rubidium-Bose-Einstein-Kondensat,” 2009.

[110] T. Esslinger, I. Bloch, and T. W. Hänsch, “Bose-Einstein condensation in a quadrupole-Ioffe-configuration trap,” *Phys. Rev. A*, vol. 58, pp. R2664–R2667, Oct 1998.

[111] E. Majorana, “Atomi orientati in campo magnetico variabile,” *Nuovo Cimento*, vol. 9, p. 43, 1932.

[112] T. Walker, D. Sesko, and C. Wieman, “Collective behavior of optically trapped neutral atoms,” *Phys. Rev. Lett.*, vol. 64, pp. 408–411, Jan 1990.

[113] M. Yamashita, M. Koashi, T. Mukai, M. Mitsunaga, N. Imoto, and T. Mukai, “Optimization of evaporative cooling towards a large number of Bose-Einstein-condensed atoms,” *Phys. Rev. A*, vol. 67, p. 023601, 2003.

[114] W. Ketterle, D. S. Durfee, and D. M. Stamper-Kurn, “Making, probing and understanding: Bose-Einstein Condensation in Atomic Gases,” *Proceedings of the international school of physics Enrico Fermi*, vol. Course CXL, p. 67, Apr. 1999.

[115] A. Marte, *Feshbach-Resonanzen bei Stößen ultrakalter Rubidiumatome.* PhD thesis, Technische Universität München, Max-Planck-Institut für Quantenoptik, 2003.

[116] D. Haubrich, H. Schadwinkel, F. Strauch, B. Ueberholz, R. Wynands, and D. Meschede, "Observation of individual neutral atoms in magnetic and magneto-optical traps," *Europhys. Lett.*, vol. 34, no. 9, pp. 663–668, 1996.

[117] Z. Hu and H. J. Kimble, "Observation of a single atom in a magneto-optical trap," *Opt. Lett.*, vol. 19, no. 22, pp. 1888–1890, 1994.

[118] A. Ashkin, "Acceleration and Trapping of Particles by Radiation Pressure," *Phys. Rev. Lett.*, vol. 24, pp. 156–159, 1970.

[119] A. Ashkin, "Trapping of Atoms by Resonance Radiation Pressure," *Phys. Rev. Lett.*, vol. 40, pp. 729–732, Mar 1978.

[120] R. Grimm, M. Weidemüller, and Y. B. Ovchinnikov, "Optical dipole traps for neutral atoms," *Advances in Atomic, Molecular and Optical Physics*, vol. 42, p. 95, 2000.

[121] C. Chin, V. Vuletić, A. J. Kerman, and S. Chu, "High Resolution Feshbach Spectroscopy of Cesium," *Phys. Rev. Lett.*, vol. 85, pp. 2717–2720, 2000.

[122] A. Marte, T. Volz, J. Schuster, S. Dürr, G. Rempe, E. G. M. van Kempen, and B. J. Verhaar, "Feshbach Resonances in Rubidium 87: Precision Measurement and Analysis," *Phys. Rev. Lett.*, vol. 89, p. 283202, 2002.

[123] T. Gustavson, A. Chikkatur, A. Leanhardt, A. Görlitz, S. Gupta, D. E. Pritchard, and W. Ketterle, "Transport of Bose-Einstein Condensates with Optical Tweezers," *Phys. Rev. Lett.*, vol. 88, p. 020401, 2002.

[124] S. Schmid, G. Thalhammer, K. Winkler, F. Lang, and J. Denschlag, "Long distance transport of ultracold atoms using a 1D optical lattice," *New Journal of Physics*, vol. 8, pp. 1–15, 2006.

[125] M. Greiner, I. Bloch, T. W. Hänsch, and T. Esslinger, "Magnetic transport of trapped cold atoms over a large distance," *Phys. Rev. A*, vol. 63, p. 031401, 2001.

[126] C. Klempt, T. Henninger, O. Topic, J. Will, S. Falke, W. Ertmer, and J. Arlt, "Transport of a quantum degenerate heteronuclear Bose-Fermi mixture in a harmonic trap," *European Physical Journal D*, vol. 48, pp. 121–126, 2008.

[127] D. Stamper-Kurn, M. Andrews, A. Chikkatur, S. Inouye, H.-J. Miesner, J. Stenger, and W. Ketterle, "Optical Confinement of a Bose-Einstein Condensate," *Phys. Rev. Lett.*, vol. 80, pp. 2027–2030, 1998.

[128] S. Adams, J. Lee, N. Davidson, M. Kasevich, and S. Chu, "Evaporative Cooling in a Crossed Dipole Trap," *Phys. Rev. Lett.*, vol. 74, pp. 3577–3580, 1995.

[129] M. Barrett, J. Sauer, and M. Chapman, "All-Optical Formaiton of an Atomic Bose- Einstein Condensate," *Phys. Rev. Lett.*, vol. 87, p. 010404, 2001.

[130] S. Granade, M. Gehm, K. O'Hara, and J. Thomas, "All-Optical Production of a Degenerate Fermi Gas," *Phys. Rev. Lett.*, vol. 88, p. 120405, 2002.

[131] T. Savard, K. O'Hara, and J. Thomas, "Laser-noise-induced heating in far-off resonance optical traps," *Phys. Rev. A*, vol. 56, p. R1095, 1997.

[132] M. E. Gehm, K. O'Hara, T. Savard, and J. Thomas, "Dynamics of noise-induced heating in atom traps," *Phys. Rev. A*, vol. 58, pp. 3914–3920, 1998.

[133] R. J. Morris, "Theory of Adiabatic Rapid Passage for Three Equally Spaced Levels," *Phys. Rev.*, vol. 133, pp. A740–A750, 1964.

[134] A. Corney, *Atomic and Laser Spectroscopy.* Oxford Unievrsity Press, 1988.

[135] G. Breit and I. I. Rabi, "Measurement of Nuclear Spin," *Phys. Rev.*, vol. 38, no. 11, pp. 2082–2083, 1931.

[136] T. R. Gentile, B. J. Hughey, D. Kleppner, and T. W. Ducas, "Experimental study of one- and two-photon Rabi oscillations," *Phys. Rev. A*, vol. 40, pp. 5103–5115, 1989.

[137] A. Widera, F. Gerbier, S. Fölling, T. Gericke, O. Mandel, and I. Bloch, "Coherent Collisional Spin Dynamics in Optical Lattices," *Phys. Rev. Lett.*, vol. 95, p. 190405, 2005.

[138] D. Sivia, *Data Analysis, A Bayesian Tutorial.* Oxford University Press, 2006.

[139] L. J. LeBlanc and J. H. Thywissen, "Species-specific optical lattices," *Phys. Rev. A*, vol. 75, no. 5, p. 053612, 2007.

[140] A. J. Moerdijk, B. J. Verhaar, and A. Axelsson, "Resonances in ultracold collisions of ^6Li, ^7Li, and ^{23}Na," *Phys. Rev. A*, vol. 51, pp. 4852–4861, Jun 1995.

[141] M. Erhard, H. Schmaljohann, J. Kronjäger, K. Bongs, and K. Sengstock, "Measurement of a mixed-spin-channel Feshbach resonance in ^{87}Rb ," *Phys. Rev. A*, vol. 69, p. 032705, 2004.

[142] V. Vuletić, A. J. Kerman, C. Chin, and S. Chu, "Observation of Low-Field Feshbach Resonances in Collisions of Cesium Atoms," *Phys. Rev. Lett.*, vol. 82, pp. 1406–1409, 1999.

Danksagung/Acknowledgement

An dieser Stelle möchte ich erstmal Prof. Meschede danken, der mir die Möglichkeit gegeben hat in dieser Gruppe meine Doktorarbeit zu machen. Ich möchte auch Prof. Weitz danken für die Übernahme des Zweitegutachtens.

Ich möchte Artur Widera danken für die viele Ideen am Experiment und für die andauernd Betreuung. Die meiste Zeit meiner Arbeit habe ich mit Claudia Weber und Nicolas Spethmann verbracht. Ich danke euch für das tolle Arbeitsklima im Labor und die konstruktive Diskussion. Ich danke ihr drei auch für das Korrektur-lesen meiner Arbeit. Während der gesamten Arbeitszeit haben auch die Diplomanden, Tatjana Weikum und Oskar Fetsch das Experiment unterstützt. Ich danke ihnen für ihren Einsatz. Ich möchte mich auch bei den ehemaligen Kollegen Michael Haas und Daniel Frese danken, die mir am Anfang meinem Arbeit viel geholfen haben und mich ins Experiment eingewiesen haben. Wolfgang Alt und Dietmer Haubrich danke ich für viele wichtige Tips fürs Experiment.

Die Naturwissenschaftamt von Nord Rhein Westphalia (NRW-MWIFT) danke ich für die finazielle unterstützung.

Mein Dank geht auch an das BIGS Sekretariat, Dr. Doris Thrun und Petra Weiss, die mir am Anfang mit den offizielen Sachen sehr geholfen haben. Ich danke auch dem Sekretariat im haus, Annelise von Rudolf Miglo, Fien Latumahina, Illona Jaschke und Dietmer Haubrich für die Unterstützung von offizielen Sachen. Den Elektronik- und Mechanik-werkstätten danke ich für die technische Betreuung.

My life in Bonn would not have been so enjoyable and pleasant without the presence of many important people. First of all, I would like to thank my aunt and uncle for providing me with a family atmosphere miles away from home. I thank all my friends who have helped and supported me during various stages of my stay here, Deepak and Preethi for helping me counter my home-sickness during the beginning of my stay here, Sada and Vamshi for all the wonderful get-togethers and the nice Indian food and Claudia and Devi for keeping up my morale when things didn't go so well.

Last but not the least, my gratitude goes to my family. I thank my husband, Santhosh for all the understanding and support during the final stage of my PhD. And above all, I'd like to thank my parents and sister for the constant love, support and encouragement, without which I would not have been able to successfully complete my work, especially Amma for everything, it would never have been the same without you. I love you all!